Nanostructured Non-Precious Metal Catalysts for Polymer Electrolyte Fuel Cell

by

Ryan S. Hsu

A thesis
presented to the University of Waterloo
in fulfillment of the
thesis requirement for the degree of
Master of Applied Science
in
Chemical Engineering
Waterloo, Ontario, Canada, 2010

Author’s Declaration

I hereby declare that I am the sole author of this thesis. This is a true copy of the thesis, including any required final revisions, as accepted by my examiners.

I understand that my thesis may be made electronically available to the public.

Abstract

Polymer electrolyte membrane fuel cells (PEFCs) have long been thought of as a promising clean alternative energy electrochemical device. They are lightweight, highly efficient, modular and scalable devices. A fuel such as H_2 or methanol that can be readily produced from a variety of sources can be utilized in PEFCs to generate electricity with low or no emissions. Despite these advantages, fuel cell technologies have failed to reach mass commercialization mainly due to short operational lifetimes and the high cost of materials. In particular, the polymer membrane and the catalyst layer have been problematic in reducing the material cost. Currently, platinum is the dominant material used to catalyze fuel cell reactions. However platinum is very expensive and scarce. In order to pursue the mass commercialization of fuel cells, two methods have been proposed: 1) increasing the utilization of platinum to lower the loading required, and 2) replacing platinum completely with a non-precious material. The latter has been suggested to be the long term solution due to the increasing cost of platinum.

This thesis explores the elimination of platinum through the use of nanostructured non-precious metal catalysts for polymer electrolyte fuel cells. Several catalysts have been synthesized without the use of platinum that are active for the oxygen reduction reaction (ORR) which occurs at the cathode. Three different synthetic techniques were utilized using different nitrogen precursors. Aside from the different nitrogen precursors, each set of experiments utilize a different approach to optimize the oxygen reduction performance. Different characterization techniques are used to learn more about the ORR on non-precious metal fuel cells.

The first experiment utilizes ethylenediamine, a well-known nitrogen precursor for non-precious metal fuel cell catalysts. Ethylenediamine is deposited onto two different porous carbon black substrates to determine the effectiveness of different porosities in creating active sites for the ORR. Of the two carbon black species, Ketjenblack EC-600JD and Ketjenblack ED-300J, the former was found to be more porous and effective. This result was mainly attributed to the increased surface area of the carbon black which allowed for better dispersion and a greater active site density. In this experiment, the coating of ethylenediamine on carbon black was also refluxed for 3 hours prior to the pyrolysis. It was found that refluxed catalyst samples showed much improved performance than catalyst samples without this procedural modification.

The next experiment utilized cyanamide as a nitrogen precursor. Cyanamide was chosen due to its ability to form larger amounts of pyridinic nitrogen on the surface of the catalyst after a high temperature pyrolysis stage. The catalysts were heat-treated at 1000^{o}C and the performance was measured. NH_3 was introduced during the pyrolysis, which could remove the excess coating from the carbon surface, and increase the surface area of the catalyst by unblocking the carbon pores. A third modification to the procedure was carried out, where the heat-treated sample was ball-milled, re-coated, and heat-treated again in ammonia conditions to increase the nitrogen functionalities and increase the active site density. The performance was slightly increased from the original heat-treated sample. However due to the decreased surface area, the limiting current density also decreased. It was believed that ball-milling the sample crushed the pores within the catalyst sample, thereby lowering the active surface area and thus the current density. Therefore, the last sample was prepared similarly to the procedure for the third sample, but without ball-milling. This sample had restored surface area and improved ORR performance over all the synthesized catalyst samples – these experiments allowed for important realizations regarding the nature of the Fe-cyanamide-KJ600 catalysts and allowed for a drastic improvement in onset and half-wave potentials from the first catalyst.

The final experiment discussed in this thesis describes the work done with 1,2,4,5-tetracyanobenzene and tetracyanoethylene as phthalcyanine precursors for non-precious metal catalysts (NPMCs). Iron(II) acetate was mixed with these phthalocyanine precursors to form polymer sheets of iron phthalocyanine or its monomeric units. By the creation of these polymer sheets of iron phthalocyanine, it allowed for a uniform distribution of iron centres on the surface of the carbon after a heat-treatment step. This allowed for high active site density through the design of these sheet polymers and prevented agglomeration or blockage of active sites which is thought to be a common problem in the synthesis of many NPMCs. Both tetracyanobenzene and tetracyanoethylene as precursors were tested. The tetracyanobenzene catalyst was heat-treated at different temperature ranging from 700-1100^{o}C and characterized through electrochemical tests for the ORR.

As an overall conclusion to this work, several catalyst samples were made and different approaches were successfully employed to improve the ORR performance. Of the synthesis treatments utilized to improve performance, each specific catalyst had different parameters to

tweak in order to improve ORR performance. With X-ray photoelectron spectroscopy (XPS) analysis, conclusions were also specific to the catalysts structure and synthesis procedure, however quaternary and pyrrolic nitrogen groups seemed to play an influential role to the ORR final performance. Although relative amount of pyridinic nitrogen was not seen to increase with increasing catalyst performance during the studies; it may still play an essential role in the reduction of oxygen on the catalyst surface. The author of this work has not ruled out that possibility. Several recommendations for future work were suggested to broaden the knowledge and understanding of nanostructure non-precious metal catalysts to design a high performing, durable, and low-cost alternative to platinum based catalysts.

Acknowledgements

The University of Waterloo and the Natural Sciences and Engineering Research Council of Canada (NSERC) are gratefully acknowledged for their financial support for this work.

I would also like to acknowledge the help and support received from Dr. Zhongwei Chen, Dr. Michael Fowler and several of my colleagues in producing this work.

Dedication

This work is dedicated to my mother, Alice Hsu, and Paul Hwang for her endless support and faith in me.

Table of Contents

List of Figures

List of Tables

List of Acronyms

BET	Brunauer Emmett and Teller
DOE	U.S. Department of Energy
EDA	Ethylenediamine
EDX	Energy Dispersive X-Ray
FTIR	Fourier Transformed Infrared Spectroscopy
GDE	Gas Diffusion Electrode
KJ300	Ketjenblack EC-300J
KJ600	Ketjenblack EC-600JD
MEA	Membrane Electrode Assembly
NAA	Nitrogen Adsorption Analysis
NPMC	Non-Precious Metal Catalyst
OCV	Open Circuit Voltage
ORR	Oxygen Reduction Reaction
PEFC	Polymer Electrolyte Fuel Cell
RDE	Rotating Disc Electrode
RHE	Reversible Hydrogen Electrode
RRDE	Rotating Ring Disc Electrode
SAXS	Small Angle X-Ray Spectroscopy
SEM	Scanning Electron Microscopy
TCNB	1,2,4,5 Tetracyanobenzene
TCNE	Tetracyanoethylene
TEM	Transmission Electron Microscopy
TGA	Thermogravimetric Analysis

ToF-SIMS	Time-of-Flight Secondary Ion Mass Spectrometry
WAXS	Wide Angle X-Ray Spectroscopy
XPS	X-Ray Photoelectron Spectroscopy
XRD	X-Ray Diffraction

Section 1: Introduction

1.1 Problem Statement

As the world's energy demands increase and there becomes a strain on global fossil fuel reserves, fuel cell systems, particularly polymer electrolyte fuel cells (PEFCs), are becoming increasingly popular as an alternative to current energy systems. Existing PEFCs are expensive as they rely on costly membrane materials and precious platinum metal for the electrocatalyst.

To reduce these costs, PEFC materials, which are durable, stable, high performing, as well as low cost, must be developed to ensure successful commercialization.

1.2 Scope & Objectives

This work outlines the work done on developing non-precious metal fuel cell electrocatalysts for H_2/O_2 PEFCs. The work was carried out primarily in Dr. Zhongwei Chen's Applied Nanomaterials and Clean Energy Laboratory at the University of Waterloo.

This thesis describes a few methodologies utilized for the synthesis and design of non-precious metal catalysts (NPMCs) for the oxygen reduction reaction (ORR) that is critical for the functioning of a PEFC. The development of such NPMCs is important for the understanding of the ORR mechanism for H_2/O_2 fuel cells. Current barriers with these types of catalysts include their rather low catalytic activity compared to precious metal catalysts and their poor stability in fuel cell operating conditions.

The intent of this work is to advance the field of fuel cell catalysis, or more specifically, NPMCs, such that fuel cell catalysts can be manufactured at low costs while performing at a high level that matches or surpasses that of traditional precious metal catalysts.

1.3 Background

In 2007, the U.S. Department of Energy (DOE) investigated the cost of PEFC components and identified that 56% of the cost comes from the electrocatalyst [1]. The electrocatalysts vary from one type of PEFC to another but typically contain platinum on carbon material for both the anode and the cathode. Platinum has long been utilized as an integral material for the electrocatalyst and is regarded irreplaceable due to its high performance and outstanding durability. The increasing cost for platinum hinders commercialization of the fuel cell. Because of this, there has been incredible strong push in the last few decades to produce cheaper catalysts materials to lower the current unacceptable cost of fuel cells to commercialize fuel cell technologies [2].

Of the two half-cell reactions occurring in the fuel cell, the cathodic reaction is said to be the limiting reaction. The cathodic reaction, also known as oxygen reduction, is prone to high overpotentials for the reaction and slow reaction kinetics [3, 4]. Therefore, the cathodic catalyst has often required more platinum than the anodic catalyst. Most pursuits to reduce/eliminate the platinum content in fuel cell catalysts have focused on the cathodic side where the ORR takes place. Two main strategies have been proposed to deal with the increasing precious metal costs for fuel cell catalysts [5]:

(i) Decrease the loading of precious materials on ORR catalyst, and,
(ii) Develop NPMCs to complete the ORR.

The former proposal aims at increasing the platinum utilization of the cathode catalyst such that the active electrochemical surface area of platinum can be maximized. Practically, this method has been carried out by utilizing several different techniques. One technique is to disperse platinum nanoparticles onto the carbon support such that the resulting platinum particle sizes are significantly small. This method has yielded only mediocre results [6-8].

Another method couples platinum with other materials and supports to increase platinum utilization to assist in the removal of hydroxides from the platinum surface to increase the availability of platinum site. Materials such as ruthenium, tin, and tungsten etc. have been used [9-13]. The work from these two methods has resulted in the development of ultra-low platinum loading catalysts for the ORR and show dramatic decreases in platinum loadings with minimal

performance losses. However, due to rapidly increasing cost of platinum, the work in this area has been negated over time by the change of platinum price.

Many research institutions have tried to develop NPMCs which are active for the ORR with performances similar to platinum. Of these two proposed alternatives, the latter choice is the optimal solution for long-term development of fuel cells catalysts. Still, non-precious metal catalysts lack the performance and stability of platinum catalysts, an on-going issue that is being addressed in today's research [2, 14].

1.4 General Fuel Cell Reactions

In a typical H_2/O_2 fuel cell, hydrogen gas is fed into the anode where it undergoes the half-cell reaction described in Equation 1.

$$H_2 \rightarrow 2H^+ + 2e^- \qquad E^0_{25°C} = 0 \text{ V} \qquad (1)$$

Where E^o is the half-cell potential versus a reversible hydrogen electrode (RHE). From this reaction, a single hydrogen gas molecule is dissociated into two protons and two electrons. The protons migrate through a semi-permeable membrane whereas the electrons travel around the cell through an external circuit to complete the load. The electrons and protons reconvene at the cathode where oxygen is introduced into the cell and react to form water [2]. This half-cell reaction is described in Equation 2.

$$2H^+ + ½O_2 + 2e^- \rightarrow H_2O \qquad E^0_{25°C} = 1.229 \text{ V} \qquad (2)$$

Thus, the overall reaction is shown in Equation 3:

$$H_2 + ½O_2 \rightarrow H_2O + \text{heat} \qquad E^0_{25°C} = 1.229 \text{ V} \qquad (3)$$

As can be seen, the only products from this reaction are water and heat. Because of this, fuel cells have been heavily promoted as zero emission energy devices [2].

Two simultaneous processes are usually observed which occurs in discrete steps. The first is the production of water which occurs through a more efficient 4-electron process pathway (Equation 4), and the second is a 2-electron pathway producing hydrogen peroxide (Equation 5).

$$H_2O_2 + 2H^+ + 2e^- \rightarrow 2H_2O \qquad E^0_{25°C} = 1.76\ V \quad (4)$$

$$O_2 + 2H^+ + 2e^- \rightarrow H_2O_2 \qquad E^0_{25°C} = 0.70\ V \quad (5)$$

The optimal pathway is the complete reduction to water. High yields of hydrogen peroxide not only leads to low energy conversions but also produces a reactive intermediate product that can form harmful free radical species [2] that leads to membrane degradation. Figure 1 shows the reaction pathways of O_2 and how they can be reduced to form H_2O through a 4-electron pathway or H_2O_2 by a 2-electron pathway.

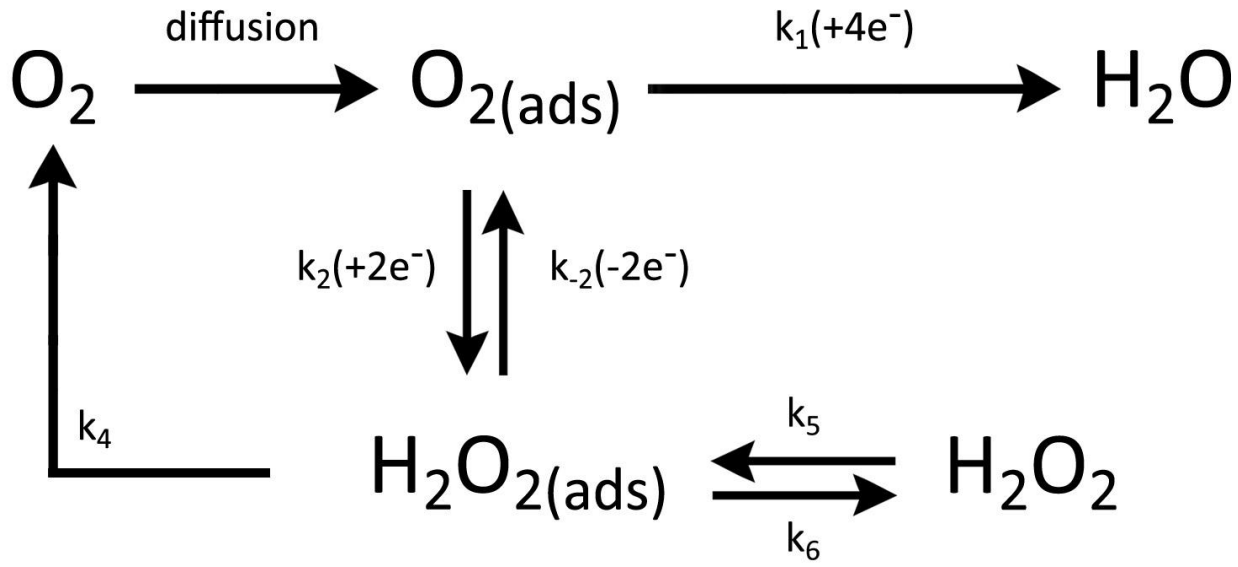

Figure 1: Reaction pathways for the reduction of oxygen in a fuel cell

1.5 Previous Work and Literature Review

Since 1964, Jasinski observed that cobalt phthalocyanine could weakly catalyze the ORR. Prior to this, only Pt/C and precious metal catalysts had been recognized as possible ORR catalysts in acidic media [15]. Jasinski's discovery allowed researchers to develop Fe-N_4 or Co-N_4 macrocycles on carbon supports as catalysts. The use of macrocycles was considered expensive and it wasn't until Yeager who discovered that ORR activity could be achieved by heat-treating a metal precursor with a nitrogen and carbon source. This high temperature pyrolysis was usually conducted at temperatures >500^{o}C in an inert gas to protect the catalyst from burning. Now, the field of NPMCs has rapidly been expanding as researchers are finding different and new nitrogen and metal precursors to deposit onto carbon substrates [5].

Well known reviews have been published regarding these non-platinum/non-precious metal ORR catalysts including one from our group. These reviews extensively outline several directions which have been explored and the current trends in this research [14, 16, 17]. Briefly some of the work done over the past few years is described here.

Although the non-precious metal catalyst work done has yielded significant results, none has shown better activity or stability compared to platinum based catalysts. These types of structures can be classified into different categories: 1) macrocycle N_4 compounds, 2) non-precious transition metal chalcogenides, metal oxides, carbides, nitrides, oxynitrides and carbonitrides, 3) conductive polymers and 4) enzymatic compounds [16].

It has generally been determined that the activity seen by most NPMCs involves a metal precursor. Although it is still unclear as to what role the metal provides, some believe that the metal is crucial in the active site and exist in these Fe-N_4 or Fe-N_2 structures, while other believe that the metal precursor only serves to facilitate in the formation of active sites and does not provide any functionality in the reduction of oxygen [18]. As evidence for the latter, metal-free catalysts were synthesized, which have shown activity for the ORR without any metal loading. Nevertheless, metal containing non-precious catalyst have much higher activity for the ORR. There have been many studies to optimize the type of metal, the metal precursor, the loading and particle size for each catalyst system with respect to the resultant catalytic activity and stability. Several different types of metals have been shown to work with the ORR including Fe [19-23],

Co [19-21, 23-26], Ni [19, 23, 25, 27, 28] and Cu [19, 23, 25, 27]. Many of these studies have compared different metals and metal precursors and have shown Fe with a consistently higher activity than the rest. In a review by Bezerra *et al.* [5] the optimum metal loading in Fe catalysts has been experimented to be 0.2 – 4 wt%. Higher iron loading leads to agglomerates of iron. It has also been noted that upon pyrolysis of these catalysts, graphitized carbon may encapsulate these iron nanoparticles and hence change the electrocatalytic properties of the carbon-iron system, making it more favourable for the reduction of oxygen [29].

The carbon support has also been investigated by many researchers and has a direct impact on the overall catalyst performance. Carbon black is almost predominately used as a catalyst support due to its chemical inertness, electroconductivity, abundance, versatility, and environmental friendliness. There are many types of carbon black made with different methods [30]. Vulcan XC-72 has been a well-used material, but recently, higher surface area carbons have been becoming more popular such as Black Pearls 2000. With the increasing research into nano-designs and nanostructures, many new carbon structures have been explored in the past couple of decades that have replaced traditional carbon blacks. These include graphitized carbon [31], highly mesoporous carbons [32-35], carbon nanotubes [36-39], carbon nanofibres [40-43] and even carbon nano-onion like structures [44]. These structures usually have the properties of increased volume-to-mass aspect ratio, higher surface areas, and greater electroconductivity. In addition, these structures can be synthesized or post-treated to give heterogeneous functionalities, for example, nitrogen doped carbon nanotubes [45]. However, not all researchers are satisfied with the properties of carbon. Carbon is susceptible to the carbon oxidation reaction at voltages higher than $E^o > 0.207$ V and this rate of corrosion is much more severe in operating fuel cells with increased temperature and high potentials. This corrosion can cause efficiency losses of the fuel cell and degradation of the catalyst support possibly resulting in catastrophic failure of the fuel cell stack. Many researchers have investigated alternative support materials such as TiO_2 [46], indium tin oxide [47], tungsten oxide [48-50] or zirconia oxide [51]. These supports usually have increased conductivity, better mechanical properties, and higher thermal stability, and may have additional benefits for a fuel cell catalyst support such as proton conductivity. These supports usually lack catalytic site dispersion and may not form non-precious metal catalyst active sites with Fe-N_x complexes.

It is well known that the variant of nitrogen precursor used will greatly affect the ORR performance of the catalyst. Numerous nitrogen precursors have been tried using a variety of different synthesis techniques. Many researchers have found that the activity of the NPMC is highly affected by the nitrogen content, therefore, some researchers aim at trying to achieve the maximum nitrogen content into their catalysts; however there are structural limitations in this direction. Some of the more successful nitrogen precursors include ethylenediamine [52-57], nitroaniline [58], 1,10-phenathroline [15, 59-61], polyacrylonitrole [19, 26, 62-64], ammonium iron sulfate [65, 66], acetonitrile [28, 62, 67, 68], and ammonia [35, 61, 62, 69-82]. Further investigation into the carbon black and nitrogen precursors are discussed in the following sections.

1.5.1 Ketjenblack as a Carbon Blacks Support

The carbon black support is a critical component for the electrocatalyst in PEFCs. The carbon black provides the essential pathway of electrons to the active site. Several different carbon blacks are used for PEFC catalyst applications. These carbons vary in sulphur, ash, moisture content, porosity, surface area, and electroconductivity. Ketjenblacks, which are used exclusively for the work in this thesis, are a commercially available carbon black from Akzo Nobel. They are commonly used for electroconductive polymers. Due to their high electroconductivity they are also well suited for electrochemical applications. The main features which make them attractive for electrocatalyst applications are their low ash content, large pore volume and high surface area. The properties of two types of Ketjenblacks (Ketjenblack EC-600JD (KJ600) and Ketjenblack EC-300J (KJ300)) are summarized along with those of two well-known carbon blacks commonly used for catalyst applications (Black Pearls and Vulcan XC-72) in Table 1.

Table 1: Conductive carbon black properties summary

Catalyst	BET Surface Area (m^2/g)	Pore Volume (cc/g)	Ash Content (wt %)	Common Uses
Ketjenblack EC-600JD	1400	4.80-5.10	< 0.1	Thermoset, thermoplastic polymers [83]
Ketjenblack EC-300J	800	3.10-3.45	< 0.05	Thermoset, thermoplastic polymers [84]
Vulcan XC-72	267	0.46	0.1	Electrical cables, electrostatic discharge products, plastics
Black Pearls 2000	1475	~2.67	0.36	Rubbers, and anti-static discharge properties [85, 86]

In several works, the effect of the carbon black support on the ORR performance has been tested. Medard *et al.* [72] conducted a study of several Fe-based catalysts for the ORR on various carbon blacks. With 0.2 wt% of Fe loading, they found that the order of catalytic activity for the ORR was Sid Richardson Carbon Corporation RC1 > Sid Richardson Carbon Corporation RC2 > HS300 > Acetylene Black > Vulcan XC-72R > Black Pearls 2000 > KJ600 > Printex XE-2. The study concluded that the carbon black support was important on the activity as well as the selectivity of the catalyst. The most important parameter for the activity, however, was the final nitrogen content on the carbon surface. The authors hypothesized that the increase in nitrogen attributed to the formation of Fe-N_2/C and Fe-N_4/C catalytic sites. They did not conclude that the surface area had an obvious influence on the catalyst performance.

In another study, N.P. Subramanian *et al.* [56] studied the effect of carbon surface area and pore size distribution on Co- ethylenediamine (EDA) based catalysts on three different carbon blacks (KJ300, Black Pearls 2000 and Vulcan XC-72). They showed that the resulting catalyst activity of the Co-EDA/C catalyst decreased with the increase of the amount of quinone groups as follows on the oxidized carbons: KJ300 > Black Pearls 2000 > Vulcan XC-72. This was due to higher selectivity for the 4-electron reduction to water. The quinine groups were added through a HNO_3 treatment of the carbons prior to catalyst synthesis. Although, Black Pearls 2000 carbons show much higher surface area, the nitric acid is not able to access the micropores that are less

than 2 nm in diameter. Subsequently, Ketjenblack EC-300J is mainly mesoporous (with pore diameters ranging from 2 – 50 nm), was able to form a greater amount of quinine groups on the edge of the basal plans when treated with nitric acid.

In an influential study conducted by Lefevre *et al.* [15], several of their experiments lead to two factors, which they claim are requirements for producing active Fe-based catalysts for the ORR: 1) disordered carbon content, and 2) micropores in the catalysts. In an attempt to follow the guidelines produced by this work as well as integrate high quinone groups on the carbon surface, Ketjenblack carbon blacks were primarily used as the carbon substrates for this work.

1.5.2 Ethylenediamine (EDA) as a Nitrogen Precursor

EDA is often used as a nitrogen precursor for electrocatalyst synthesis. NPMCs utilizing EDA have shown impressive ORR performance for cathodic electrocatlaysts in acid electrolyte [38, 87] and alkaline fuel cells [18, 88]. Its high performance for the ORR has been attributed to its high nitrogen to carbon ratio, although other precursors with high nitrogen to carbon ratios do not display such high performances. Synthetic techniques utilizing EDA as a nitrogen precursor often involve coating the precursor materials onto a carbon black followed by a heat-treatment. However alternative techniques have been reported including sol gel, no heat-treatment, and using EDA to form alternative carbon structures such as nitrogen-doped carbon nanotubes [38, 89].

1.5.3 Cyanamide as a Nitrogen Precursor

In section 4, cyanamide as a nitrogen precursor for NPMCs is used. Cyanamide is an organic compound with the chemical formula CN_2H_2. To this researcher's knowledge, the only previous work done with cyanamide as a precursor for NPMCs is the work conducted by the Los Alamos lab [90, 91]. Their research claims that cyanamide was a nitrogen precursor capable of forming graphitic-C_3N_4 under certain pyrolysis conditions [92]. Since high nitrogen content was associated with high ORR activity in non-precious catalysts, it was thought that cyanamide would allow for a high nitrogen content and high ORR activity catalyst. Although the NPMC was able to obtain high catalytic activity, no correlations with high nitrogen content or high pyridinic-N was found. Instead the high activity that resulted from the cyanamide derived

catalyst was attributed to the increased carbon disorder and oxygenated functional groups found in the catalyst.

1.5.4 Phthalocyanine as a Nitrogen Precursor

Phthalocyanine structures have been investigated as NPMC structures for some time now. Their planar geometry, electrical conductivity, nitrogen, and thermal stability make them a unique structure for application into fuel cell catalysts. In addition these structures form coordination complexes with many metals such as iron, cobalt or cooper which are intensely coloured and often used for dyes and paint applications [93].

In a study conducted by Boston and Bailar [94], they discuss the synthesis of polymetric phthalocyanine structures either in stacked or sheet forms. They discuss the various polymer structures existing as either a bridged, fused or stacked form. In their work they note the difficulties in polymerization and characterization of these structures are mainly due to the inability to dissolve the phthalocyanine. Characterization of these structures usually relies on some form of spectroscopy as elemental analysis and end-group titration are not effective for large polymetric chains. Fourier transform infrared spectroscopy (FTIR) was therefore utilized to determine the amount of residual monomer in the reaction batch, and found that all the monomer has been consumed and that the polymerization has occurred. However, the yield of polymer is quite low and vigorous purification procedures are needed to obtain a high quality polymer.

Lalande *et al.* [29] also conducted experiments with iron phthalocyanine seeking to form M-N_4 moiety after pyrolysis treatment. With equivalent metal loading their non-precious catalyst were able to obtain 65% of the catalytic activity of Pt/C catalysts. Upon characterization of their catalyst, they determined that iron was crucial for the activity seen in their catalyst with temperatures above 900^{o}C showing long-term stability after the decomposition of the macrocyclic compound. They claim that for iron to be stable and active for the ORR, it should be engulfed in graphitic carbon where it changes the electroconductive properties of the surface to form catalytic active sites. Figure 2 illustrates the chemical structure of EDA, cyanamide, and phthalocyanine structures discussed in this section.

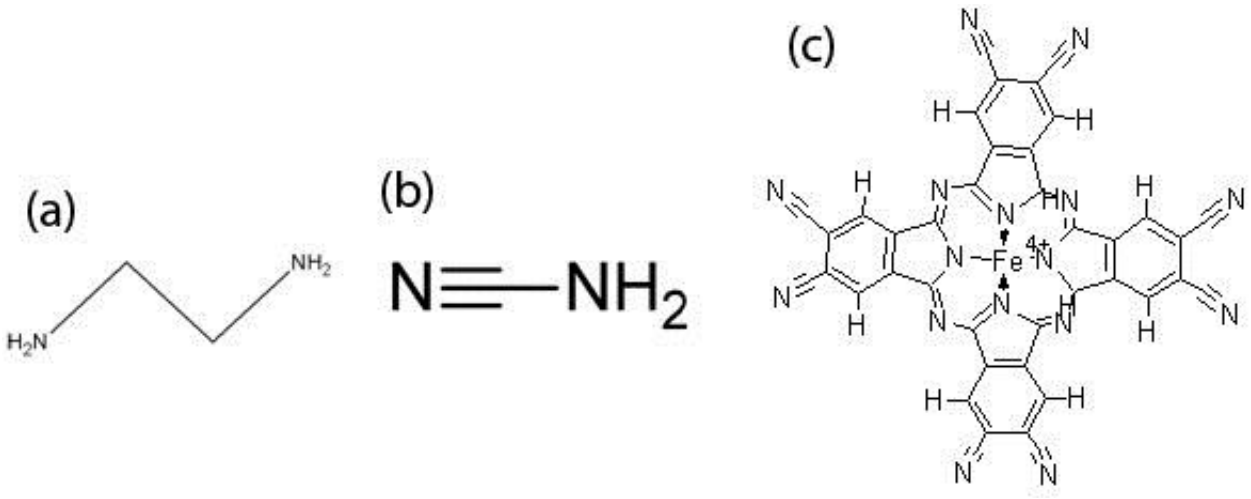

Figure 2: Chemical structures of (a) EDA, (b) cyanamide, and (c) iron phthalocyanine

1.6 Organization of Thesis

The present thesis is divided into six main categories. The first chapter introduced the reader to the scope and objectives of the work as well as background information in fuel cell catalysis. Chapter 1 contains a literature review on past work done in the field of NPMCs for fuel cells. Chapter 2 discusses most of the theory and analysis techniques that were utilized in the work done for this thesis. The three experiments utilizing EDA, cyanamide, and iron phthalocyanine are described in Sections 3, 4 and 5 respectively. These sections describe the motivation for the work, the experimental procedure, the discussion of the results and the conclusions arrived at. The work described in sections 3 and 4 have been published previously, while the work in section 5 is awaiting publication at the time of writing. Section 6 summarizes the important results and some discussion on the future direction that the work may take.

Section 2: Experimental Characterization Techniques

2.1 Physical Characterization Techniques

In the following section, the experimental methods, instrumentation and the background theory of the analysis used for various physical characterizations of the synthesized catalysts in this work will be discussed. X-ray photoelectron spectroscopy, transmission electron microscopy, scanning electron microscopy, X-ray diffraction, Fourier transform infrared, thermogravimetric analysis and nitrogen adsorption analysis were used in this work.

2.1.1 X-Ray Photoelectron Spectroscopy

X-ray photoelectron spectroscopy (XPS) is a quantitative spectroscopic technique that measures elemental composition, chemical states and electronic states of samples. The principle of the technique relies on irradiating the sample with a beam of X-rays and observing the number of electrons and the kinetic energy of the material that result [95].

Figure 3 shows a schematic of an X-ray photoelectron spectrometer. The devices commonly utilized 20-200 μm beams of monochromatic aluminum K-alpha waves. The device must be enclosed in an ultra-high vacuum to avoid any interference from the atmosphere. Due to the small diameters of the orbitals, XPS is unable to detect elements with an atomic number less than 3. And depending on the density of the sample, XPS is only able to obtain a surface analysis no more than 1-10 nm deep into the sample. Hence, XPS is commonly used to measure inorganic compounds, metal alloys, semiconductors, polymers and catalysts [96, 97].

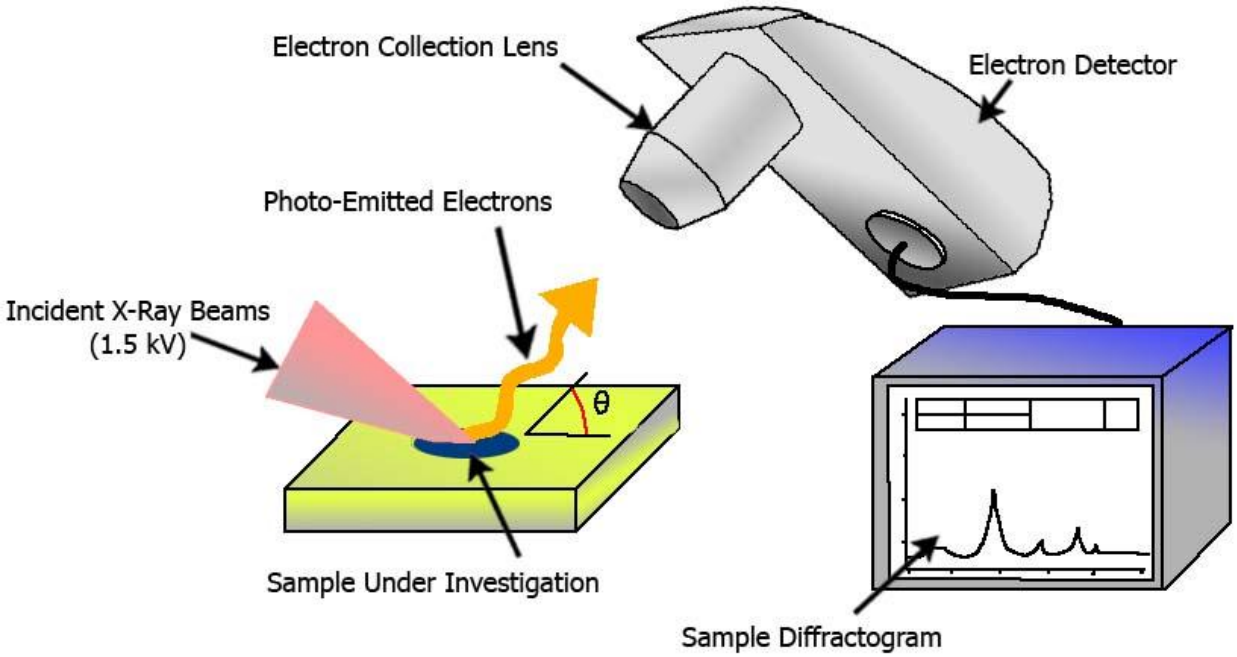

Figure 3: XPS equipment schematic

XPS was used in this work to detect surface concentrations of different elements. For catalysts synthesized in this work, iron, nitrogen, oxygen and carbon were of particular interest. XPS can also quantify the different types of nitrogen bonds including pyrrolic, quaternary, pyridinic and pyridone. The type of nitrogen bonded onto the surface of the carbon support is said to be an influencing factor in the active site formation of Fe-N catalysts and thus XPS is an integral part of the catalyst characterization.

2.1.2 Scanning Electron Microscopy/Energy Dispersive X-Ray

Scanning electron microscopy (SEM) is a well-known physical characterization technique that is utilized for observing the morphology of a sample at high magnification. SEM can be coupled with energy dispersive X-ray (EDX) analysis to determine elemental composition as well as other properties such as electroconductivity of a sample. The device takes advantage of electrons having a particular wavelength to act like photons [98]. These wavelengths were hypothesized by de Broglie stating that the wavelength of matter is inversely proportional to the momentum of a particle and that the frequency is directly proportional to the particle's kinetic energy. Mathematically, these relationships are stated as Equation 6 [99]:

$$\lambda = \frac{h}{p} \; and \; f = \frac{E}{h} \tag{6}$$

Where h is Planck's constant. Utilizing the equations of special relatively, these equations are also written as Equation 7:

$$\lambda = \frac{h}{\gamma m v} = \frac{h}{mv}\sqrt{1 - \frac{v^2}{c^2}} \; and \; f = \frac{\gamma m c^2}{h} = \frac{1}{\sqrt{1 - \frac{v^2}{c^2}}} \cdot \frac{mc^2}{h} \tag{7}$$

Where m is the particle's rest mass, v is the particle's velocity, γ is the Lorentz factor, and c is the speed of light in a vacuum.

Since the emitted electrons thus have smaller wavelength than photons, SEM can observe higher resolutions and greater magnifications than an optical microscope. The detector equipment is very sensitive being able to reveal detail up to 1-5 nm in size and thus must operate within an ultra-high vacuum for accurate measurement. The electrons that are emitted to interact with the sample can be captured by various detectors and can yield different results for each: secondary electrons (inelastic collisions), back-scattered electrons (elastic collisions), characteristic X-rays, transmitted electrons. Each of these emissions occurs because of different energy levels of the incident electron. For example, low energies will promote secondary electron emission while higher energies will promote X-ray emission.

For catalyst characterization, SEM can be utilized to investigate the surface porosity of the carbon surface, the metallic particles, the uniformity of the coatings and substituent's, general defects and the presence of contaminants.

2.1.3 Transmission Electron Microscopy

Transmission electron microscopy (TEM) is a microscopy technique where a beam of electrons is transmitted through an ultra-thin specimen. Similar to SEM, electrons are focused and emitted to interact with a specimen – the electrons are focused onto an imaging device such as a fluorescent screen, a layer of photographic film or to be detected by a sensor such as a CCD camera. Electrons are generated by the microscope through a process known as thermionic

emission from a tungsten filament, in the same way as a light bulb. The electrons are accelerated by an electric potential which are focused by numerous lenses through the sample and onto the image capturing device [100].

The manipulation of the electron beam and hence the image captured by the detector can be achieved by two methods. The first method is to have the electrons interact with a magnetic field which can move and manipulate the beams based on the right hand rule. The magnetic field can act as a lens with variable focusing power. The second method to adjust the beam is by using electrostatic fields that can cause electrons to be deflected at a constant angle [101]. Both these methods used together can allow two deflection beams with a small intermediate gap to cause a TEM beam shift. This gives TEM a distinct advantage over optical microscopes since the beam path can be easily changed by changing the field strength or disabling the field entirely by rapid electrical switching.

TEM is capable of much higher resolution than light microscopes or SEM due to the small de Broglie wavelength of electrons. At small magnifications TEM image contrast is due to the absorption of electrons onto the specimen surface, while at higher magnifications complex wave interactions are responsible for a clear modulated image. The maximum resolution that can be obtained from a light microscope is limited by the wavelength of a photon:

$$d = \frac{\lambda}{2n \sin \alpha} \tag{8}$$

Where λ is the wavelength of the photon, n is an integer equal or greater than 1, and d is the theoretical maximum resolution. However by use of the de Broglie wavelength of matter, for instance electrons, this maximum resolution is greatly increased to be able to distinguish even columns of atoms of a few nanometers.

TEM is utilized to observe the surface morphology of the catalyst structures. The high resolution of TEM imaging allows for investigation of pore structure, surface coatings, particle size and particle distribution determination. Figure 4 is a typical schematic of a transmission electron microscope.

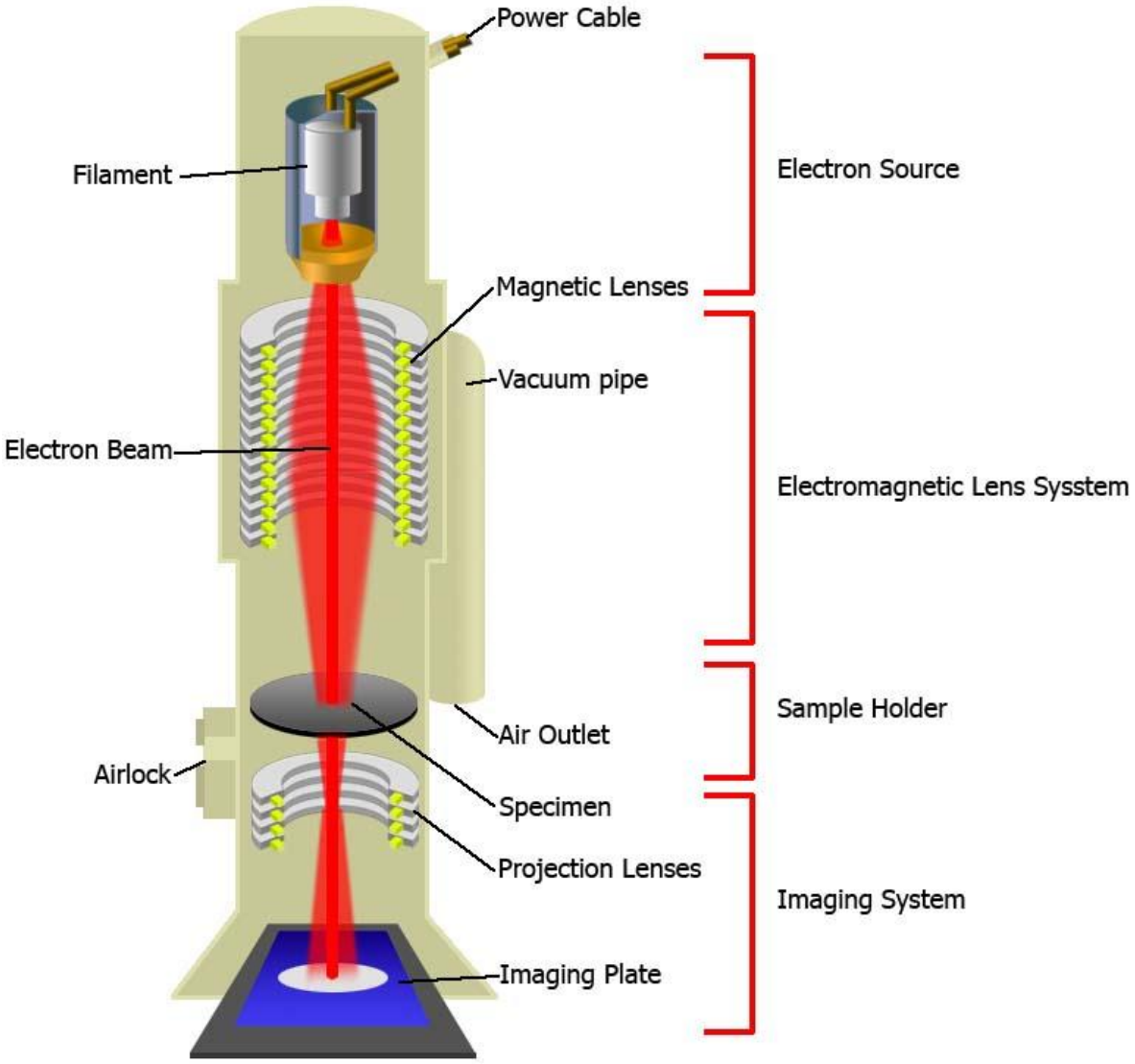

Figure 4: Schematic of TEM equipment

2.1.4 X-Ray Diffraction

X-ray diffraction (XRD) is a non-destructive X-ray scattering technique which physically characterizes a sample based on crystallographic structure, chemical composition and physical properties. The principle theory of X-ray diffraction relies on an X-ray beam hitting a sample and detecting the intensity at the angle of reflection. The reflected X-rays give information based on the atomic structure of the sample materials which is caused by the elastic scattering of X-rays from the electron clouds of the species within the sample [102].

XRD is often used to identify what elements a heterogeneous mixture is composed of, the crystalline structure of those elements, as well as, the crystallite size or grain size. The X-ray diffraction equipment usually controls the position of the X-ray beam (incident ray) and the position of the detector (reflected ray) and records the observed intensity at the detector. In this way, a plot called a diffractogram is obtained with the angle in 2θ on the x-axis versus intensity which is plotted on the y-axis. The resulting diffractogram can then be compared to diffraction data in a well-known database to determine what species or molecules exist in a sample. With techniques such as Rietveld refinement, the diffractogram can also provide lattice structural information.

XRD is also a common method to determine particle sizes of crystalline structures and metals/metal alloys. For such analysis, Scherrer's Equation can be applied to a specific peak seen in the diffractogram and is shown in Equation 9 [103]:

$$d = \frac{K\lambda}{\beta \cos\theta} \tag{9}$$

Where d is the particle diameter (nm), K is known as a dimensionless shape factor, λ is the wavelength of the incident X-rays (0.154 nm for Cu-Kα), β is the full width half maximum of the diffraction peak (rad) and θ is the angle corresponding to the peak being analyzed. There are several similar XRD techniques based on the same theory which are utilized for specific analysis such as small angle X-ray scattering (SAXS) and wide angle X-ray scattering (WAXS). The former relies on scattering angles in the range of 0-5^{o} whereas WAXS is typically lager than 5^{o} [103].

XRD is used for catalyst characterization for the identification of specific metal and composite characterizations. XRD determines what structures of specific materials exist within the catalyst layer and crystalline parameters can also be determined. From this knowledge grain size of metallic particles, graphitic order of the carbon black and lattice structure of the metals can be analyzed.

2.1.6 Thermogravimetric Analysis

Thermogravimetric analysis (TGA) is a destructive analysis technique which allows the experimenter to determine the change in weight of a sample in response to a change in temperature. The instrument typically comprises of a sample holder which continually measures the mass of the sample, and a combustion chamber, which heats/cools the sample to the desired temperature. TGA has often been employed in several scientific fields to determine the decomposition temperature of materials, thermal stability, adsorbed moisture content, relative organic composition, required reaction temperatures or reaction kinetics. For these purposes, it is a common technique in the fields of polymers, materials science, inorganic and organic chemistry and corrosion science [107].

When conducting a TGA experiment, there are several important factors that must be considered. The temperature can be controlled fairly accurately depending on the power of the furnace that is being used to heat the combustion chamber and the efficiency of the cooling gas/system, thus, the user has fair control over the temperature profile, the heating and cooling rates, and the type of gas being fed through the system. The gas used to flow through the reaction chamber during an experiment is worth discussing as it can drastically affect the sample weight change characteristics. Typically heating profiles are burned in oxygen or air to determine thermal stability, however, an inert gas such as nitrogen, helium or argon is commonly used to give different information.

Interpretation of the results can often be complicated as many temperature-weight profiles may look very similar for samples of the same nature. Therefore it is often helpful in terms of analysis to use the derivative weight change of the sample and compare with other samples. Figure 5 illustrates a simple TGA plot where the sample was heated to 900^{o}C in air. Both the weight versus temperature and the derivative weight versus temperature curves are shown. The sample demonstrates some characteristic behaviours often seen for carbonaceous materials. From room temperature to 400^{o}C, there is only slight mass loss and is most likely due to water or surface group removal on the material. Starting at 400^{o}C, there is an increase in mass loss as the material starts to decompose and burn. This rapid weight loss continues to about 750^{o}C where the percentage mass versus temperature curve levels off. At this point, the organic carbon material is

practically completely burned off and trace residuals of metals, ash and other inorganic materials remain in the sample holder.

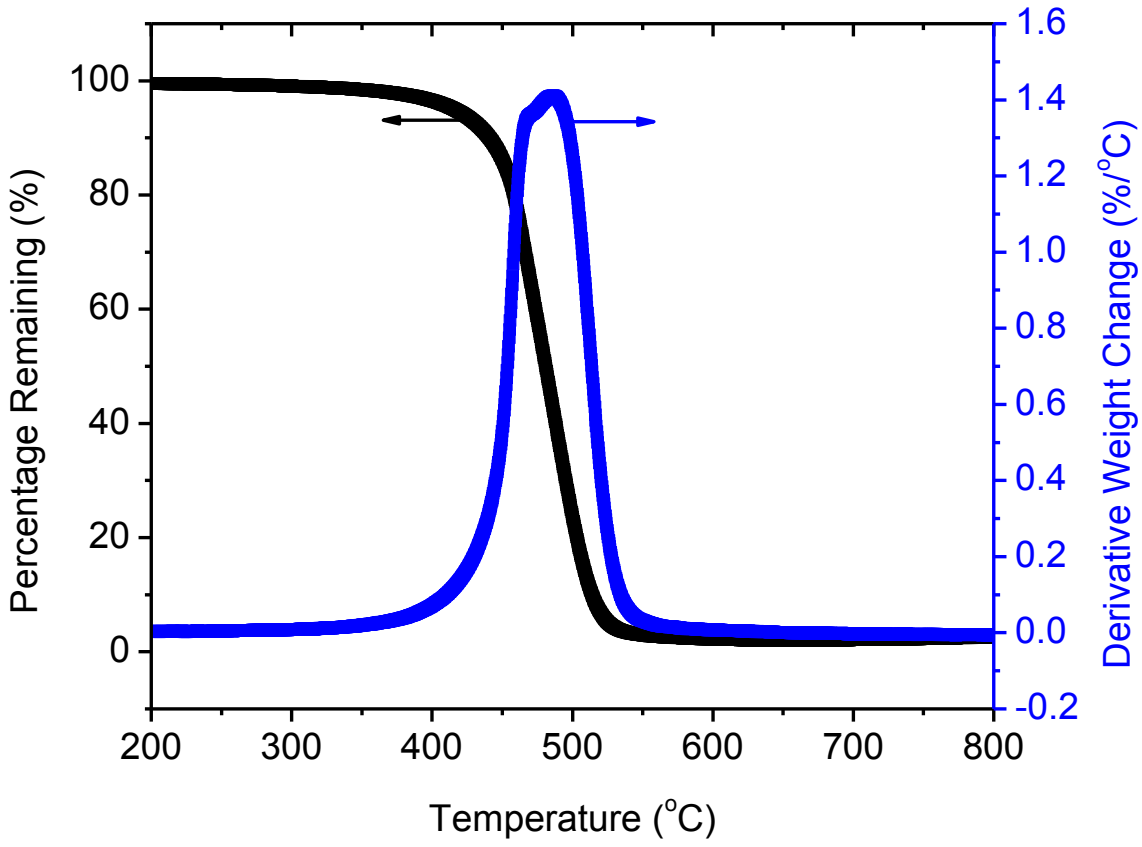

Figure 5: Typical TGA plot of carbonaceous materials

Thermogravimetric analysis is used in this work to provide insight on the thermal stability and metal content of the catalyst samples. A more thermal stable catalyst begins decomposition or combustion at higher temperatures and may combust less rapidly depending on the catalyst structure. The catalyst sample being burned, are mainly composed of carbonaceous matter, with varying levels of graphitization, surface group functionalization, metal content and edge plane exposure. TGA was conducted on these samples to hopefully provide insight into these parameters. Specific experimental details are described in the experimental section.

2.1.7 Nitrogen Adsorption Analysis

Nitrogen adsorption analysis (NAA) or BET theory utilizes the physical adsorption of gases onto solid materials to measure the specific surface area of the solid. The underlying theories were founded in 1938 by Stephen Brunauer, Paul Hugh Emmett and Edward Teller and hence the term BET has been coined by the initials of their last names in recognition for this work in the field.

The principles of BET build upon Langmuir theory; the following equation can be expressed [108]:

$$\frac{1}{\upsilon[(P_o/P)-1]} = \frac{c-1}{\upsilon_m c}\left(\frac{P}{P_o}\right) + \frac{1}{\upsilon_m c} \tag{10}$$

Where P and P_o are equilibrium and saturation pressure of the adsorbate at a specific temperature, υ and υ_m are the adsorbed gas quantity (mL), and the monolayer adsorbed gas quantity and finally c is the BET constant expressed Equation 11 [108]:

$$c = exp\left(\frac{E_1 - E_L}{RT}\right) \tag{11}$$

Where E_1 is the heat of adsorption of the first layer (J/mol) and E_L is the heat of adsorption for the following layers and is also equal to the heat of liquefaction (J/mol).

BET theory is valid under three hypothesis: 1) gas molecules physically adsorb on a solid in layers infinitely, 2) there is no interaction between each adsorption layer, and 3) Langmuir theory can be applied to each layer [108].

From the adsorption/desorption isotherm, a BET plot can be formulated with $1 / \upsilon[(P_o / P) - 1$ on the y-axis and P/P_o on the x-axis. A linear relationship on the range of $0.05 < P/P_o < 0.35$ is obtained with a slope of A and a y-intercept of I. Thus the values of υ_m and the BET constant, c, can be calculated for Equation 10 by Equation 12 and Equation 13:

$$\upsilon_m = \frac{1}{A+I} \tag{12}$$

$$c = 1 + \frac{A}{I} \tag{13}$$

Finally a total surface area, $S_{BET,Total}$ (m^2), can be evaluated for the total surface area of the solid material by physical adsorption of gas molecules by Equation 14:

$$S_{BET,Total} = \frac{(\upsilon_m N s)}{V} \tag{14}$$

Where N is avagadro's number (molecule/mol), s is the adsorption cross section of adsorbing species (m^2), V is the molar volume of the adsorbing species (m^3/mol). BET analysis is useful in catalysis for observing the specific surface area of carbon blacks. High activity catalysts usually try to maximize the active site density on the surface of the carbon supports and hence try to utilize high surface area carbons to functionalize these carbons. NAA was used to measure the surface areas and characterize pore distributions in the carbon blacks and the resulting Fe-N/C catalyst that were made in this work.

2.2 Electrochemical Characterization Techniques

Electrochemical characterization techniques utilized in this work deal with the electrochemical and half-cell reactions. By conducting these electrical experiments information regarding the reaction species, the reaction products, the reaction kinetics, the reactive surface area, the nature of the film and mass transfer limitations can be deduced. The following sections will emphasize the importance of these electrochemical techniques and the analysis methods used in the experiments to characterize the behaviour of the catalyst samples.

2.2.1 Rotating Ring Disc Electrode

The rotating ring disc electrode (RRDE) experiments are one of the key methods for analyzing catalyst electrochemical performance for the ORR. In past literature, RRDE have been used to characterize the onset potential, half-way potential, limiting current density, H_2O/H_2O_2 selectivity, and to determine the electrochemical active surface area of certain catalyst [2]. RRDE experiments can also give information on the electroconductivity and capacitative

behaviour of samples. Repeated cyclic tests also give information on the durability of certain conditions and chemical tolerance of the catalyst to different contaminants. This section discusses the equipment setup, background theory, and analysis techniques of the RRDE experiments utilized in this thesis.

While rotating ring disc electrode (RDE) experiments are commonly carried out using a three electrode system (Figure 6), RRDE experiments add another working electrode in the form of a ring on the working electrode. This means that four electrodes are used to conduct the experiment: two working electrodes, a counter electrode and a reference electrode to which all potential measurements are made. The working electrode for RRDE experiments exists as a glassy carbon disc surrounded by a second input electrode in the form a ring. The glassy carbon is used to deposit a known amount of the catalyst sample whereas the platinum ring collects information on the selectivity of the reaction occurring on that disc. The counter electrode, in this work, a platinum wire, is used to provide or accept electrodes to complete the circuit of the half-cell setup. All three electrodes are immersed in an acidic electrolyte which can either be saturated with oxygen providing the reactant to be reduced, or an inert gas like nitrogen. Saturating the electrolyte solution (0.1 M $HClO_4$ solution in this thesis) and sweeping the applicable potential range allows for the ORR to be measured.

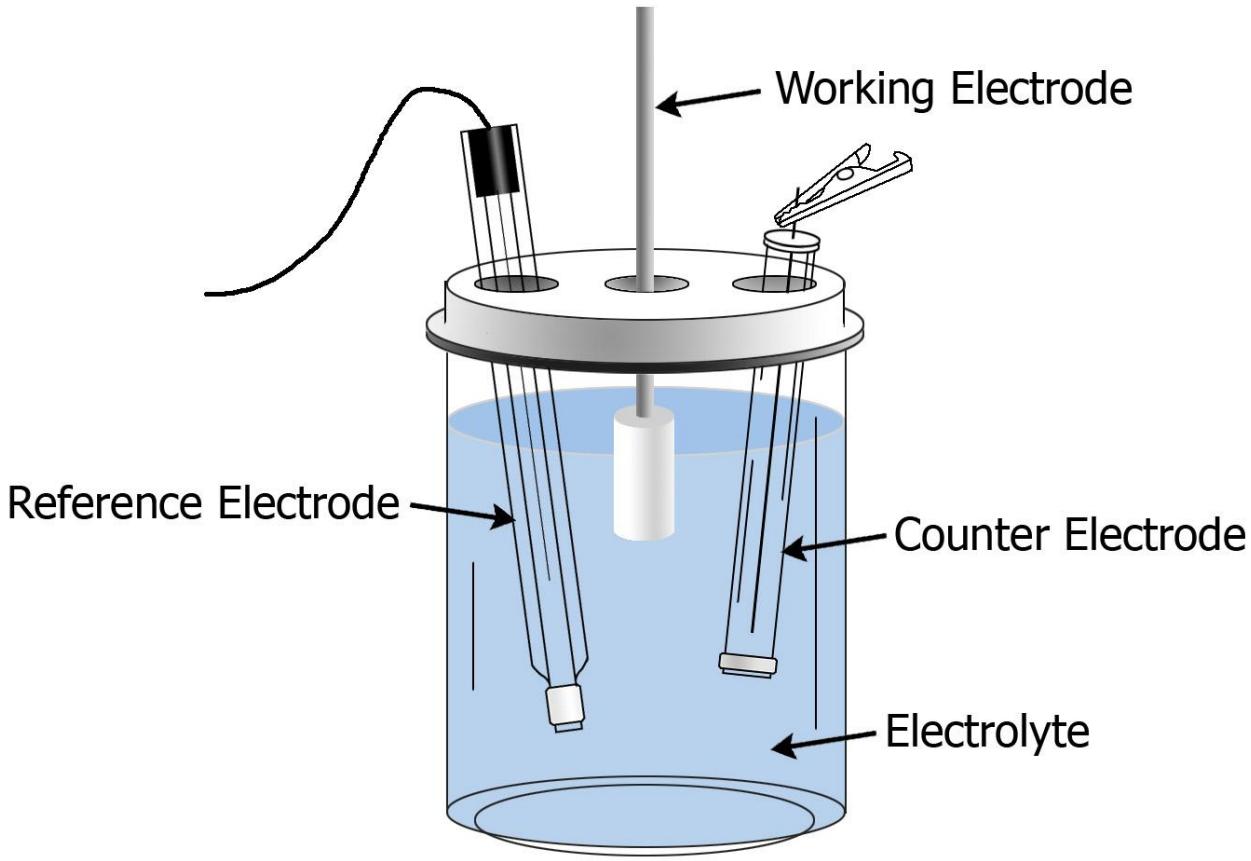

Figure 6: 3 electrode cell half-cell setup

The RRDE system takes advantage of laminar flow properties caused by a spinning electrode. The working electrode is connected to a rotator that can spin at measured frequencies. The rate of rotation allows the solution electrolyte to be forced outwards to the side of the cell; meanwhile bulk solution with saturated gas is driven towards the surface of the electrode. The faster the rotation speed, the higher the bulk convection current towards the working electrode, thus more saturated gas is being provided to the electrode. By providing reactants for this half-cell reaction, a current can be produced at an appropriate voltage, which is determined by the diffusion current and mass transfer limiting current [2]. On surface of the working electrode there is a stagnant reaction layer covering the surface. The reactants transport through this layer by diffusion to react on the electrode. This overall expression for current density at a specific voltage can be expressed by the Koutecky-Levich equation seen in Equation 15:

$$\frac{1}{|i|} = \frac{1}{|i_d|} + \frac{1}{|i_k|} \tag{15}$$

Where i is the overall or total current density, i_d is the diffusion controlled current density and i_k is the reaction kinetics controlled current density.

In a typical RDE experiment the potential of the working electrode is scanned from the potential where no reaction occurs to a potential where the reaction occurs. A limiting current is achieved when the overpotential of the reaction is high enough such that an increase in the overpotential, does not increase the current density at the working electrode. Stated otherwise, the limiting current is achieved when the mass transport rate of reactant is the limiting condition for the generation of current in the system.

This steady-state diffusion-controlled system has been modeled by the Levich equation and is expressed in Equation 16:

$$|i_d| = 0.620nFAD^{2/3}\omega^{1/2}\upsilon^{-1/6}C \quad (16)$$

Where n is the number of electrons transferred in the half reaction, F is the Faraday constant, A is the electrode area, D is the diffusion coefficient of reactant in the bulk solution, ν is the kinematic viscosity, ω is the angular rate of rotation of the electrode and C is the reactant concentration in the bulk solution.

When the overpotential is not sufficient to reduce all the reactant reaching the working electrode, the reaction is said to be within the kinetic current limiting stage where the reaction is limited by the reaction kinetics. In this region, Equation 17 can be used to model the kinetic current density:

$$|i_k| = nFAk_fC \quad (17)$$

Where k_f is a rate constant is a function of the overpotential.

When the working electrode catalyst is coated with a layer of Nafion which is usually the case in RRDE experiments, a third term must be added to model the diffusion of reactant through the Nafion binding film. The resulting Koutecky-Levich expression becomes that shown in Equation 18:

$$\frac{1}{|i|} = \frac{1}{|i_d|} + \frac{1}{|i_k|} + \frac{1}{|i_f|} \quad (18)$$

Where i_f is the diffusion current density of the reactant through the Nafion and can be expressed as that shown in Equation 19:

$$|i_f| = nFAC_f D_f/\delta \quad (19)$$

Where C_f is the concentration of reactant in the Nafion film, D_f is the diffusion coefficient of the reactant though the film and δ is the thickness of the Nafion layer. For simplicity, the kinetic current density is usually much larger compared to both the diffusion and Nafion current densities and hence neglected from the final equation shown in Equation 20:

$$\frac{1}{|i|} = \frac{1}{|i_d|} + \frac{1}{|i_f|} = \frac{1}{|i_d|} + \frac{\delta}{nFAC_f D_f} \quad (20)$$

A plot of current density versus potential for the range of voltages from when the reaction does not occur to the potential where the limiting current is reached is called a polarization curve or ORR curve. These curves are usually done at several rotation speeds of 100, 400, 900, 1600 rpm in O_2 saturated 0.1 M $HClO_4$. A typical example of these types of plots is illustrated in Figure 7. Background currents are subtracted from the plots by repeating the ORR curve in saturated N_2. All potential sweeps are done at a sweep rate of 10 mV/s.

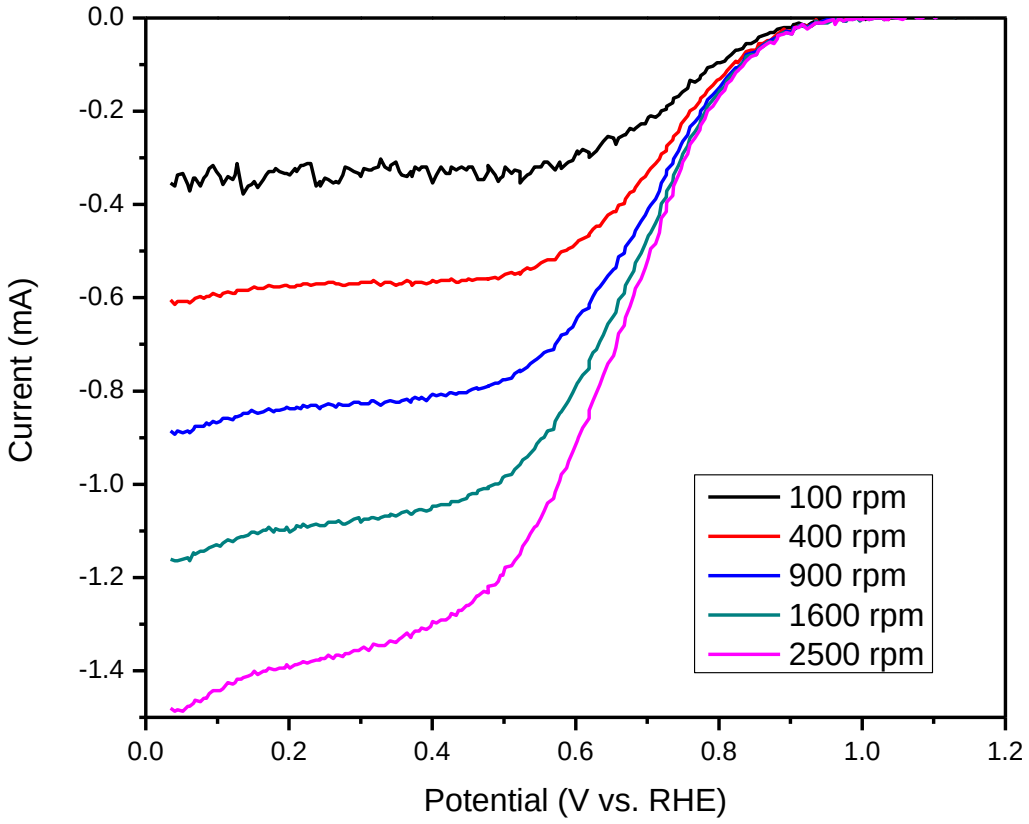

Figure 7: Typical ORR curves from a NPMC

The outside ring electrode consisting of platinum is utilized as an electrode to gather supplementary data to the reaction on the selectivity of the catalyst that has been deposited onto the working electrode. Reduction of oxygen to H_2O and H_2O_2 may happen simultaneously at the working electrode and all the products are pushed outwards towards the ring. The ring electrode is held at a certain voltage capable of reducing the H_2O_2 completely to H_2O.

The number of electrons transferred during the ORR and the selectivity of H_2O_2 during the ORR can be calculated by the following three equations [2]:

$$n = 4|I_D|/\left(|I_D| + (|I_R|/N)\right) \quad (21)$$

$$\%H_2O_2 = 100(4 - n)/2 \quad (22)$$

$$\%H_2O = 100 - \%H_2O_2 \quad (23)$$

Where n is the number of electrons transferred, I_D is the current at the disc electrode, I_R is the current at the ring electrode, N is the collection efficiency which is determined by the manufacturer of the RRDE system (N=0.26 in this work), $\%H_2O_2$ is the selectivity of H_2O_2 of the reaction and $\%H_2O$ is the selectivity of H_2O in the reaction. Thus, a plot of $\%H_2O$ versus potential will determine the yield of H_2O throughout the range of voltages.

For catalyst samples in this work, RRDE testing was the primary performance testing method for electrochemical characterization. RRDE tests would give a quick and repeatable results without having to construct membrane electrode assemblies, which are time consuming and expensive.

2.2.2 Membrane Electrode Assembly Testing

The problem with half-cell testing is that it gives very limited information about the catalytic performance. The actual performance seen in a fuel cell stack using a specific catalyst is much different from RDE and RRDE experiments. To better gauge the fuel cell stack performance, membrane electrode assemblies can be fabricated and test in single cell prototype cells to carry out membrane electrode assembly (MEA) benchmark performances. This is a common procedure carried out by catalyst researchers. However MEA benchmark tests are usually reserved for the most promising catalyst. After creating the MEA stack, a steady-state sweep of the potential while recording the current yields a polarization curve. The operating conditions such as stack temperature, inlet temperatures, humidity and flow rates can be systematically changed to obtain information on the stack performance in relation to these changes. Figure 8 shows a typical polarization curve along with a power density versus current density plot which is often done as well to illustrate optimum power density which can be achieved by the cell.

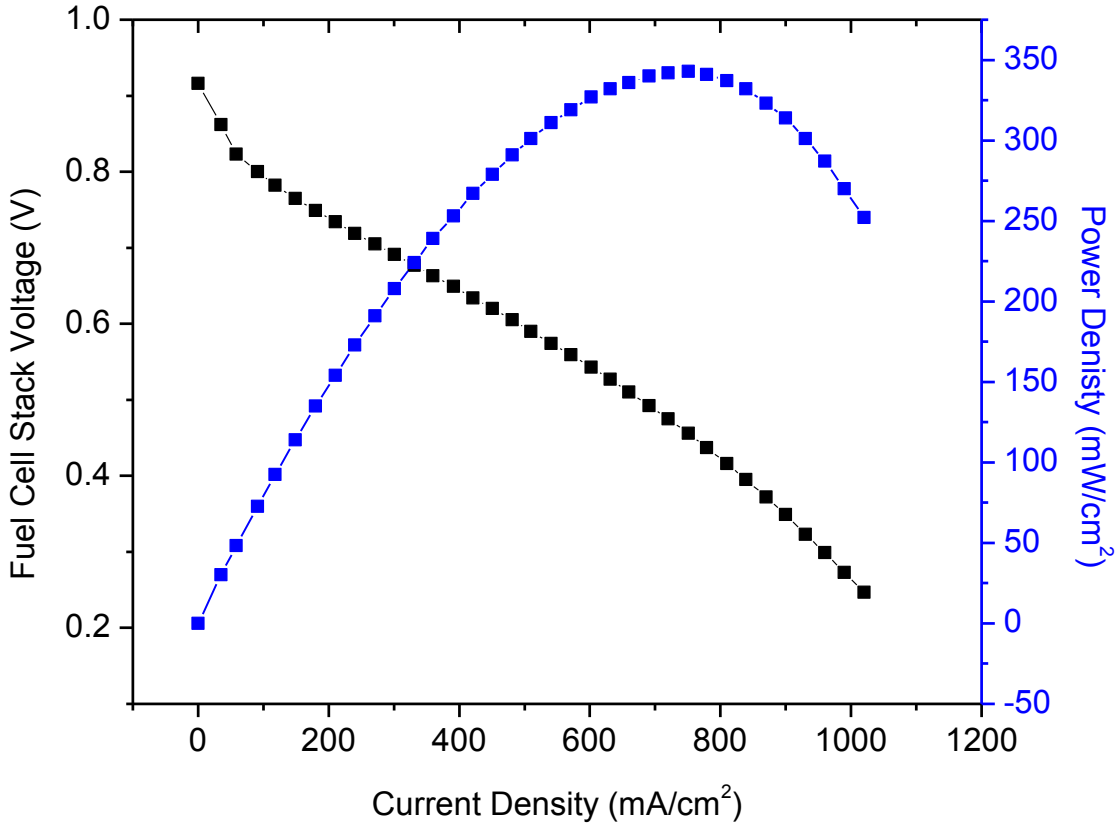

Figure 8: Typical MEA polarization curve with a power density versus current density plot

Fuel cell voltage losses are separated into three regions or categories: 1) activation loss, 2) ohmic loss, and 3) concentration loss. These losses are illustrated in Figure 9. The theoretical open circuit voltage (OCV) should being at E= 1.229 V which is the standard reduction potential of oxygen. At low current densities the cell losses are mainly attributed to sluggish kinetics of the ORR. At intermediate current densities, the voltage usually drops linearly as ohmic losses begin to impede the reaction. These losses are usually caused by the resistance of electrons through the electrolyte and the electrodes. Finally at higher fuel cell voltages, mass transport effects start to be the limiting factor as the reactants are not able to make it to the electrode rapidly enough. This causes a drastic drop in potential.

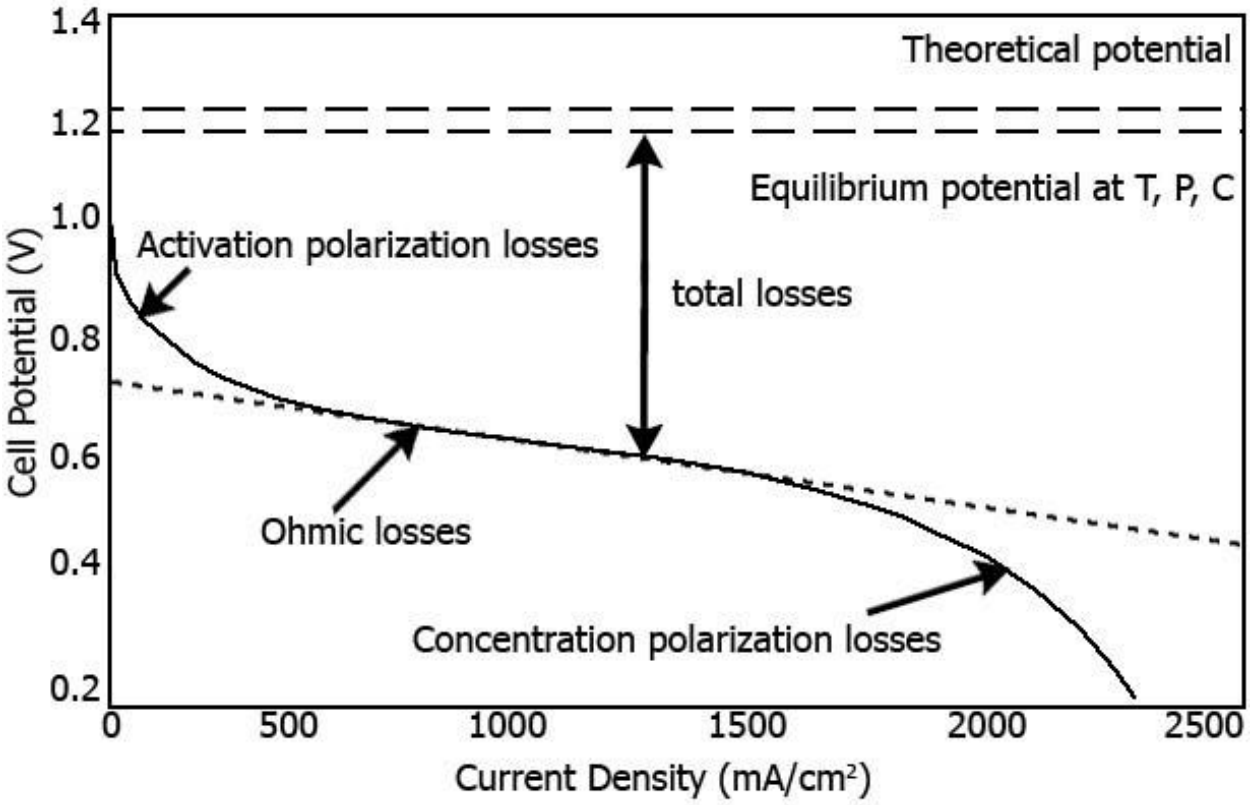

Figure 9: Sample polarization curve, various polarization losses in a fuel cell

The total output voltage of a single cell, can be expressed as the fuel cell OCV minus the combination of attributing losses. This is expressed in Equation 24:

$$E_{cell} = E_{OCV} - \Delta E_{act} - \Delta E_{ohmic} - \Delta E_{con} \quad (24)$$

Where E_{cell} is the output voltage of the cell, E_{OCV} is the fuel cell open circuit voltage, ΔE_{act} is the voltage loss due to the activation of the anode and the cathode, ΔE_{ohm} is the voltage loss associated with the ohmic resistances at a given voltage and ΔE_{con} is the voltage drop due to the decreasing concentration of oxygen and hydrogen.

MEAs were constructed for this work to evaluate the cell performances and obtain polarization curves of the synthesized catalysts in actual fuel cell conditions. Upon obtaining these curves, activation losses, ohmic losses and concentration losses could be considered and analyzed. Specific MEA manufacturing methods are discussed within the following sections.

Section 3: Ethylenediamine – KJ600 Catalyst

3.1 Introduction

For this study iron(II) sulphate heptahydrate and cobalt dinitrate hexahydrate were used as the metal precursors. EDA and either KJ300 or KJ600 were utilized as the nitrogen and carbon precursors respectively. The metal and nitrogen precursor were coated onto both carbon supports and then heat-treated at 900^{o}C to create two different catalyst samples, denoted as FeCo-EDA-KJ300 and FeCo-EDA-KJ600. A procedural change was added to allow the mixing of the catalyst precursors to happen under reflux conditions for an hour which was not originally done with the two catalyst samples. These new samples are denoted as FeCo-EDA-KJ300R and FeCo-EDA-KJ600R, with the R to denote the reflux procedural change which was performed on the catalyst. The initial carbon precursors as well as the resulting catalysts synthesized were characterized by various analysis methods including SEM, XRD and XPS. The final catalyst samples were then tested electrochemically using a RRDE for the ORR in a half-cell setup and the best performing catalyst sample was used for the synthesis of an MEA for a prototype fuel cell and tested. The work described in this section has been published [55].

3.2 Purpose and Motivation

The work described here was heavily inspired by a recent journal article published by Dodelet's group [15]. The paper describes the interesting correlation between the microporosity of the microporous carbon supports and the resulting active site density in the final catalyst. It was hypothesized by their group that the formation of active sites on the carbon surface could be assisted by these micropores within the carbon structure and hence a highly microporous carbon could obtain a much higher active site density on the surface of the carbon than a carbon support without these micropores. These claims are supported by other reports [109].

The study at hand, utilizes two different porous carbons as carbon supports for the synthesis of a novel NPMCs. These two carbons, KJ300 and KJ600 vary in microporous surface area as well as the size of the micropores – KJ600 having the higher pore surface area and smaller pore

diameter. The study aims to characterize these two carbon supports and to determine the effect of using each for NPMCs.

As for nitrogen precursors, there have been many published journal reports documenting the performance of EDA as a nitrogen precursor for NPMCs [52-57]. This may be due to the fact that EDA acts as a high nitrogen content precursor with a carbon to nitrogen ratio of 1:1, although this may be irrelevant as several other high nitrogen content precursors fail to show similar high performance. EDA is also favoured because of its availability and relatively low cost. The popularity of EDA as a nitrogen precursor for these types of catalysts allows for easy comparisons with recorded data and documented well developed synthesis procedures for these types of catalysts. It was determined that EDA was an ideal precursor for an initial experiment so that all acquired performances could be benchmarked against previous studies. EDA was deemed simple enough such that the effect of the carbon substrate could be gauged and judged independently to the nitrogen source.

The metal precursors chosen for this synthesis were iron(II) sulphate heptahydrate and cobalt(II) nitrate hexahydrate. These materials were left unchanged for the duration of this study as to not introduce any new parameters.

In addition to this straightforward comparison, the procedure was modified between the two different catalyst samples. In one batch of catalysts (FeCo-EDA-KJ600 and FeCo-EDA-KJ300), the mixing solution was refluxed for one hour to allow for a more complete coating of the iron and EDA on the carbon supports. These catalyst samples (FeCo-EDA-KJ600R and FeCo-EDA-KJ300R) were synthesized to evaluate the coating procedure used to try to optimize the performance for the ORR.

3.3 Experimental

3.3.1 Functionalization of Carbon Blacks

Two types of carbon black, KJ300 and KJ600, were treated in concentrated 6 M HCl solution to remove metal impurities present on the carbon. This was followed by thoroughly washing the carbon black with copious amounts of de-ionized water before filtering and drying the carbon

black overnight in an oven at 60°C. The remaining solid was subject to reflux in 70% HNO_3 solution at 80°C for 8 hours to functionalize the carbon. The carbon blacks were then washed again with de-ionized water, filtered and dried overnight in an oven at 60°C.

3.3.2 Catalyst Synthesis

0.25 g of $Co(NO_3)_2 \cdot 6H_2O$ and 0.25 g of $FeSO_4 \cdot 7H_2O$ were dissolved in 125 mL of ethanol before adding 2 mL of EDA. This solution was stirred for half an hour before a solution containing 0.5 g of functionalized carbon black and 125 mL of ethanol was added. The solution was mixed for 30 minutes and then boiled for an hour under ambient pressure with and without reflux. This boiling procedure was done under air at approximately 80˚C to allow the EDA and metal precursor to completely cover the carbon surface. If reflux was used, it was removed after an hour to allow the ethanol to evaporate completely. The dried precipitate was ground using a mortar and pestle and heat-treated at 900^{o}C for an hour, after raising the temperature at 20^{o}C/min from room temperature. The sample was protected with a constant flow of inert nitrogen gas during the entire pyrolysis and cooling stages. The sample was then acid treated in 0.5 M H_2SO_4 for 8 hours before it was filtered and washed with 1 L of de-ionized water. All samples were oven dried overnight at 80˚C before use. Figure 10 shows a schematic representation of the hypothesized process of the procedure.

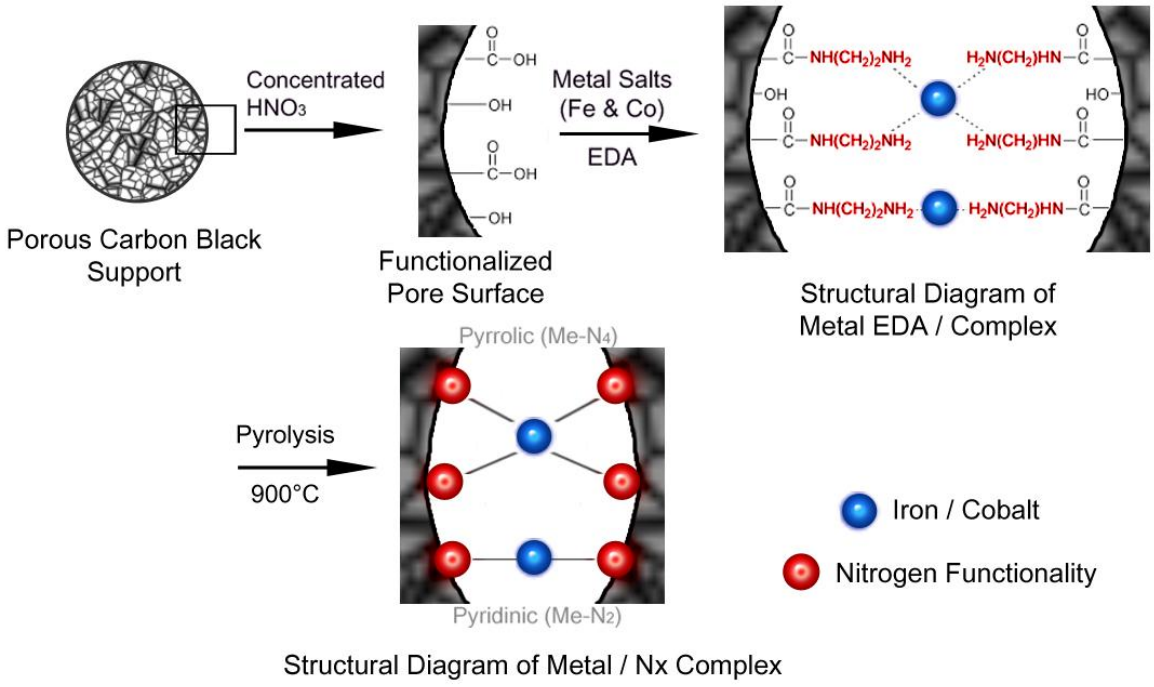

Figure 10: Schematic representation for preparation of the FeCo-EDA-C catalyst. Reproduced with permissions from [55]. Copyright © 2010 American Chemistry Society

3.3.3 Physical Characterization

XRD data was obtained by using Inel XRG 3000 with Cu-Kα radiation to determine elemental composition of the catalysts. EDX and SEM analysis was carried out by using a LEO1530 FE-SEM, equipped with EDAX Pegasus 1200 integrated EDX/OIM. XPS data was obtained using Thermal Scientific K-Alpha XPS spectrometer in order to investigate the relative content of different elements in the catalyst sample.

3.3.4 Electrochemical Characterization

Electrocatalytic activity was evaluated in a three-electrode electrochemical cell using a Pine-Instrument Bipotentiostat AFCBP1 equipped with a speed rotator. The working electrode was a 0.19635 cm^2 glassy carbon surface and a 5.0 mm diameter Pt ring (collection efficiency of 26%). All RRDE measurements were collected in acidic electrolyte; 0.5M H_2SO_4, versus a Ag/AgCl reference electrode at room temperature. The electrode was prepared by dissolving 4 mg of catalyst sample in 2 mL of ethanol. This ink was ultrasonicated for 1 hour 20 µL of the ink was

deposited and allowed to dry on the glassy carbon disc, followed by 10 μL of 0.05 wt% Nafion solution. The catalyst loading on the glassy carbon electrode was 20.4 mg/cm^2. ORR curves were recorded in the potential range of 0 – 1.2 V vs RHE at a scan rate of 10 mV/s with the electrolyte saturated with oxygen gas. ORR curves were corrected for the background current by conducting the same sweep voltammetry in the absence of oxygen and subtracting the curve from the measured ORR curves. Nitrogen was used as the inert gas which was with saturated in the electrolyte. The measurements were repeated at various rotation speeds (100, 400, 900 and 1600 rpm). The ring potential was maintained at 1.2 V vs. RHE throughout the experiments in order to oxidize H_2O_2 produced while oxygen reduction was occurring on the disc electrode.

3.3.5 Membrane Electrode Assembly Preparation and Fuel Cell Polarization Measurements

A commercially available catalyzed gas diffusion electrode (GDE) (LT250EW Low Temperature ELAT® GDE Microporous Layer, E-TEK) was used as the anode for the fuel cell test. Cathode catalyst ink was prepared by thoroughly blending the FeCo-EDA-KJ600R composite catalyst with de-ionized water and recast Nafion ionomer (5% Nafion suspension in alcohols; 1100 Nafion equivalent weight; Solution Technology, Inc.). The catalyst was combined with de-ionized water to achieve a 1:10 ratio by weight. Nafion suspension was added in an amount sufficient to reach a 1:1 volumetric ratio between the ionically-conducting phase (Nafion) and the electronically-conducting phase (catalyst + carbon) in dry cathode catalyst. The mixture was placed in an ice bath to prevent overheating and minimize evaporation of solvents, and then ultrasonically mixed for 100 seconds. A piece of a Nafion 212 membrane was placed on the top of a vacuum table preheated to 80 °C. The vacuum table was used to hold the membrane in place and avoid wrinkling during the catalyst application. Cathode ink was then applied to one side of the membrane using a camel hair brush. Upon completion of the painting, the MEA was left on the heated vacuum table for an additional 30 minutes to allow the cathode catalyst layers to cure. The MEA was then removed from the table and placed in a sealed plastic bag for future use. The cathode catalyst loadings were approximately 4.0 mg/cm^2.

The MEA was assembled in a 5 cm^2 fuel cell prototype. Hydrophobic double-sided and single-sided carbon-cloth gas diffusion layers “backings” from De Nora USA/E-TEK Inc. were used on the cathode and the anode sides of the MEA, respectively. The MEAs were conditioned in

hydrogen-oxygen at 0.40 V and 80 °C. The conditioning was continued until the current density reached a constant level. The flow rates of hydrogen and oxygen were 2 and 5 mL/s, respectively. The anode and cathode gases were humidified at 90 °C and 80°C, respectively. Back pressures of the H_2/O_2 during the polarization were set to 30 psi/30 psi, while no back pressures were set for the durability tests.

3.4 Results and Discussion

XRD patterns for the two carbon black supports and FeCo-EDA complex catalysts based on those supports are shown in Figure 11. All samples showed broad carbon peaks at $2\theta = 24.3°$. Although the XRD result for FeCo-EDA-KJ300R catalyst shows evidence of iron and cobalt oxides, the intensity and variety of the peaks representing transition metals in FeCo-EDA-600R are far more apparent. It was hypothesized that the greater pore volume for the KJ600 catalyst allows for a larger amount of iron constituents to be recognized by XRD. The diffractogram obtained for FeCo-EDA-KJ600R shows distinct iron and iron oxide peaks at $2\theta = 44.7°$, 51.9°, 76.4° and 82.3° and cobalt oxide peaks at $2\theta = 32.4°$, 48.3°, 64.5° and 73.1°. These peaks verify the presence of iron and cobalt crystalline phases.

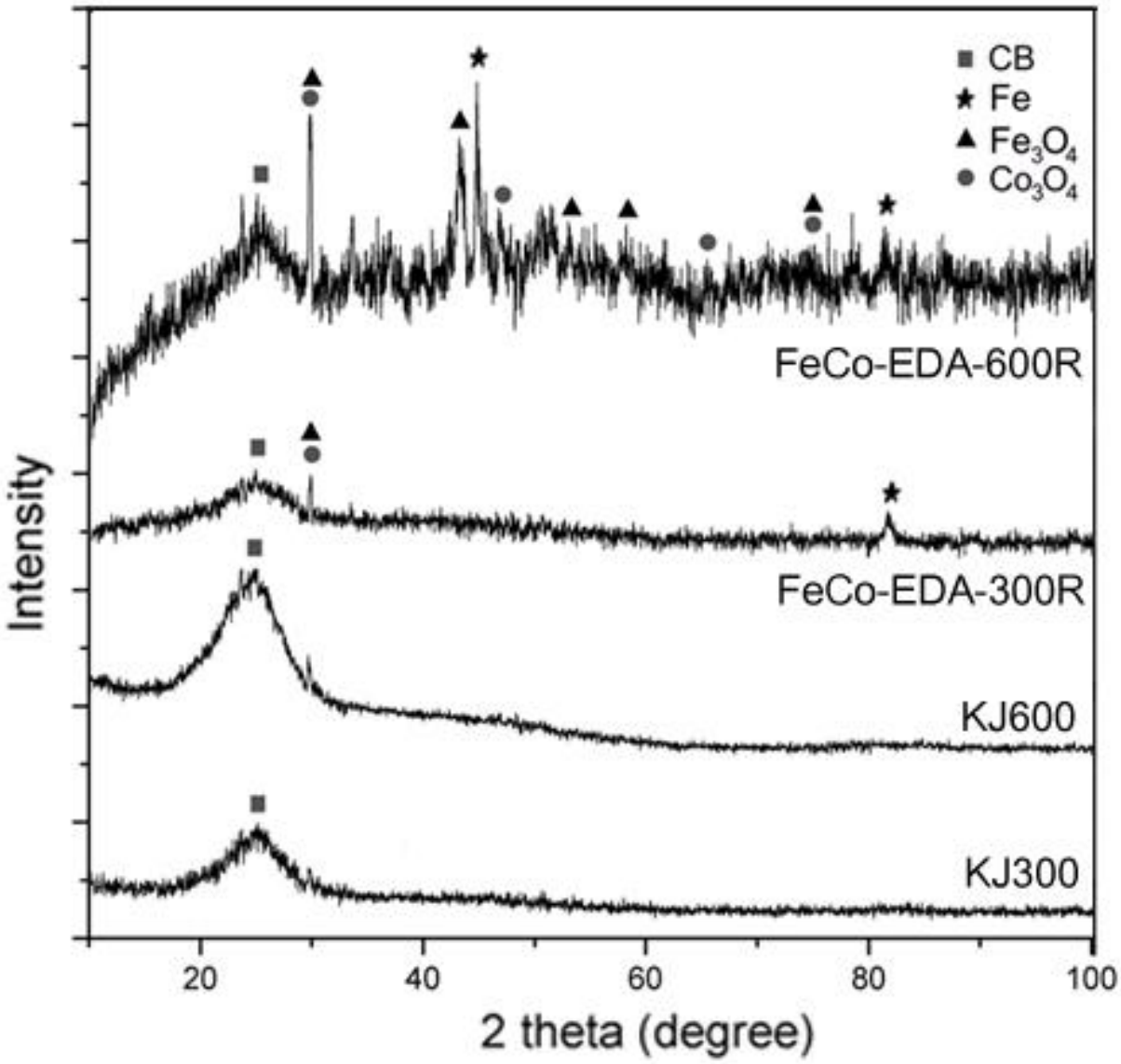

Figure 11: XRD patterns for functionalized KJ300, KJ600, FeCo-EDA-KJ300R and FeCo-EDA-KJ600R. Reproduced with permissions from [55]. Copyright © 2010 American Chemistry Society

Table 2 summarizes the EDX analysis for the elemental weight compositions of the FeCo-EDA-KJ600R catalyst and the FeCo-EDA-KJ300R catalyst. The metal loading on the two samples is quite different as there is about four times the metal loading in the FeCo-EDA-KJ600R. The nominal iron and cobalt loading is 2 wt% for both. This loading is lower in the FeCo-EDA-KJ300R catalyst but two times higher in the FeCo-EDA-KJ600R. This excess is due to EDA not being completely adsorbed onto the carbon surface, much of the EDA is washed and filtered

away if not burned off during pyrolysis. Nitrogen is also a significant component within the catalyst sample but EDX analysis is not ideal for detecting nitrogen content.

Table 2: EDX elemental analysis of FeCo-EDA-300R and FeCo-EDA-600R samples

Composition	FeCo-EDA-300R (wt %)	FeCo-EDA-600R (wt %)
Carbon	90.57	83.06
Oxygen	4.73	4.72
Iron	1.43	4.14
Cobalt	1.04	4.31

The electrocatalytic activity of the four catalysts was evaluated using rotating RRDE voltammetry, shown in Figure 12. The onset potential was measured by taking the potential at which the ORR curves deviated from 0 current from ORR curves corrected for background. This correction was made by obtaining ORR curves at 100, 400, 900 and 1600 rpm in oxygen saturated conditions and subtracting the background current, which was obtained by conducting the voltammetry under nitrogen saturated electrolyte conditions. Similarly, the half-wave potential was measured by finding the potential which was halfway between the limiting current (measured at 0.2 V vs. RHE) and zero current on the ORR voltammetry curve. The FeCo-EDA-KJ600R shows the best performance, followed by FeCo-EDA-KJ300R, FeCo-EDA-KJ600, and FeCo-EDA-KJ300. From ORR curves, the effect of the refluxing process on the electrocatalytic activity is very clear. Refluxing contributed to the half-wave and onset potential being about 0.25 and 0.15 V higher, respectively. This phenomenon is due to the FeCo-EDA complex being fully coated onto the carbon surface, and is deposited in the microporous structure in the carbon support. The KJ600 carbon derived samples showed improved performance over the KJ300 samples whether or not the catalyst was refluxed. Improved current densities, onset and half-wave potentials were shown. This result was due to the increased mesoporous and microporous structure within the KJ600 carbon.

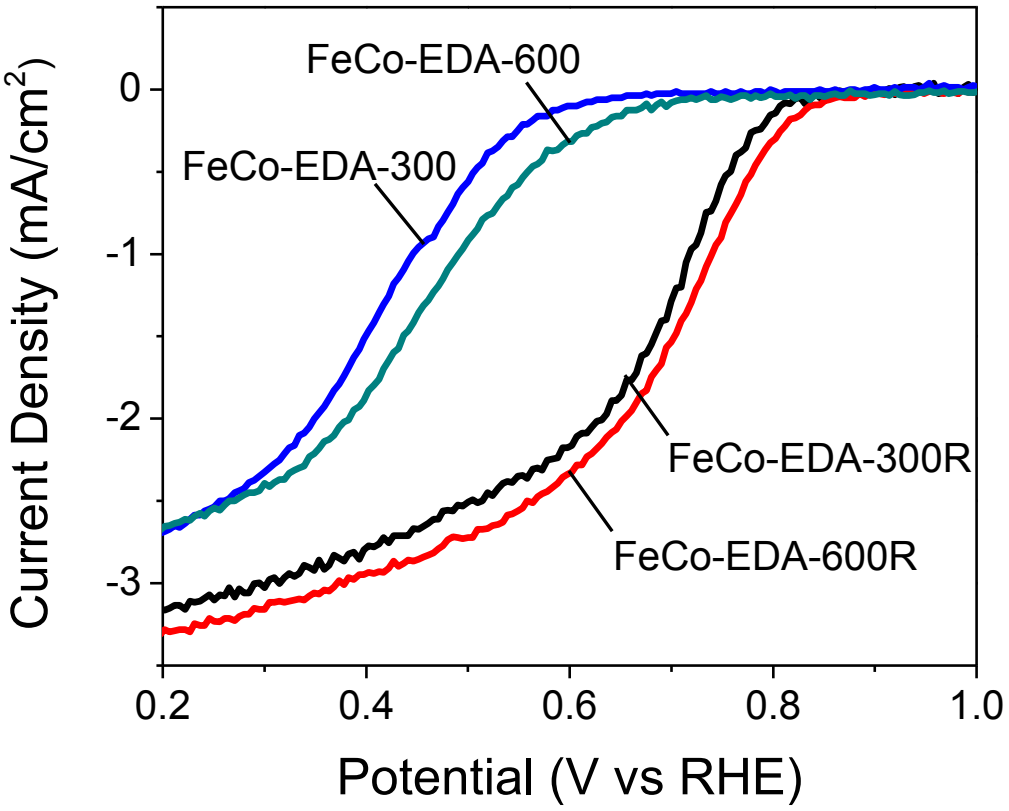

Figure 12: ORR curves of various catalysts; FeCo-EDA-KJ300, FeCo-EDA-KJ600, FeCo-EDA-KJ300R and FeCo-EDA-KJ600R, obtained at 900 rpm in 0.5M H_2SO_4. Reproduced with permissions from [55]. Copyright © 2010 American Chemistry Society

The RRDE voltammetry curves showing the amount of hydrogen peroxide generated during ORR process of four samples are illustrated in Figure 13. The current density, which is directly related to the amount of hydrogen peroxide, obtained for KJ300 based catalysts are almost twice that of the KJ600 based catalysts. Between the two KJ600 based ones, FeCo-EDA-KJ600R which showed the best oxygen reduction activity and generated the least amount of hydrogen peroxide during the reaction. The figure shows that KJ300 based catalysts have fractional yield ranging from approximately 10 - 20% while the values for KJ600 based catalysts fall in the range of 5 – 10%. FeCo-EDA-KJ600R showed the lowest fractional yield of 5%. These results indicated that the activity and selectivity of NPMCs could be improved by using higher pore volume and surface area carbon as catalyst support.

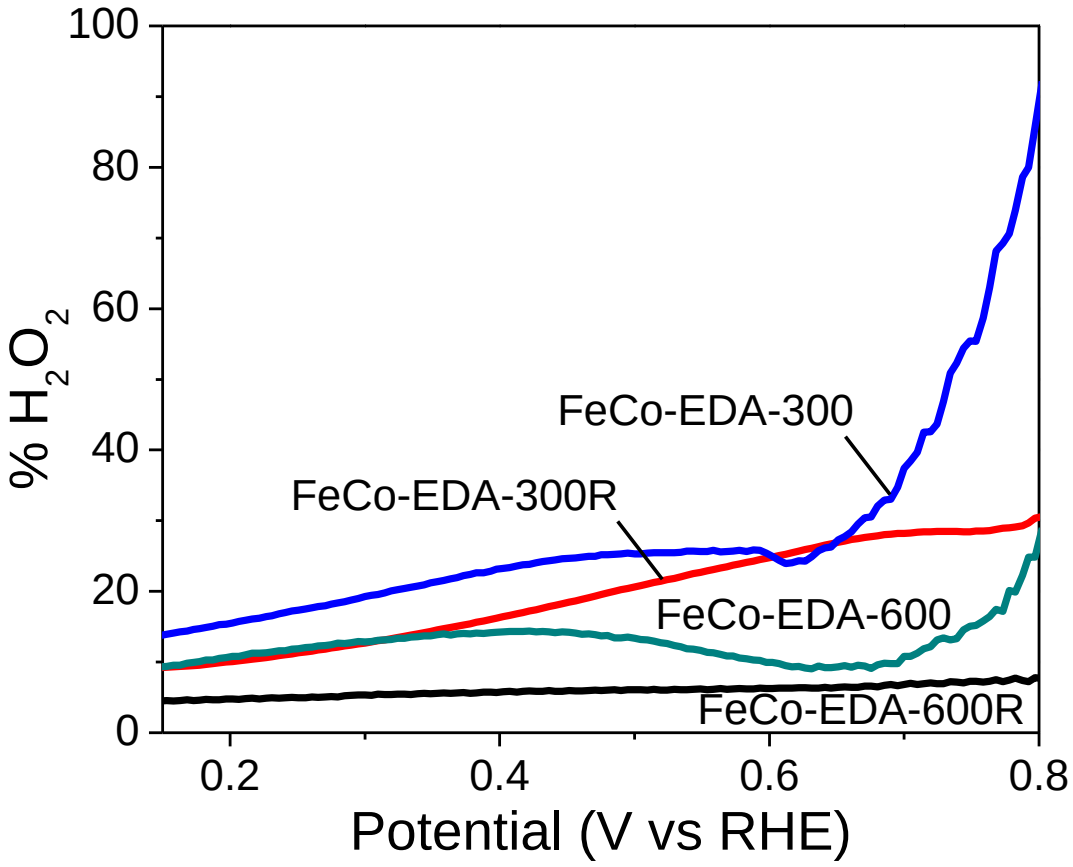

Figure 13: **The fractional yield of hydrogen peroxide for four samples; FeCo-EDA-KJ300, FeCo-EDA-KJ600, FeCo-EDA-KJ300R and FeCo-EDA-KJ600R. Reproduced with permissions from [55]. Copyright © 2010 American Chemistry Society**

The elemental composition and different structural groups of nitrogen in FeCo-EDA-KJ300R and FeCo-EDA-KJ600R were obtained using XPS, shown in Figure 14. From XPS results, FeCo-EDA-KJ600R showed higher nitrogen content (2.15 at.%) compared to FeCo-EDA-KJ300R (1.65 at.%). It is expected that the FeCo-EDA-KJ600R catalyst has higher nitrogen content which could lead to better catalytic activity for various fuel cell catalysts. Three distinct peaks are observed, centered at 404.9, 400.7 and 398.3 eV for each catalyst. The peaks at 404.9 and 398.3 eV are known as pyridinic N^{+}-O^{-} and pyridinic nitrogen groups respectively, while there is some uncertainty regarding the peak at 400.7 eV since it is close to both the peak of pyrrolic nitrogen group at 400.5 eV and the peak of quaternary nitrogen group at 401.3 eV. In

this work, the middle peak will be considered as the co-existence of both pyrrolic and quaternary nitrogen groups. The graph clearly shows that for FeCo-EDA catalyst, the amount of nitrogen content (which can be determined by calculating the area under the curves) is directly related to the electrocatalytic performance. Although the contribution to the catalytic activity of the pyridinic N^{+}-O^{-} nitrogen groups seems ambiguous, it is hypothesized that pyrrolic/quaternary and pyridinic peaks lead to formation of complex structures that are better suited as catalysts. Figure 15 shows the high resolution N 1s peak of all four catalysts. It can be observed that the amplitude of the pyridinic peak is rising as the catalyst performance is increased, compared to the other nitrogen peaks. It has been studied that the formation of pyridinic nitrogen groups is observed on the edge of the graphite plane and the lone pair of electrons from pyridinic nitrogen groups has been attributed to be ORR active. The higher exposure of the planar edges of graphite in FeCo-EDA-KJ600R due to the more rugged surface structure is expected to expose more pyridinic nitrogen which enhances ORR activity. For these reasons it is expected that ORR activity of FeCo-EDA-KJ600R be greatest.

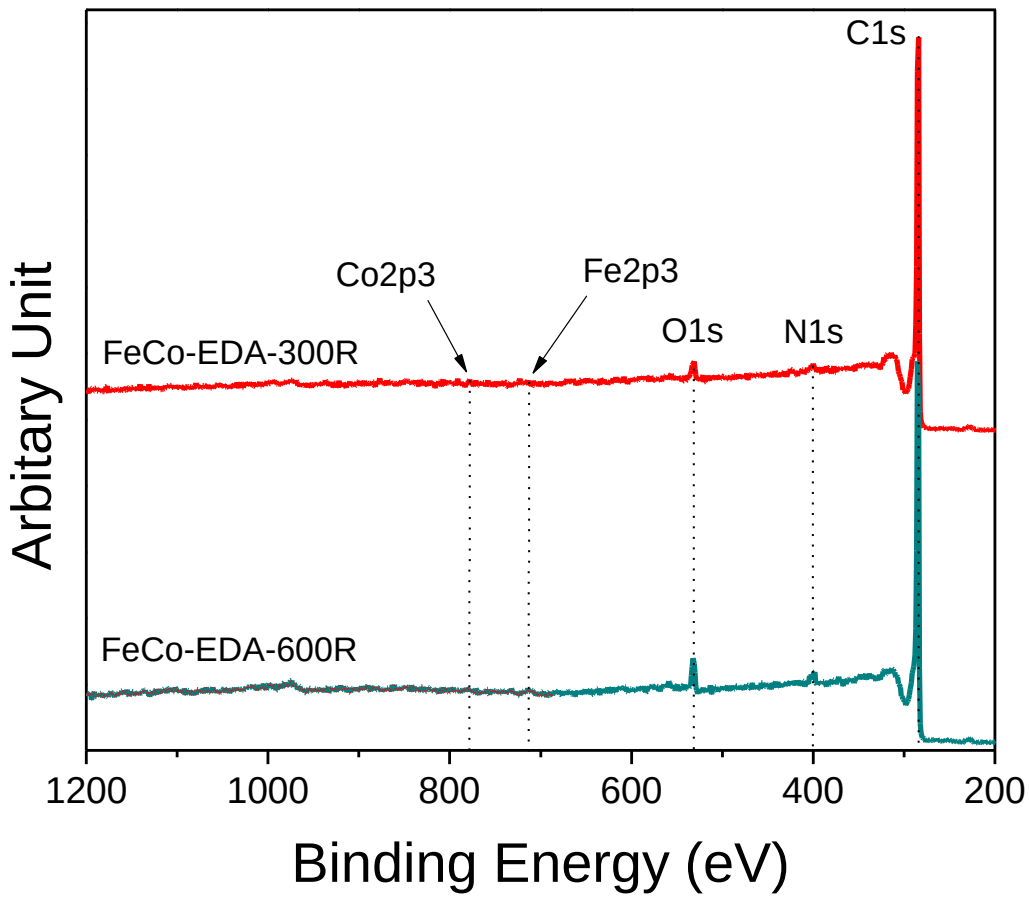

Figure 14: XPS spectrum of FeCo-EDA-KJ300R and FeCo-EDA-KJ600R showing all the elements in the samples. Reproduced with permissions from [55]. Copyright © 2010 American Chemistry Society

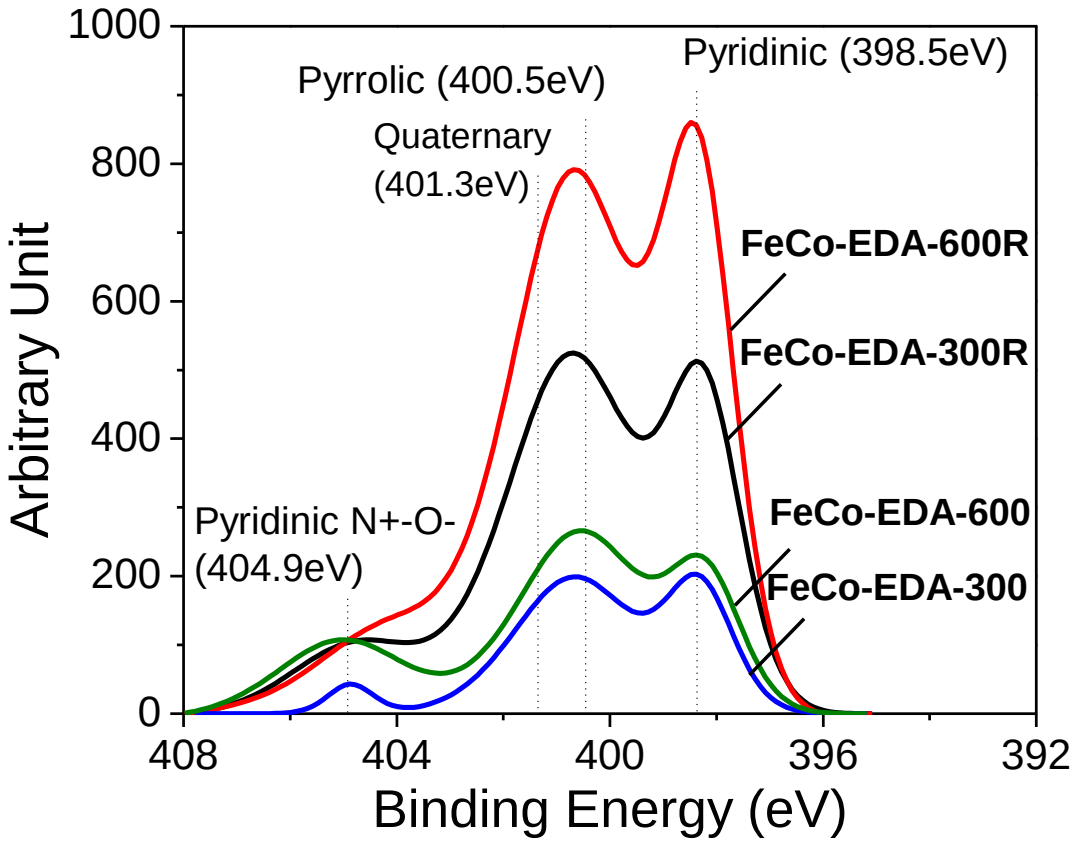

Figure 15: XPS spectrum showing the presence of different types of nitrogen groups from the N 1s signal. Reproduced with permissions from [55]. Copyright © 2010 American Chemistry Society

In order to evaluate ORR catalytic activity of the FeCo-EDA-KJ600R catalyst in practical fuel cell applications, an MEA was fabricated with the FeCo catalyst at the cathode and tested using a fuel cell test station. The PEM fuel cell polarization curve was obtained at 80 ˚C using 30 psi back pressure for both H_2 and O_2. The polarization curves and the corresponding power density curves are shown in Figure 16. At a cell voltage of 0.6 V the current density as measured at 0.37 A/cm^2 with a maximum power density of 0.44 W/cm^2. The stability of the FeCo-EDA-KJ600R catalyst material was tested by holding the cell voltage at 0.4 V at 80 ˚C for 100 hours. No back pressure was applied to the MEA and the cathode catalyst loading was 4.0 mg/cm^2. Figure 17 graphically depicts this current transient for the H_2/O_2 cell with no visible degradation in performance.

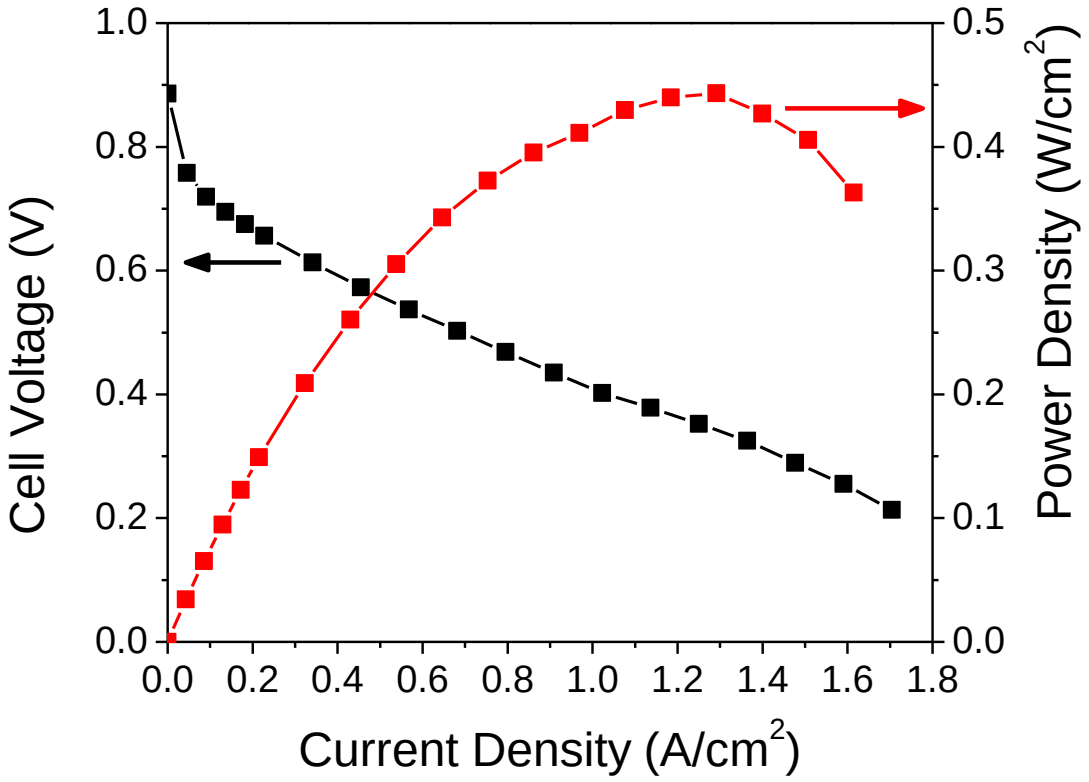

Figure 16: Polarization curve and corresponding power densities of MEAs fabricated with FeCo-EDA-KJ600R cathode catalyst and commercially available catalyzed GDE anode. Cell temperature: 80˚C; Catalyst loading: 4 mg/cm^2; H_2/O_2 back pressures: 30 psi/30 psi. Reproduced with permissions from [55]. Copyright © 2010 American Chemistry Society

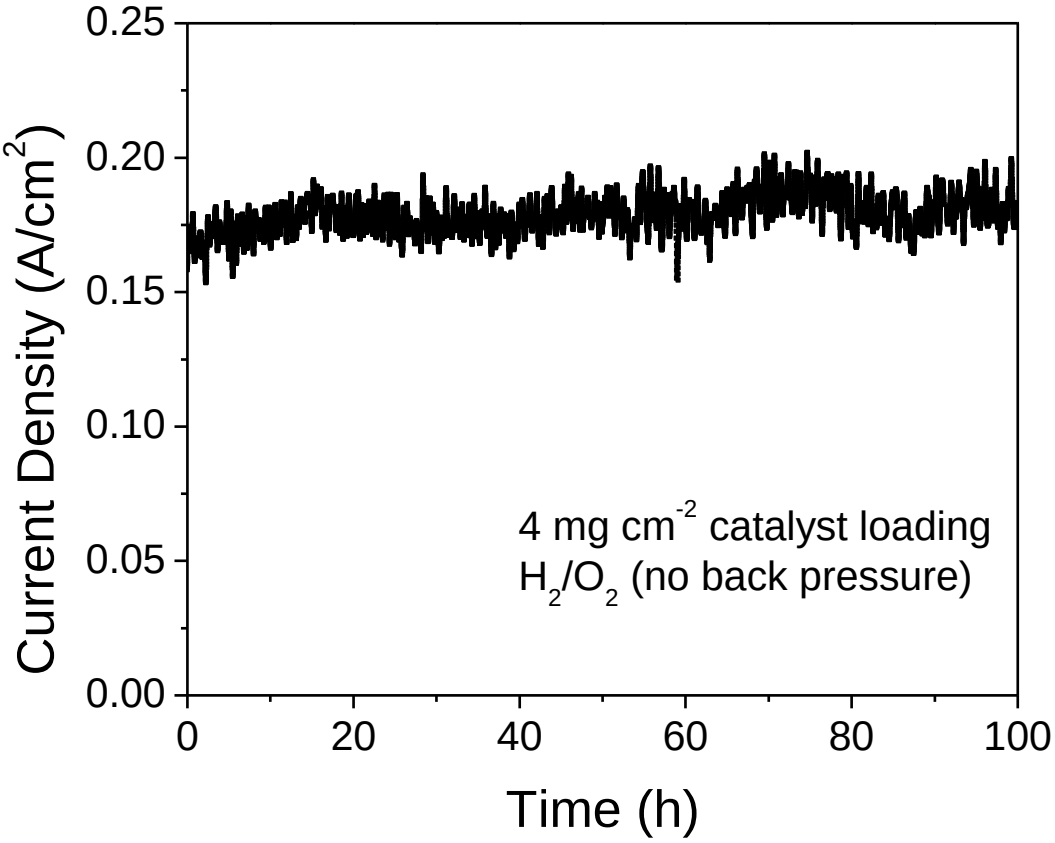

Figure 17: **Durability test of the H_2/O_2 PEM fuel cell at 0.4V for 100 hours. MEA was fabricated with FeCo-EDA-KJ600R catalyst and commercially available catalyzed GDE as the cathode and anode respectively. Cathode catalyst loading: 4 mg/cm^2; Cell temperature: 80˚C; No back pressure. Reproduced with permissions from [55]. Copyright © 2010 American Chemistry Society**

3.5 Conclusions

Non-precious metal catalysts were developed by mixing EDA with iron and cobalt on two different porous carbon black supports in order to improve ORR activity. Among those materials, the FeCo-EDA-KJ600R catalyst possesses the highest electrochemical activity for ORR, as well as the least amount of hydrogen peroxide generated at approximately 5%. Between the two carbon graphite catalyst support, KJ300 and KJ600, KJ600 showed greater potential in generating higher catalytic activity when used as a non-precious metal catalyst due to its higher

pore volume and surface area. During synthesis, KJ600 leads to higher nitrogen content providing more active sites for ORR as confirmed by RRDE and XPS analysis. When NPMC is synthesized using this in-situ method, the addition of a reflux stage increases the resulting catalyst ORR performance. The MEA fabricated with the FeCo-EDA-KJ600R catalyst maintained high power densities. At a cell voltage of 0.3V a current density of 1.4 A/cm^2 was achieved with a maximum power density of 0.44 W/cm^2 using pure O_2. Further study will be necessary to determine the durability of the MEA in fuel cell operating conditions. However, it can be concluded that higher pore volume and surface area of carbon support could lead to higher nitrogen content providing more active sites for ORR and this type of catalyst has great potential used as a non-precious PEM fuel cell catalyst.

Section 4: Cyanamide – KJ600 Catalyst

4.1 Introduction

During this phase of work, iron(II) sulphate heptahydrate, cyanamide and KJ600 were utilized as the metal, nitrogen and carbon precursors respectively. Iron(II) sulphate heptahydrate and cyanamide were first mixed together in ethanol where KJ600 was added before boiling with reflux for 3 hours. The dried precipitate was heat-treated at 1000^{o}C in N_2 to produce the catalyst denoted as Fe-Cyan-KJ600-1. The procedure was only slightly modified to use an additional gaseous nitrogen precursor by pyrolyzing the sample with ammonia gas instead of just pure N_2. This second sample with ammonia gas was denoted as Fe-Cyan-KJ600-2. Two more samples were synthesized from the Fe-Cyan-KJ600-2 catalyst by not ball-milling and ball-milling the sample before undergoing a second coating and pyrolysis with ammonia gas treatment to determine the effects of an additional coating step and pyrolysis to the procedure. The second heat-treated samples were denoted as Fe-Cyan-KJ600-3 and Fe-Cyan-KJ600-4 for the ball-milled and not ball-milled samples respectively. These samples were physically characterized with XPS, XRD, SEM, and NAA. The samples were electrochemically characterized with an RRDE setup in a half-cell for the ORR.

4.2 Purpose and Motivation

From the results seen in section 3, KJ600 showed better performance as a result of the increased surface area caused by the large amount of mesopores as confirmed by NAA. From that conclusion, KJ600 was utilized again in the current study as a high surface area carbon which had the additional benefit of mesoporous to help facilitate active site growth.

Cyanamide was chosen as a new nitrogen precursor which was hypothesized to demonstrate good ORR activity as a NPMC precursor. Unlike EDA, the use of cyanamide was uncommon and had only been reported on by the Los Alamos group as a nitrogen precursor for NPMC PEFC applications [90, 91]. They speculated that cyanamide provides a substantial amount of pyridinic functionalities on the carbon support surface after pyrolysis at high temperatures.

Cobalt(II) nitrate hexahydrate was eliminated as a metal precursor for this catalyst because it was thought to be hindering the initial ORR performance achieved by the final catalyst. Removing cobalt(II) nitrate hexahydrate as a precursor from the catalyst also removed the ambiguity of the active site structure and elemental analysis used to characterize the final catalyst samples. Instead, iron(II) sulphate heptahydrate was used as the sole metal precursor. It has been reported by many journals that iron heat-treated NPMCs demonstrate the highest ORR activity compared to other transition metals such as Cu, Zn, Mn or Co [5].

The purpose of this work was to utilize cyanamide as a nitrogen precursor and to try alternative synthesis procedures to increase the performance for the ORR as high as possible. Hence several variations on the original procedure were tested, including using ammonia as a secondary nitrogen source, re-coating and pyrolyzing the original catalyst and ball-milling and not ball-milling prior to re-coating. The work reported in this section is partially reported previously in ESC Transactions by Hsu and Chen [110].

4.3 Experimental

4.3.1 Synthesis of Fe-Cyanamide-KJ600 Electrocatalyst

Functionalization of carbon black was carried out as described in the previous section. For a typical synthesis of the Fe-cyan-KJ600 catalyst, 0.5 g of functionalized KJ600 was dissolved in 125 mL of denatured ethanol and sonicated for 30 minutes. 0.5 g of $FeSO_4 \cdot 7H_2O$ was completely dissolved in 125 mL of denatured ethanol and mechanically stirred for 1 hour. 2 g of cyanamide was dissolved into 2 mL of denatured ethanol and added to the $FeSO_4 \cdot 7H_2O$ mixture under mixing conditions. This solution was kept stirring for 30 minutes before adding the mixture of carbon black together with the iron-cyanamide mixture. Using an oil bath and condenser tube, the solution was refluxed at 80^oC for 3 hours before the condenser tube was removed and the ethanol was allowed to evaporate from the beaker. The solid precipitate was allowed to dry in an oven at 60^oC overnight. The precipitated solid was collected and heat-treated in a chemical vapour deposition furnace at 1000^oC for 1 hour using NH_3 and/or N_2 as carrier gases. Finally, an acid leaching treatment was carried out using boiling 0.5 M H_2SO_4 with reflux for 8 hours to remove any surface metals.

Two samples underwent a re-pyrolysis to examine the effect of another pyrolysis stage on the performance of the Fe-cyanamide-KJ600 sample. To go about the re-pyrolysis, the samples that had undergone a first pyrolysis were taken after acid leeching sample. One was ball milled for 3 hours while the other sample did not receive ball-mill treatment. The resulting samples were then re-coated with $FeSO_4 \cdot 7H_2O$ and cyanamide as described previously at half loading, for example, 0.5 g of ball-milled catalyst sample was mixed with 0.25 g of $FeSO_4 \cdot 7H_2O$ and 1 g of cyanamide using the same procedure for the first pyrolysis.

4.3.2 Physical Characterization

All samples were analyzed by XRD, SEM, XPS, and NAA. XRD analysis was done with an Inel XRG 3000 diffractometer using a Cu-Kα source. A broad range scan of the 2θ range from 0.288^o to 113^o was captured for about 10 minutes per sample. A LEO FESEM 1530 was used to take SEM images at 100 kx magnification at 20 kV. XPS was carried out using a Thermal Scientific K-Alpha XPS spectrometer at 150 eV to investigate the relative content of different elements and the relative content of different types of nitrogen bondings. BET surface areas and pore size distributions were obtained through N_2 adsorption/desorption isotherms using an Autosorb 1 from Quantachrome. Prior to N_2 adsorption/desorption, samples were subject to an outgassing pretreatment by heating the sample at 100^oC in a vacuum overnight.

4.3.3 Rotating Ring Disc Electrode Experiments

Electrochemical activity was measured through the use of rotating ring disc electrode experiments in a three-electrode half-cell setup. A platinum wire was used as the counter electrode and a Ag/AgCl electrode was utilized as reference. All potentials were converted to the RHE scale. Catalyst inks were made using denatured ethanol at concentrations of 2 mg/mL and sonicated until the catalyst was uniformly dispersed in the ink. The ink was deposited in 5 μL increments on a 0.19635 cm^2 glassy carbon disc electrode until the surface of the electrode was fully coated with the electrocatalyst. 10 μL of *ca.* 0.05 wt% of Nafion in ethanol was added on top of the electrocatalyst as a binding agent. Disc and ring electrochemical measurements were obtained using a PINE AFCBP1 bipotentiostat in the range of 0.05-1.0 V vs. RHE at 10 mV/s in 0.1 M $HClO_4$ while saturating the electrolyte with oxygen. The background current was removed by performing cyclic voltammetry experiments with the same conditions while bubbling N_2 gas in the electrolyte. Collection efficiency and diameter of the ring was 26% and 0.6 mm.

4.4 Results and Discussion

SEM analysis was carried out at various stages within the synthesis procedure and is shown in Figure 18. The micrographs show significant morphological changes of the catalyst at 100k times magnification. Figure 18a is an SEM image of functionalized KJ600 prior to use in the catalyst synthesis. Particles show uniform size distribution and no agglomeration. Although the pore channels cannot be seen from the micrograph, KJ600 is a high surface area carbon with significant pore volume - as later confirmed by nitrogen adsorption/desorption analysis. Figure 18b shows the KJ600 after the surface and pores have been coated with cyanamide and the iron precursor. This coating on the functionalized KJ600 can be observed from the SEM image as it is apparent that the average particle diameter has increased. The iron-cyanamide coating also induces agglomeration to occur between the KJ600 particles further decreasing specific surface area and causing blockage of the carbon pores. It can be seen in Figure 18c where catalyst sample (Fe-cyanamide-KJ600-2) has been heat-treated with ammonia and acid leached, that the iron-cyanamide coating seen in Figure 18b has been reduced and the particles are similar in shape and size distribution to the functionalized KJ600. Smaller particles are vital for increased surface area, increased access to pore channels, as well as, increased edge plane exposure of carbon to form higher pyridinic nitrogen within the catalyst. It is hypothesized that after pyrolysis with ammonia, the iron-cyanamide coating is effectively etched away leaving behind these nitrogen functionalities and Fe-N complexes believed to be the active sites. Figure 18d reveals the morphology of the Fe-cyan-KJ600-3 catalyst showing a drastic increase in particle size and severe agglomeration of the carbon black particles.

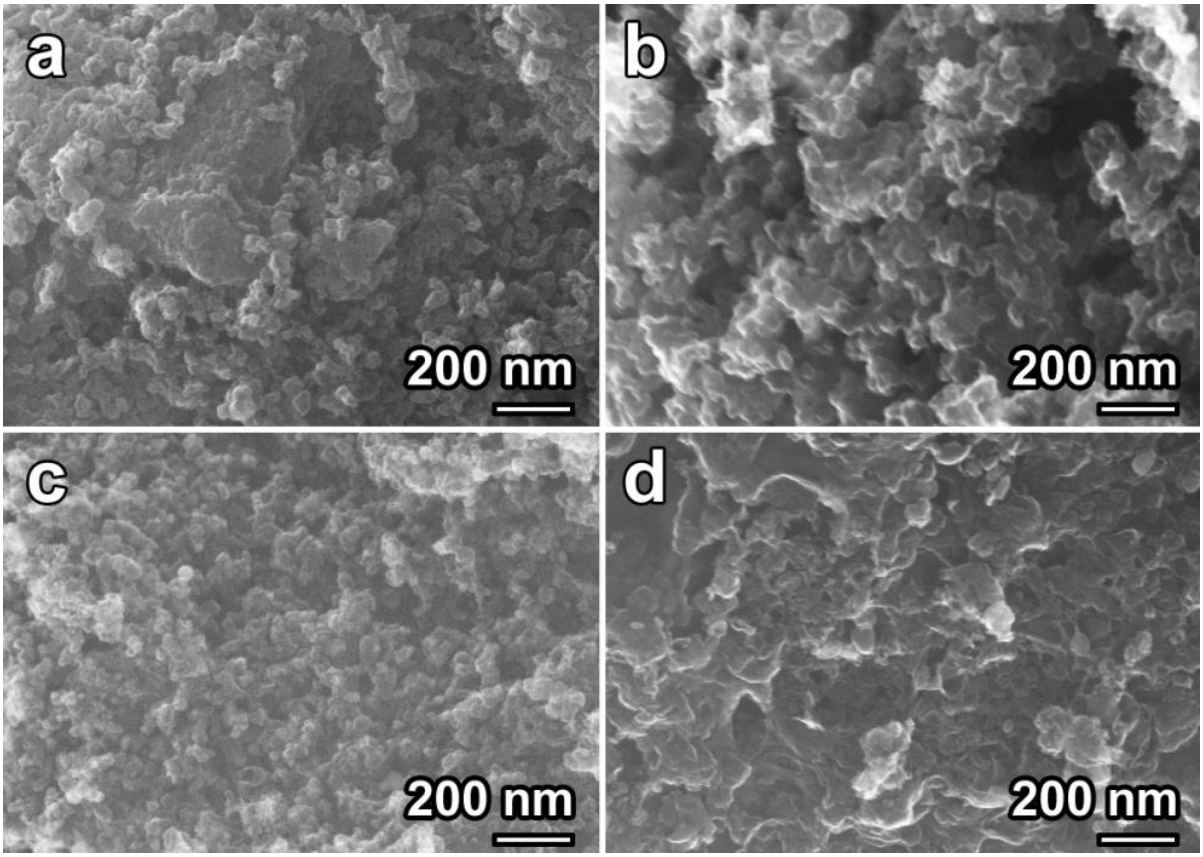

Figure 18: SEM images of a) functionalized KJ600, b) coated KJ600 prior to pyrolysis treatment, c) Fe-cyan-KJ600-2, and d) Fe-cyan-KJ600-3. Images were taken using a LEO FESEM at 100k times magnification at 20keV [110]. Reproduced by permission of The Electrochemical Society

Three samples were synthesized and tested to determine the effect of various preparation treatments: (a) Fe-cyan-KJ600-1 with one pyrolysis using no ammonia during the pyrolysis treatment, (b) Fe-cyan-KJ600-2 with one pyrolysis treatment in ammonia, and (c) Fe-cyan-KJ600-3 with two pyrolysis treatments both with ammonia as an additional nitrogen precursor. XRD analysis, shown in Figure 19, was carried out on all three samples to determine the crystalline phases present. At *ca.* 26^{o} the graphitic C(002) face can be seen in all three catalyst samples. The relative intensity of this peak is seen to be highest in the Fe-cyan-KJ600-2 sample with one pyrolysis treatment with ammonia. This can be attributed to the greater graphitized carbon exposure brought on by the treatment with ammonia. The Fe-cyan-KJ600-3 catalyst sample was also treated with ammonia for both pyrolysis treatments which would expose greater

graphitized carbon from the KJ600 surface, however, the increased loading of cyanamide and iron precursor added during second coating step may not have been effectively etched away during the second pyrolysis. This hypothesis is supported by the SEM images obtained for the Fe-cyan-KJ600-3 catalyst where there is severe agglomeration seen within the particles and increased carbon particle sizes. XRD analysis also revealed iron present in the form of iron crystals (Fe), iron carbide (Fe_7C_3) and iron nitride (Fe_3N and Fe_4N) with respective peaks indicated on the diffractogram in Figure 19. Each catalyst sample was thoroughly treated with sulphuric acid to ensure surface metals on the catalyst were removed, thus, the metal and metallic species remaining are likely to remain on the catalyst as encapsulated particles trapped under carbon layers. This result is widely supported by literature and several groups have even attempted to argue that the encapsulated iron particles facilitate the formation of ORR active sites owing to the change in electron effect near nitrogen functionalities. However, they claimed that the encapsulated iron particles themselves were not the sites for oxygen reduction [29].

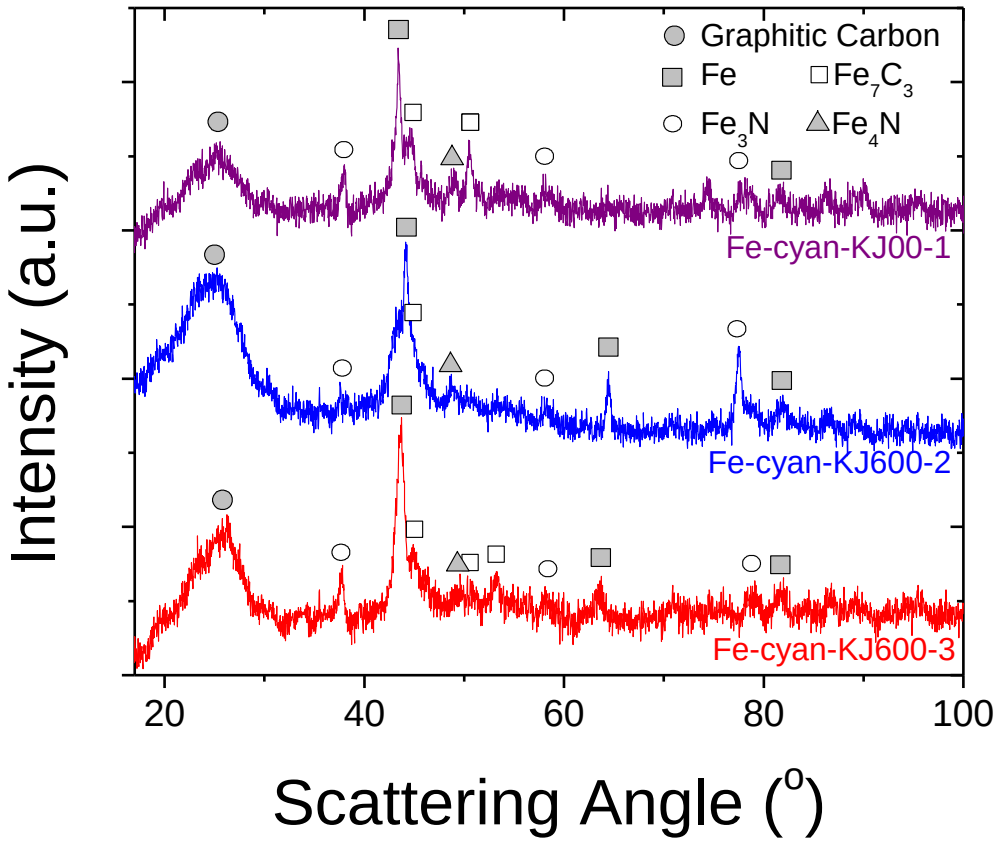

Figure 19: XRD patterns for Fe-cyan-KJ600-1, Fe-cyan-KJ600-2, and Fe-cyan-KJ600-3 [110]. Reproduced by permission of The Electrochemical Society

To investigate the significance of pore volume and surface area on the catalytic activity, nitrogen adsorption and desorption isotherms were measured (Figures 20-24). A summary of the resulting analysis is outlined in Table 3. Each isotherm plot demonstrated characteristics indicative of micro/mesoporous carbons and pore condensation at high relative pressures. As expected, with each sequential coating and pyrolysis step, total pore volume decreases as nitrogen functionalities and carbon coatings have been impregnated into the pores. An increased pore volume was observed for the first pyrolysis using NH_3 gas compared to the first pyrolysis without NH_3. This is believed to be due to the etching and reaction of ammonia with the existing coating prior to pyrolysis. Ammonia gas facilitates the destruction of the coating and utilizes the excess nitrogen to form active site complexes on the surface of the carbon. This result is reflected in the BET surface areas calculated between the first pyrolysis samples with and

without ammonia as a nitrogen precursor. As shown in Table 3, there is a dramatic increase in BET surface area seen in the pyrolysis with ammonia due to the uncovering of blocked pore channels and removal of the coating into a denser active site surface. It is also important to note how this total pore volume and BET surface area change as a second pyrolysis stage is introduced to the procedure. A drastic decrease in BET surface area is observed, even with half loading of the cyanamide and iron precursor coating. This decrease in BET surface area does not correlate with the increase in electrochemical ORR performance as seen later in this report. This discrepancy is surprising and further works need to be carried out to understand the correlation of this result to the effect on catalytic performance.

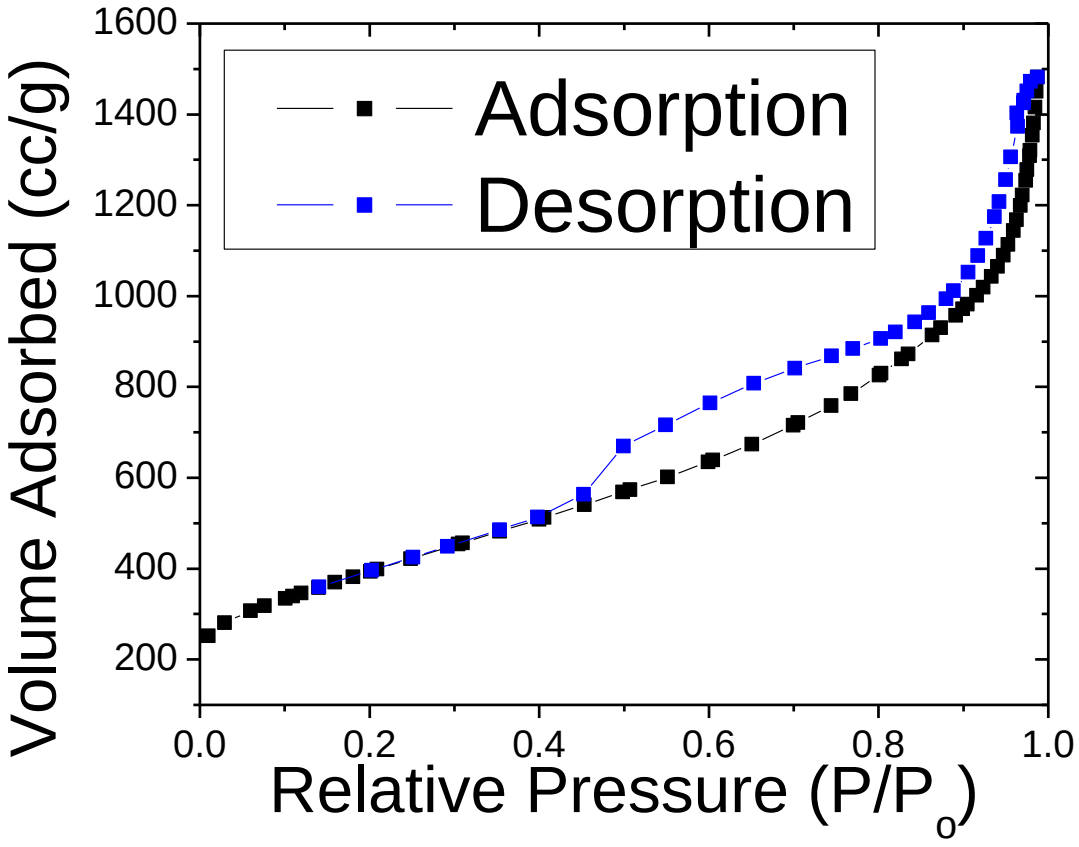

Figure 20: Adsorption and desorption isotherm for BET analysis of functionalized KJ600

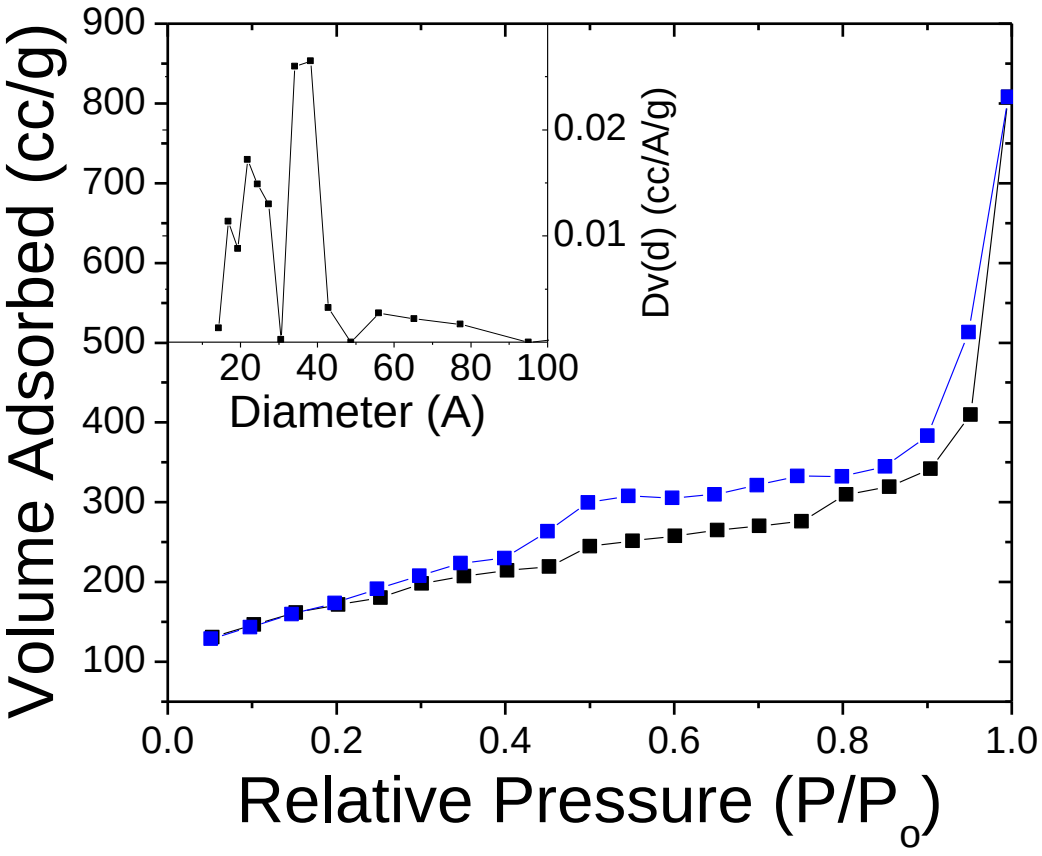

Figure 21: Adsorption and desorption isotherm for BET analysis of Fe-cyan-KJ600-1, no NH_3

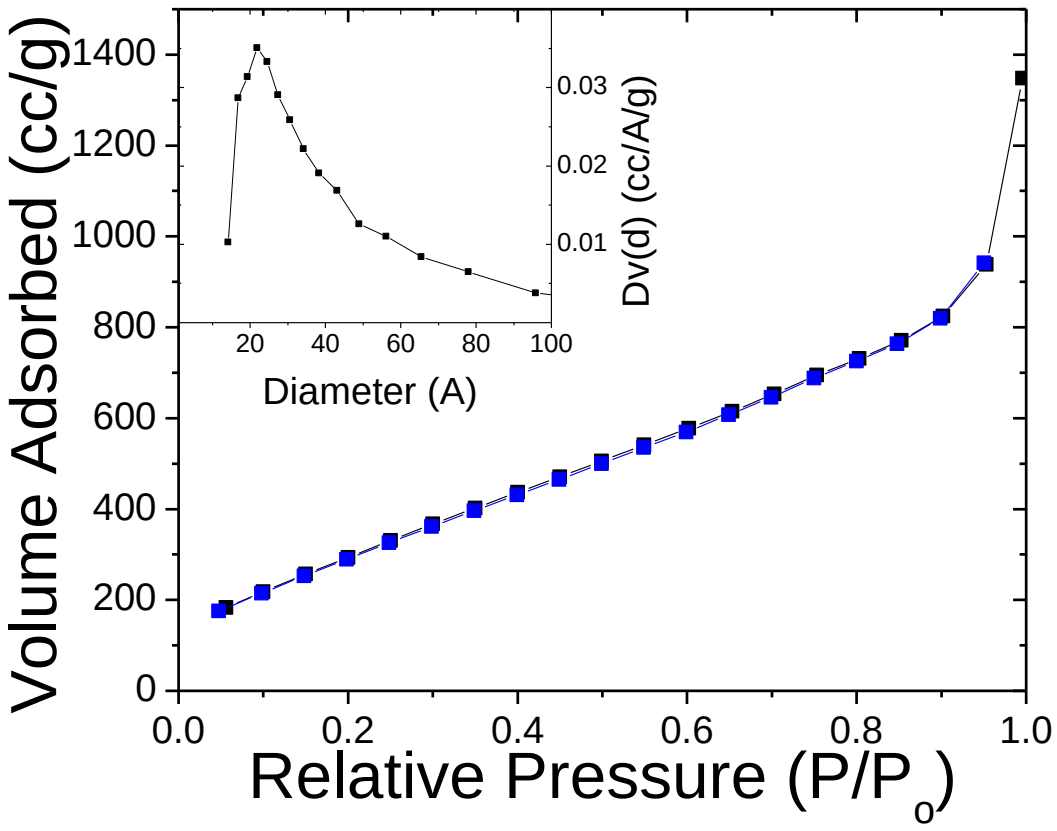

Figure 22: Adsorption and desorption isotherm for BET analysis of Fe-cyan-KJ600-2, with NH_3

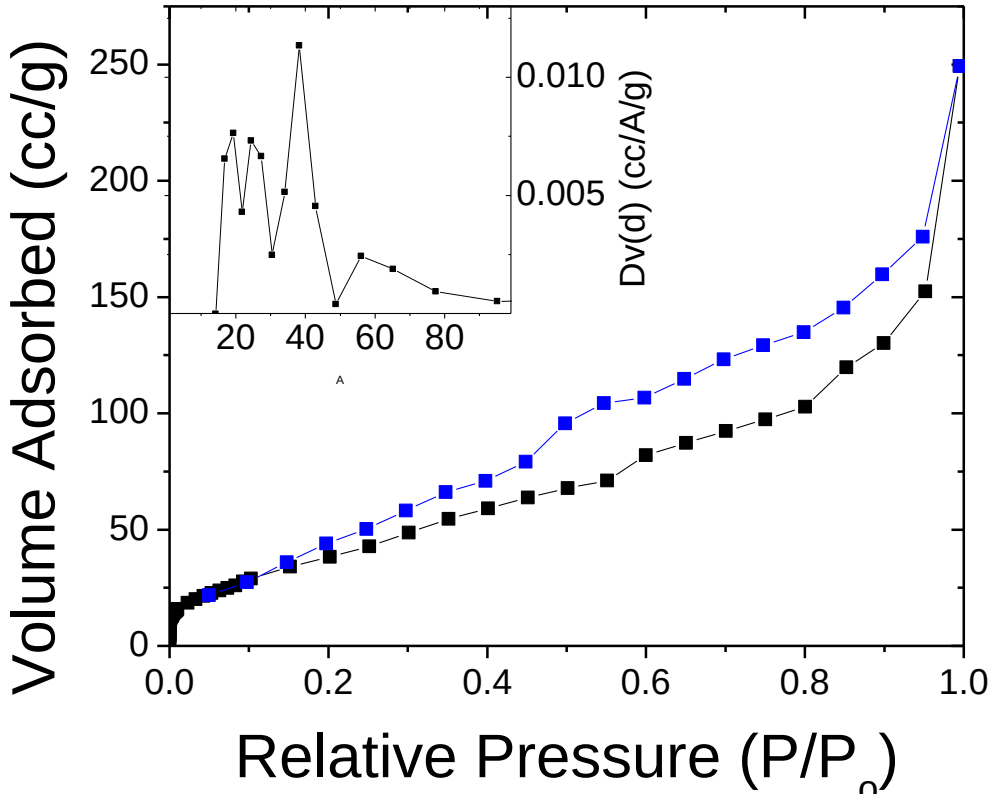

Figure 23: Adsorption and desorption isotherm for BET analysis of Fe-cyan-KJ600-3, 2nd pyrolysis, with NH_3

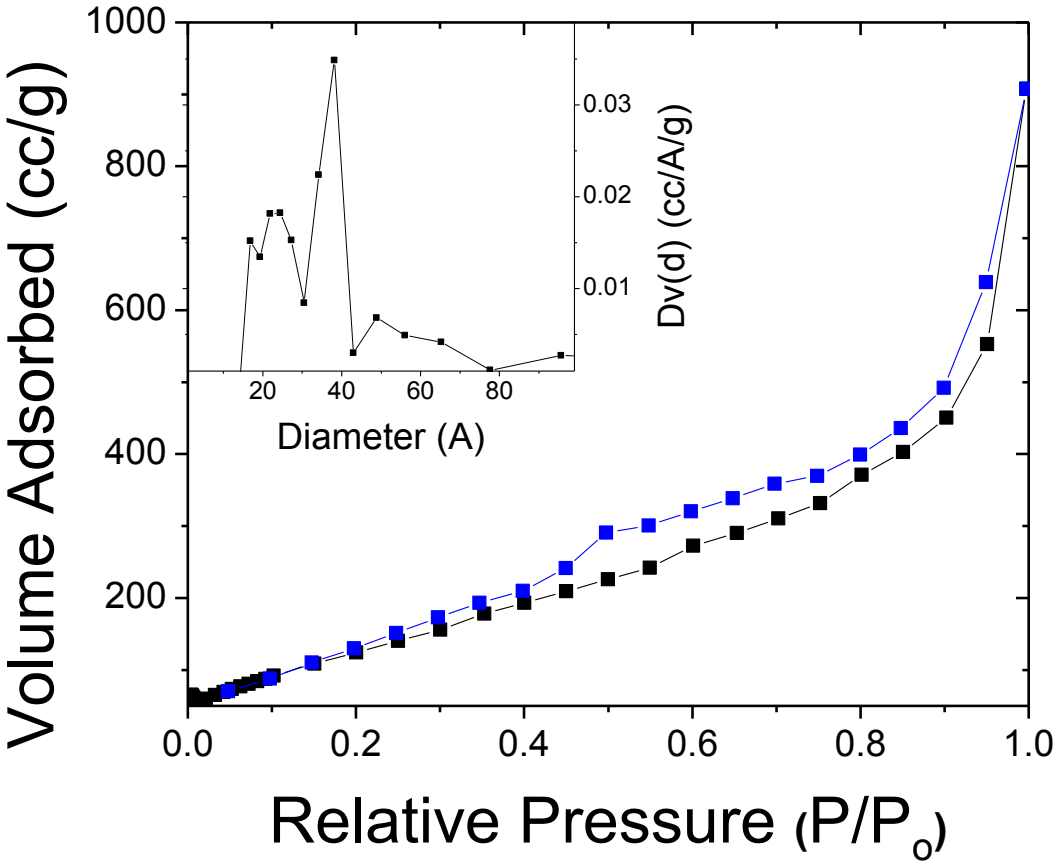

Figure 24: Adsorption and desorption isotherm for BET analysis of Fe-cyan-KJ600-4, 2nd pyrolysis, with NH_3, no ball-mill

Table 3: Summary of N_2 adsorption/desorption analysis

Sample	BET Surface Area (m^2/g)	Average Pore Size (nm)	Total Pore Volume (cm^3/g)
Functionalized KJ600	1416	6.1	2.391
Fe-cyan-KJ600-1	603	3.8	0.8373
Fe-cyan-KJ600-2	1194	2.2	1.603
Fe-cyan-KJ600-3	113	1.1	0.3345
Fe-cyan-KJ600-4	531	0.91	1.147

Figure 25 illustrates the ORR activity of the different catalyst samples as measured by RDE experiments at 1600 rpm. It can be seen that the Fe-cyan-KJ600-1 catalyst without ammonia in the pyrolysis exhibits poor performance by itself as the ORR polarization curve shows a low onset and half-wave potential (0.48 V vs RHE). For non-precious Fe-N/C catalysts it is typical to experience poorly defined plateaus in the mass limiting potential range. This is because of the relative slow kinetics compared to platinum catalysts, and an uneven active site distribution that can be brought on by the porous nature of the carbon.

The Fe-cyan-KJ600-2 catalyst has increased half-wave potential (0.54 V vs RHE), onset potential and limiting current density, even though the increases in onset potential and limiting current density are slight. As hypothesized, the addition of NH_3 as a nitrogen precursor added to the pyrolysis stage significantly improved the observed half-wave potential by 0.06 V. The Fe-cyan-KJ600-3 catalyst utilized a second pyrolysis using ammonia which improved the performance of the Fe-cyan-KJ600 catalyst by an additional 0.11 V vs RHE in half-wave potential. A problem seen with the ORR polarization curve after a second pyrolysis is the dramatic reduction in limiting current density. Several factors were hypothesized to cause this, most significantly, the low BET surface area. The ball-mill procedure was applied to the Fe-cyan-KJ600-3 catalyst which was thought to crush the pores and reduce the surface area of the

carbon black. This was demonstrated by the reduction in BET surface area by NAA. Therefore, a fourth catalyst was made and tested without the use of the ball-mill procedure, Fe-cyan-KJ600-4. This catalyst has significantly higher surface area than Fe-cyan-KJ600-3 (4.7 times higher) and therefore has much better limiting current density comparable to the other two samples that were not ball-milled (Fe-cyan-KJ600-1 and Fe-cyan-KJ600-2). Thus, the Fe-cyan-KJ600-4 sample had a 0.15 V vs RHE improvement in half-wave potential which was due to the etching of the pores using NH_3 and a second pyrolysis treatment which allowed for greater coating and active site formation on the surface of the catalyst. It was interesting to note that ball-milling the sample actually harmed the catalyst in terms of the surface area and the number of active sites that would be able to interact with the electrolyte. It was suggested that the ball-mill would actually crush/shut the pores resulting in no access for those potential active sites to carry out the ORR.

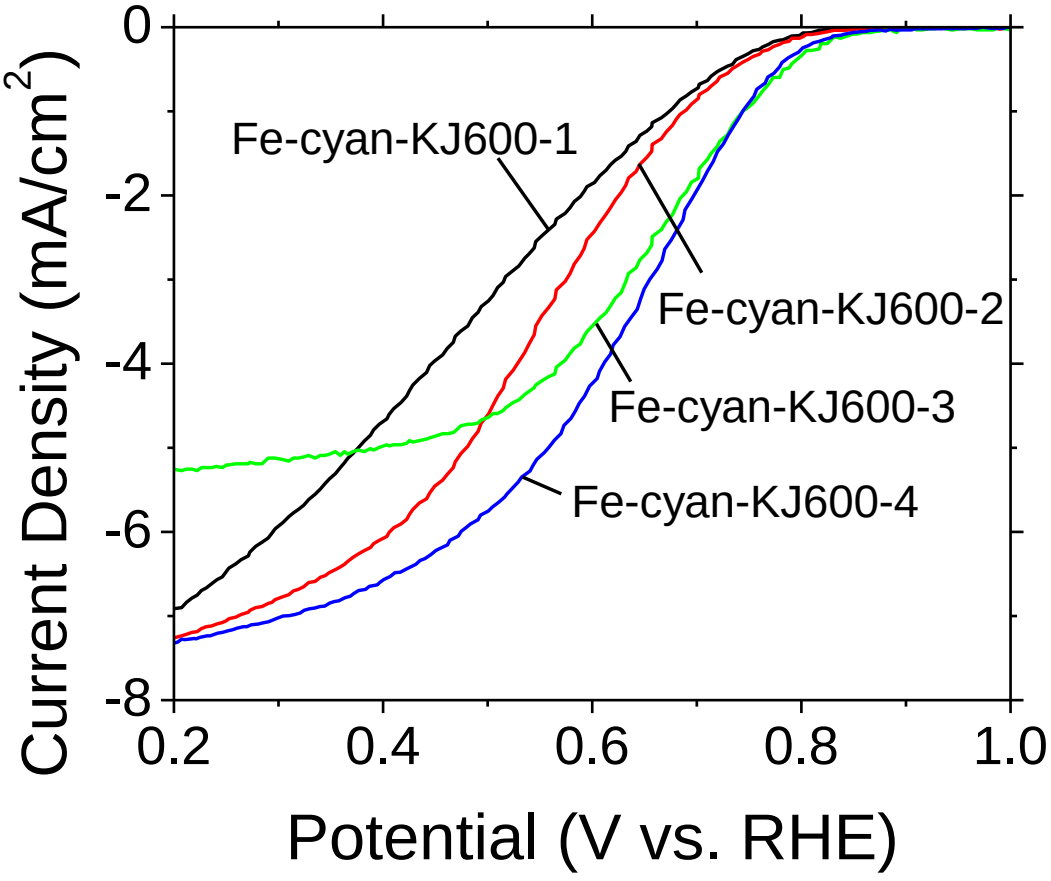

Figure 25: ORR Polarization curves of Fe-cyan-KJ600-1, Fe-cyan-KJ600-2, Fe-cyan-KJ600-3 and Fe-cyan-KJ600-4 catalyst samples at 1600 rpm in 0.1 M $HClO_4$ [110]. Reproduced by permission of The Electrochemical Society

4.5 Conclusions

Cyanamide as a lone nitrogen precursor for these types of catalyst resulted in a poor Fe-cyan-KJ600 electrocatalyst which demonstrated low onset (0.82 V vs. RHE) and half-wave (0.48V vs. RHE) potentials. Regardless of the nitrogen ratio in the organic nitrogen precursor, cyanamide by itself did not outperform other organic nitrogen precursors tested by our group previously. Successful use of ammonia gas as an additional nitrogen precursor to increase the ORR catalytic performance was carried out and resulted in higher onset and half-wave potentials of 0.83 and 0.54 V vs. RHE respectively after a first pyrolysis.

A further enhancement of the ORR performance was seen after a second coating and pyrolysis (with ammonia) treatment was done. It was found that although the second coating and pyrolysis was able to increase the half-wave (0.65 V vs. RHE) and onset (0.94 V vs. RHE) potentials by and increasing the number of active sites, the limiting current density was diminished. This result is possibly due to the reduction of pyridinic nitrogen which is transformed to quaternary type nitrogen on the catalytic surface. BET analysis provided no conclusive evidence that nitrogen functionalities and active sites are hosted within the pores of the carbon support.

Section 5: TCNB/TCNE – KJ600 Catalyst

5.1 Introduction

In this phase of work, tetracyanoethylene and 1,2,4,5- tetracyanobenzene were mixed with iron(II) acetate which all were used as iron phthalocyanine precursors. KJ600 was mixed in with these precursors and were refluxed in quinoline for 24 hours to create the phthalocyanine structure and adsorb it onto the carbon black surface. Heat-treatment of the precipitate was done in several stages and involved (1) a one hour heat treatment at 300^{o}C to remove water and complete the macrocycle complex of any unformed TCNE/TCNB monomeric units, (2) a one hour heat treatment at 400^{o}C to further remove water from the dehydrogenation polymerization reaction of any iron phthalocyanine sheet polymer synthesis, and finally (3) a one hour treatment at a final heat-treatment temperature (600 – 1100^{o}C) to destroy the newly synthesized macrocyclic compounds to form ORR active sites on the carbon surface. Each synthesized catalyst was named according to the format of FeAc-X-Y-Z, where X = TCNB or TCNE, Y denoted the final heat-treatment temperature in the final one hour heat-treatment step described above, and Z was the flow gas being used in the furnace reactor while the pyrolysis took place.

Altogether, 8 different samples were created and characterized physically using XPS, XRD, TGA, FTIR, and TEM, and electrochemically using RRDE analysis and MEA testing.

5.2 Purpose and Motivation

Of the different types of NPMCs, macrocyclic compounds containing the M-N_4 moiety are among the oldest being tested for the ORR. These macrocyclic compounds, or phthalocyanines can polymerize together to form sheets of phthalocyanine monomeric units. The advantage to using these polymer sheets of iron phthalocyanine units is that the iron centres are very small and extremely close together. Upon pyrolysis and desctruction of the sheet polymer, the iron centres and M-N_4 moieties are hypothesized to become active sites for the catalysis of the ORR. Well-developed sheet polymers or linear polymers on the surface of the carbon disperse these iron particles very uniformly on the carbon surface leading to very dense active site formation and hopefully increased ORR activity and performance.

The purpose of this study was to design an NPMC with extremely high active site density. This is to be accomplished by choosing novel iron phthalocyanine precursors and synthesizing these polymer sheets which are to adsorb on the surface of the KJ600 carbon support. Pyrolysis of the resulting carbons would destroy the iron phthalocyanine structure and leave behind evenly distributed and densely packed iron nanoparticles on the carbon surface hopefully creating active sites for the ORR. Figure 26 describes the proposed synthesis reaction steps for the polymer sheets in this work.

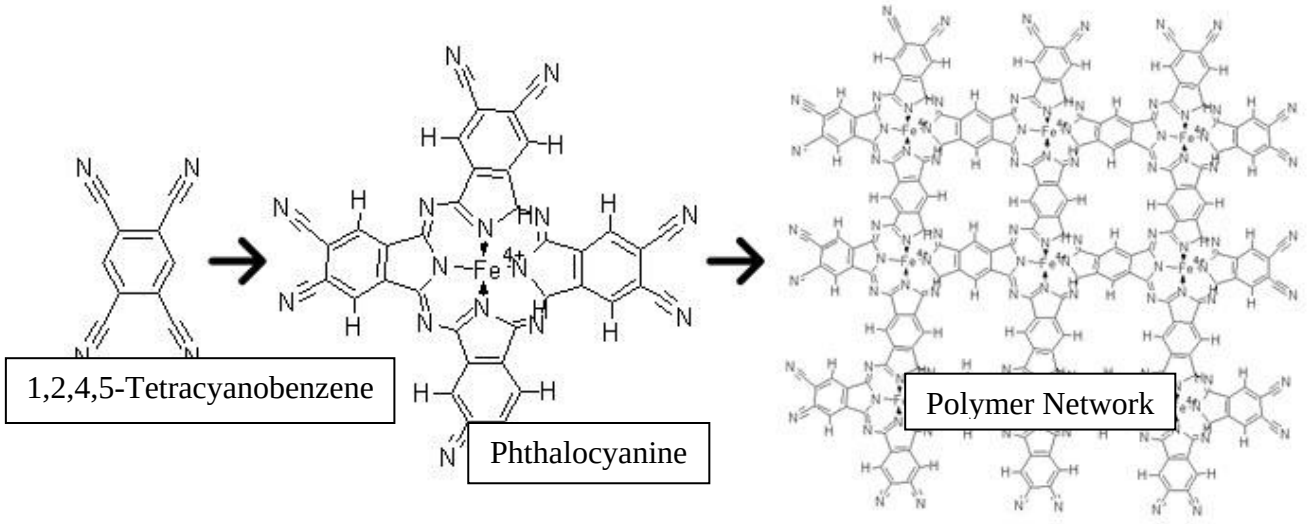

Figure 26: Proposed schematic of iron phthalocyanine polymer network

5.3 Experimental

5.3.1 Catalyst Preparation

0.0178 g of 1,2,4,5-tetracyanobenzene (TCNB) (Sigma Aldrich, 97% pure) and 0.0174 g of iron(II) acetate (Sigma Aldrich, 95% pure) was dissolved and stirred in 10 mL of quinoline for 30 minutes under N_2 protection. This allowed for a 1:1 ratio of iron to TCNB and a 2 times excess of iron for iron phthalocyanine product. KJ600 (AkzoNobel Corporate) was functionalized by the procedure described in [55] and 0.3168 g was added to the mixture and left stirred for another 30 minutes. The temperature of the solution was raised to 210^{o}C and refluxed with nitrogen protection for 24 hours. The catalyst was then precipitated by the addition of 200

mL of methanol and filtered and washed with copious amounts of methanol. No purification methods were used to isolate the polymer sheet. The solid product was dried in an oven at 60^{o}C overnight. The various samples were then ground into a fine powder and heat-treated in a reaction furnace at 300^{o}C for 1 hour, ramped up to 400^{o}C and held for 1 hour and then ramped up to the final heat-treatment temperature and held for 1 hour. The furnace was allowed to cool before the sample was removed and used as the final product.

A similar catalyst was synthesized using tetracyanoethylene (TCNE) as an iron phthalcyanine precursor using the same procedure. Thus, each sample contained a nominal iron loading of ca. 1.6 wt%. Samples were named FeAc-X-KJ600-Y-Z, where X represents the nitrogen precursor (either TCNB or TCNE), Y represents the final heat-treatment temperature (700-1100^{o}C) and Z represented the gas flow used during heat-treatment (either N_2 or NH_3).

5.4 Results and Discussion

Altogether, eight samples were characterized. Six of the samples utilized TCNB as a precursor where one was left not heat-treated and the other five were heat-treated in N_2 at different final heat-treatment temperatures (700, 800, 900, 1000 and 1100^{o}C). To test the effect of a different nitrogen precursor and different flow gas during heat treatment, two other samples were synthesized: one replacing TCNB with TCNE as a precursor, and one using TCNB however heat-treated in NH_3 – these two samples were heat-treated at a heat-treatment temperature of 900^{o}C. Table 4 summarizes the synthesized catalysts and the synthesis parameters for the reader's understanding.

Table 4: Sample names and denotation for catalyst samples in this work

Sample Number	Name	Nitrogen Precursor	Final Heat-Treatment Temperature (^oC)	Pyrolysis Flow Gas
1	FeAc-TCNB-KJ600-0-N2	TCNB	N/A	N_2
2	FeAc-TCNB-KJ600-700-N2	TCNB	700	N_2
3	FeAc-TCNB-KJ600-800-N2	TCNB	800	N_2
4	FeAc-TCNB-KJ600-900-N2	TCNB	900	N_2
5	FeAc-TCNB-KJ600-1000-N2	TCNB	1000	N_2
6	FeAc-TCNB-KJ600-1100-N2	TCNB	1100	N_2
7	FeAc-TCNE-KJ600-900-N2	TCNE	900	N_2
8	FeAc-TCNB-KJ600-900-NH3	TCNB	900	NH_3

FeAc-TCNE-KJ600-900-N2 and FeAc-TCNB-KJ600-900-N2 after thermal treatments were characterized with TEM to examine the surface morphology of both structures. Figure 27 shows both the high resolution TEM images of (a) FeAc-TCNE-KJ600-900-N2 and (b) FeAc-TCNB-KJ600-900-N2. Both images show KJ600 particles sizes ranging from 30 – 50 nm in diameter with a noticeable coating of material less than 10 nm think. This coating is explained to be the result of the iron(II) acetate and the TCNE/TCNB that was mixed with the carbon black material. However, it is believed that neither the precursor materials nor the iron phthalocyanine structure remains intact after pyrolysis. Instead, decomposed constituents that remain after high

temperature thermal treatment are what form the coating surround the KJ600 particles. From the TEM images acquired, it is impossible to resolve the differences between a TCNE or TCNB precursor. Both coatings seen in (a) and (b) show a uniform coating with very small deviations in thickness. This gives evidence to a very even distribution of polymer iron phthalocyanine or monomer derivative that was coated onto the carbon substrate prior to pyrolysis.

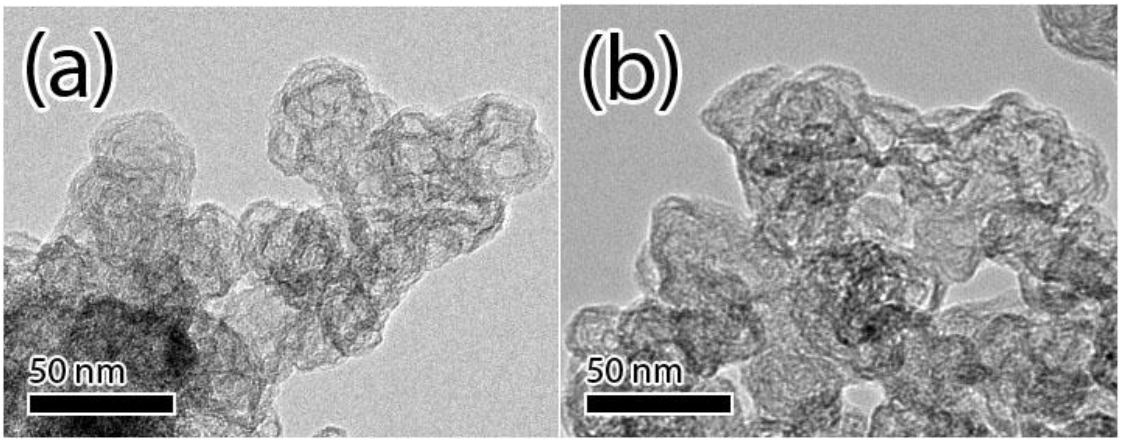

Figure 27: The samples (a) FeAc-TCNE-KJ600-900-N2 and (b) FeAc-TCNB-KJ600-900-N2 analyzed by TEM

Half-cell RRDE experiments were conducted for all the samples to determine their catalytic activity for the ORR. FeAc-TCNE-KJ600-900-N2, FeAc-TCNB-KJ600-900-N2, and FeAc-TCNB-KJ600-900-NH3 were first synthesized and plotted for comparison. These results are plotted together in Figure 28 along with an unheat-treated sample (FeAc-TCNB-KJ600-0-N2) and a commercial Pt/C (20 wt%, E-TEK) catalyst as a reference standard. All polarization curves in the graph are conducted at 900 rpm.

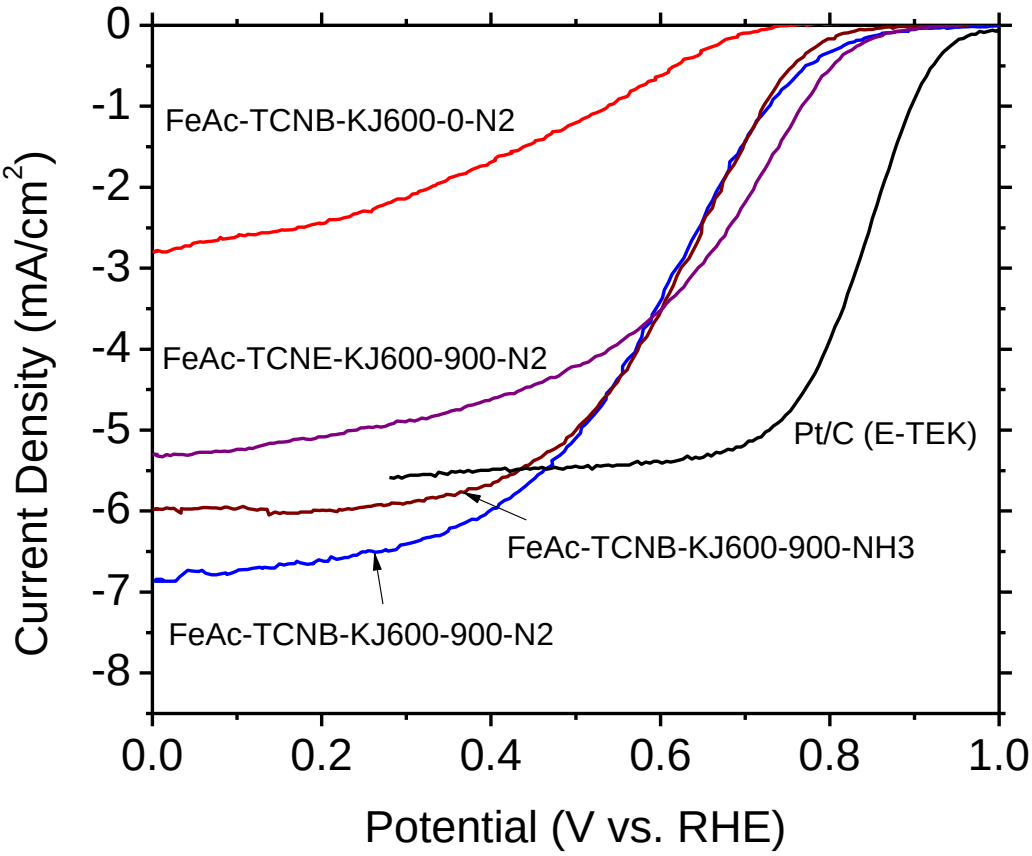

Figure 28: ORR curves for various catalysts synthesized versus Pt/C as a reference

From the figure it is apparent that the onset and half-wave potential demonstrated by the precious Pt/C catalyst outperforms all the NPMCs synthesized in this work. The required overpotential to carry out the ORR on Pt/C is far less and the reaction kinetics is quite fast. Still, this work was able to demonstrate that TCNB and TCNE as iron phthalocyanine nitrogen precursors can result in ORR active catalysts even without any precious metals. The metal loading of iron contained within the non-precious metal catalysts samples is about 1.6 wt% nominally. No attempt in this work was made to optimize the metal content in the catalysts.

In Figure 29, of the samples made, FeAc-TCNE-KJ600-900-N2 demonstrated the highest onset and half-wave performance. In terms of limiting current density, FeAC-TCNB-KJ600-900-N2 demonstrated remarkable current densities, outperforming FeAc-TCNE-KJ600-900-N2 and Pt/C. The FeAc-TCNE-KJ600-900-NH3 catalyst also showed higher limiting current densities

compared to Pt/C however, compared to the sample without ammonia treatment, the current density, onset and half-wave potentials were reduced. This gives indication that the treatment with ammonia during pyrolysis of the sample is destructive to the active sites of these types of catalysts and does lead to an improvement in the ORR performance unlike previous work done using ammonia as a nitrogen source for NPMCs. In the previous work, utilizing cyanamide, ammonia was introduced to the catalyst during heat-treatment as an additional nitrogen precursor for the synthesis. Ammonia was also found be highly influential to the catalysts BET surface area due to the fact that ammonia gasification would etch away the iron-cyanamide excess coating and uncover blocked pores on the KJ600 carbon substrate. The etching of the coating provided substantial surface area recovery compared to a sample heat-treated in just N_2. The NH_3 heat-treated sample demonstrated a dramatic increase in both half-wave and onset potential. It is surprising that ammonia treatment using TCNB would not benefit the catalyst structure in the same way. Although it is unclear whether the benefit of ammonia in previous studies was achieved through the introduction of additional nitrogen present in ammonia, through the increased surface area due to the blocking of pores, through some specific reaction with ammonia gas and the iron-cyanamide coating or some combination of these possibilities, it is hypothesized that several problems may be created for these TCNE/TCNB derived catalysts due to the introduction of the ammonia:

1) The incorporation of ammonia could affect the construction of the iron phthalocyanine monomer/polymer during the heat-treatment in the range of 300-400^{o}C. The addition of NH_3 may obstruct the formation of iron phthalocyanine or the N_4 moiety or react with its constituents causing less polymer sheet or monomer derivative to be formed. When the temperature is raised to the final heat-treatment temperature and the iron pthalocyanine units decompose, there would be fewer formed units and hence less resulting active sites from this process.
2) Ammonia could etch away or react with active site components at higher temperatures causing active sites to not form.
3) Ammonia could alter the carbon substrate properties by reacting with surface functional groups. Since the mechanics and polymerization process of iron phthalocyanine

adsorbing onto the carbon black are unknown, this process may change the adhesion of the monomeric units.

To ensure that the heat-treatment step was necessary, the non-heat-treated TCNB sample was tested in a half-cell RRDE set-up and the results are also illustrated in Figure 28. Little or no oxygen reduction activity is observed. NPMCs without heat-treatment have been reported to show some activity for the ORR and several papers conduct work on non-heat treated phthalocyanine structures for fuel cell applications. The poor performance of the FeAc-TCNB-KJ600-0-N2 sample could be an indicator that the iron phthalocyanine structure has not formed yet. In previous studies, the formation of iron phthalocyanine is carried out at a temperature of 300-400^{o}C, and hence it is not expected that any phthalocyanine has developed, rather only the initial precursors (iron(II) acetate and TCNB) may exist. The slight ORR activity that is shown in Figure 28 from the non-heat-treated catalyst may be due to the inherent catalytic activity of these precursors absorbed onto carbon black or simple the inherent catalytic activity of carbon black itself. Either way, it is understood that these types of NPMCs require a high temperature pyrolysis step to fully form and decompose the iron-phthalocyanine structure before significant activity can be observed.

As an additional endeavor, the sample employing TCNB as a precursor was heat-treated at different final temperatures in N_2 to try to optimize the synthesis procedure. Four samples were tested at different final pyroyzation temperatures (700, 800, 1000, and 1100^{o}C) in addition to the sample heat-treated at a final temperature of 900^{o}C. There is an apparent trend between the samples heat-treated at temperatures from 700-1000^{o}C. As the heat-treatment temperature increases from 700^{o}C the limiting current density, the onset potential and the half-wave potential increase steadily to a maximum of 1000^{o}C. At a final heat-treatment temperature of 1100^{o}C, the current density dramatically decreases whereas the onset potential remains the same. Figure 29 plots these 5 ORR performance plots with the inset showing the trend in limiting current densities measured at 0.4 V vs. RHE. The results of the limiting current density and the half-wave and onset potentials are tabulated in Table 5 for all the catalysts displayed in Figures 28-29.

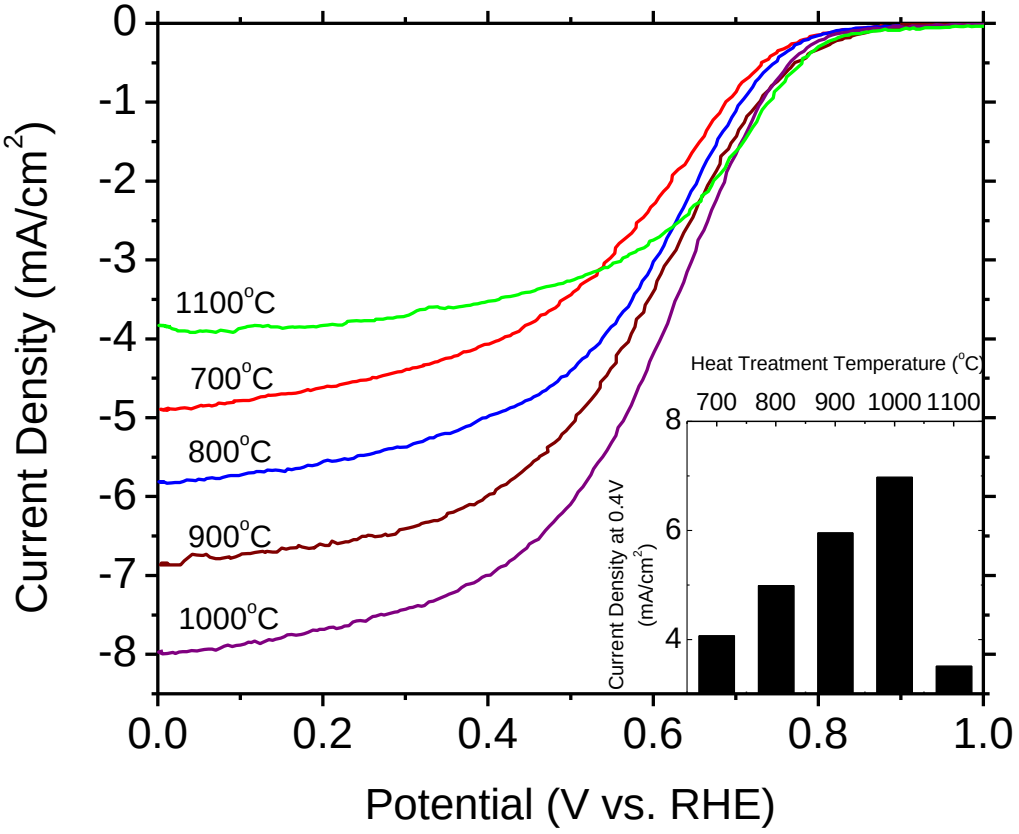

Figure 29: ORR curves of Fe-TCNB-KJ600 catalysts heat-treated in N_2 at different heat-treatment temperatures (800-1100°C). Inset shows current densities of these curves at 0.4 V

The ring currents from the RRDE experiments were exploited to gather information regarding the H_2O selectivity of the catalyst samples. High H_2O selectivity indicates a more efficient reaction pathway instead of the two electron pathway for the formation of H_2O_2. H_2O_2 is a destructive chemical in the cell as it is able to oxidize carbon surface groups in the catalyst as well as harm the Nafion membrane. Figure 30 plots the H_2O selectivity of five catalyst samples over the polarization range: FeAc-TCNE-KJ600-900-N2, FeAc-TCNB-KJ600-800-N2, FeAc-TCNB-KJ600-900-N2, FeAc-TCNE-KJ600-1000-N2, and FeAc-TCNE-KJ600-900-NH3. All catalysts show high selectivity for H_2O upwards of 90%. At 0.4 V vs. RHE, the order of the selectivity for H_2O from highest to lowest is FeAc-TCNB-KJ600-1000-N > FeAc-TCNB-KJ600-900-N2 > FeAc-TCNB-KJ600-800-N2 > FeAc-TCNB-KJ600-900-NH3 > FeAc-TCNE-KJ600-900-N2. FeAc-TCNB-KJ600-1000 shows the best H_2O selectivity of 98.7% at 0.4 V vs. RHE.

This selectivity drops with a decrease of final heat-treatment temperature. This data is in agreement with the polarization curves seen in Figure 29. Since the rotating disc speed is the same, the amount of oxygen being supplied to the working electrode is also the same. Hence the only determining factor of the limiting current density is the efficiency of the reaction. Higher limiting current densities indicate a higher selectivity for the more efficient H_2O reaction. This selectivity drops by *ca*. 1% for FeAc-TCNB –KJ600-900-N2 and another 1% for FeAc-TCNB-KJ600-800-N2. This change in selectivity for the H_2O reaction is quite significant as seen by the resulting change in limiting current densities in Figure 29.

The ammonia heat-treated sample shows lower H_2O selectivity than the sample heat-treated at 900^oC without ammonia – this is a further indication that the introduction of NH_3 has a negative consequence on these types of catalysts. The FeAc-TCNE-KJ600-900-N2 had the lowest selectivity of all the synthesized samples. This result is reflected by the lower current density shown in Figure 28 when compared to Pt/C or TCNB derived samples, even though the TCNE derived sample displayed a relatively high onset and half-wave potential. It should be mentioned that no attempt to optimize the TCNE catalyst was made in this work. Metal loading, pyrolysis temperature, and TCNE loading could be altered to possibly increase the selectivity of the catalyst.

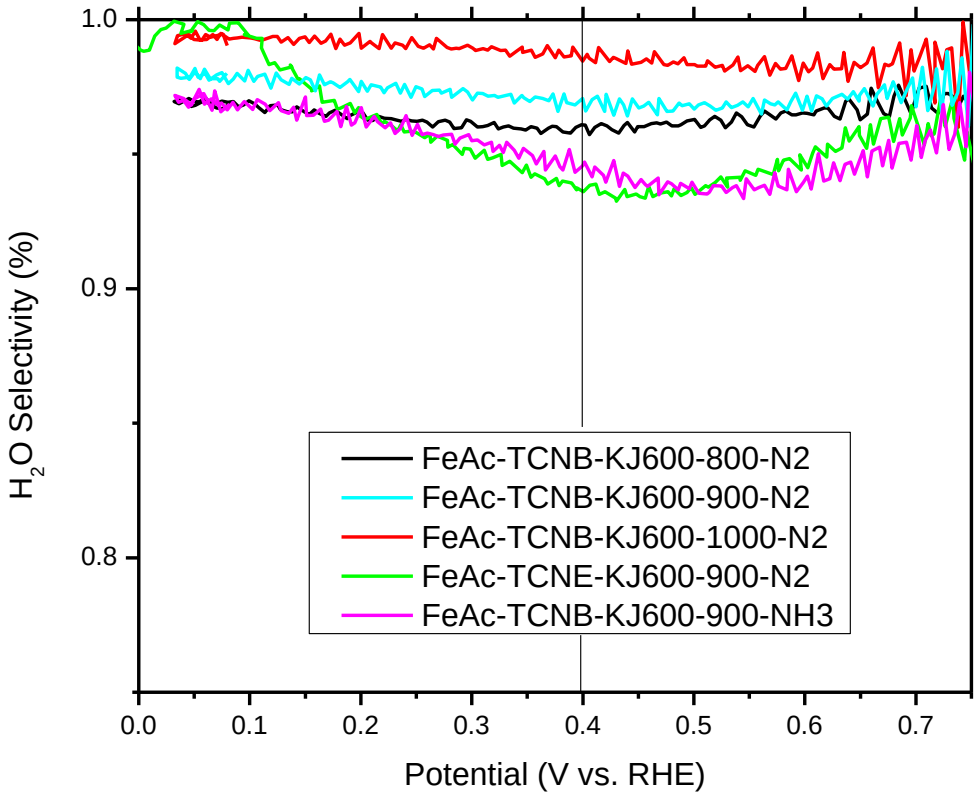

Figure 30: H_2O Selectivity for FeAc-TCNB-KJ600-800-N2, FeAc-TCNB-KJ600-900-N2, FeAc-TCNB-KJ600-1000-N2, FeAc-TCNE-KJ600-900-N2 and FeAc-TCNB-KJ600-900-NH3

For ease of comparison, current density, half-wave potential, onset potential and H_2O selectivity of all catalyst samples from Figure 28-30 are summarized in full in Table 5.

Table 5: Summary of RRDE experiments for synthesized catalyst samples

Catalyst	Current Density at 0.4 V vs. RHE (mA/cm^2)	Onset (mV vs. RHE)	Half-Wave (mV vs. RHE)	H_2O Selectivity at 0.4 V vs. RHE (%)
FeAc-TCNB-KJ600-0-N2	1.69722	736	495	--
FeAc-TCNB-KJ600-700-N2	4.06590	826	597	--
FeAc-TCNB-KJ600-800-N2	4.97357	830	608	96.1
FeAc-TCNB-KJ600-900-N2	5.96837	845	610	97.1
FeAc-TCNB-KJ600-1000-N2	7.00056	870	618	98.5
FeAc-TCNB-KJ600-1100-N2	3.52503	867	681	--
FeAc-TCNB-KJ600-900-NH3	5.68235	835	623	94.6
FeAc-TCNE-KJ600-900-N2	4.63163	895	679	93.7

XPS was utilized in this work to determine the atomic composition and bond types that exist on the surface of the catalyst samples. Figure 31 presents the wide range XPS spectra of Fe-TCNB-KJ600-900-N2. All other synthesized samples are similar to Figure 31. The XPS spectra shows the C1s, N1s and O1s peak and confirms a large percentage of carbon along with oxygen and nitrogen. Trace amounts of iron were also detected through the Fe2p3 peak. Further analysis of the surface composition allows one to infer the effect of different synthesis techniques on the surface of the carbon substrate. Table 6 summarize the overall atomic composition.

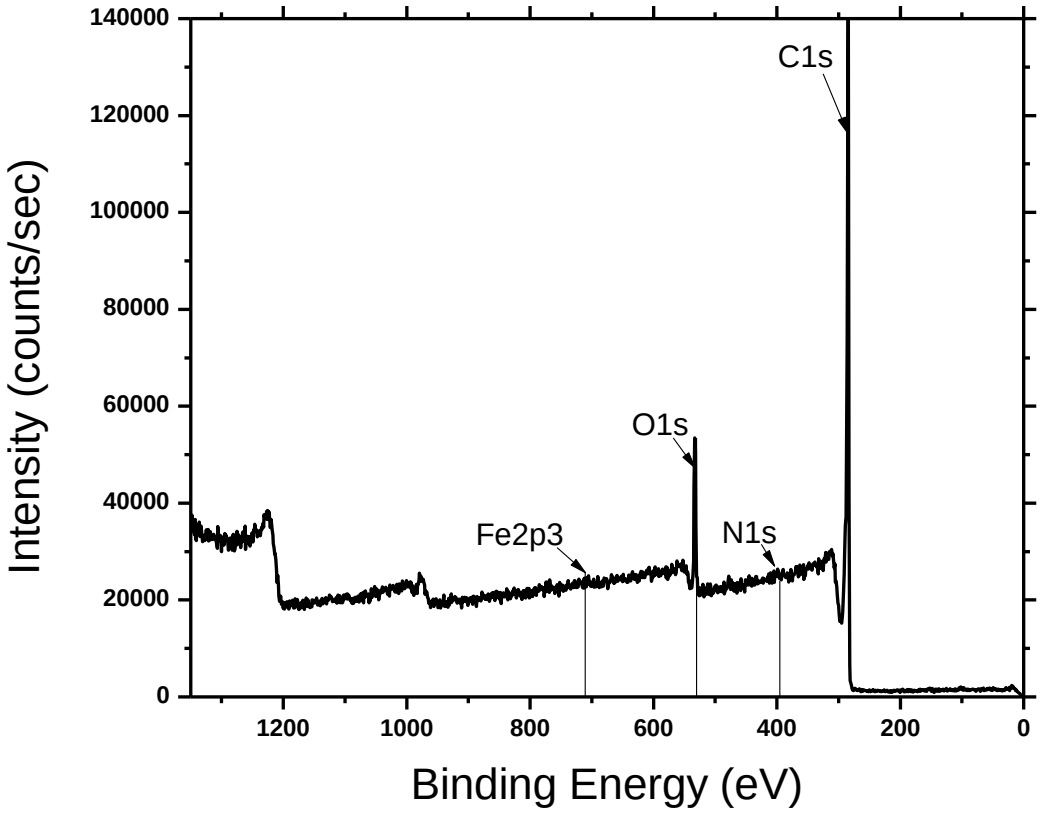

Figure 31: Wide range XPS spectra for FeAc-TCNB-KJ600-900-N2 sample

The iron content was looked at through XPS analysis. Even though the nominal iron loading was approximately 1.6 wt% the resulting pyroyzed catalyst compositions as determined by XPS all fell within the range of 0.18 - 0.32 wt% (0.04 - 0.09 at%) even the non-heat-treated sample FeAc-TCNB-KJ600-0-N2 had a surface concentration of 0.4 wt%. It is worth mentioning that at low concentrations, the XPS peaks become difficult to resolve and may not be accurate at less than 0.5 at%. Bulk concentrations of iron within the catalyst samples are expected to be lower. This poor yield of iron indicates that during the mixing and heating stage in the quinoline solvent most of the iron would remain dissolved in solution and washed away when filtered. Many previous researches indicated a much higher content of iron is optimal. Many notice that the trend for optimal ORR performance is increasing performance with iron content up until ca. 2 wt% where then the ORR performance will decrease slightly and level off after 4 wt%. The researchers investigating this trend noticed that after the sample was loaded with more than 2

wt% the iron species on the catalyst surface would form large agglomerate particles and be ineffective in the formation of active sites. The relatively small amounts of iron loaded onto the synthesized catalysts suggest that more iron could be afforded in future optimization studies dealing with precursor loading; however that is beyond the scope of this work.

Table 6: XPS summary of atomic composition for catalyst samples

Peak Analyzed	C1s Atomic %	Fe2p3 Atomic %	N1s Atomic %	O1s Atomic %
FeAc-TCNB-KJ600-0-N2	91.27	0.09	2.92	5.71
FeAc-TCNB-KJ600-700-N2	94.95	0.06	2.79	2.19
FeAc-TCNB-KJ600-800-N2	95.45	0.07	1.94	2.54
FeAc-TCNB-KJ600-900-N2	95.18	0.06	1.51	3.25
FeAc-TCNB-KJ600-1000-N2	94.70	0.07	1.19	4.05
FeAc-TCNB-KJ600-1100-N2	97.04	0.04	0.99	1.94
FeAc-TCNB-KJ600-900-NH3	96.23	0.05	1.44	2.27
FeAc-TCNE-KJ600-900-N2	94.65	0.06	1.98	3.31

For XPS analysis, the N1s peak is also of great interest to characterize the ORR active site. Since there is still a lot of speculation as to what the structure of the active site is, looking at the nitrogen bonding structures and their relative amounts compared with their ORR active performance will determine what sorts of bonds are pertinent to the active site. The N1s signal can usually be deconvoluted into four separate peaks indentifying different bond structures. Figure 32 represents these nitrogen bonding types on a graphitized carbon structure. These types

of nitrogens from lowest binding energy to highest include pyridinic (398.5 eV), pyrrolic (400.5 eV), quaternary (401.3 eV) and pyridine (404.9 eV). Since the peak location for pyrrolic and quaternary are quite similar, it is usually very difficult to distinguish between these two peaks. Figure 33 illustrates two high resolution plots of the N1s peak for all the catalyst samples. Figure 33 (a) shows the final catalysts utilizing TCNB as a precursor heat-treated at different temperatures in N_2, while Figure 33 (b) shows FeAc-TCNB-KJ600-0-N2, FeAc-TCNB-KJ600-900-N2, FeAc-TCNB-KJ600-900-NH3 and FeAc-TCNE-KJ600-900-N2 to compare the nitrogen type composition for different synthesized catalysts. Table 7 summarizes the compositions of these nitrogen structures.

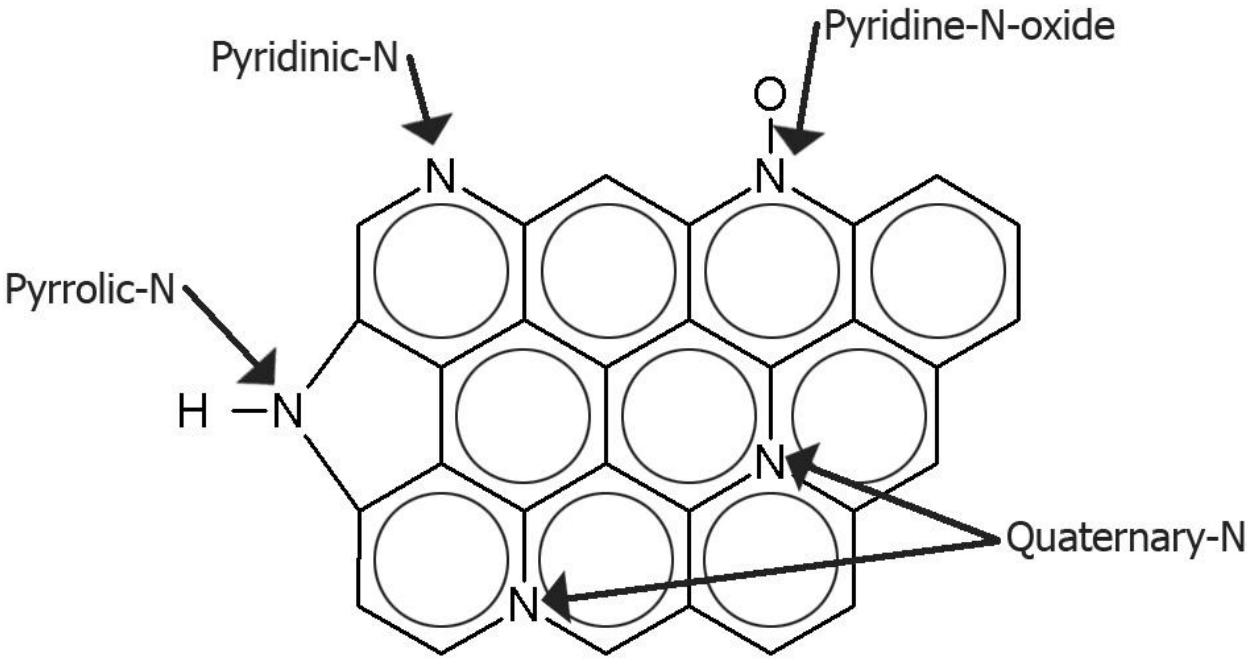

Figure 32: Different types of nitrogen characterized by XPS

From the results described on Table 7 and Figure 33, the first peak seen at ca. 398.5 eV is present in little amounts or not at all in the non-heat-treated sample (FeAc-TCNB-KJ600-0-N2). After a pyrolysis at 300^{o}C for 1 hour, 400^{o}C for 1 hour and 700^{o}C for 1 hour, the amount of pyridinic nitrogen is increased to 37.69% of all the nitrogen groups. By increasing the final pyrolysis temperature, this relative amount of pyridinic nitrogen is decreased as pyridinic nitrogen is unstable at temperatures greater than 800^{o}C. Hence, for catalysts heat-treated at higher temperatures, the relative amount of pyrindic nitrogen in the sample is lower from FeAc-TCNB-

KJ600-700-N2 > FeAc-TCNB-KJ600-800-N2 > FeAc-TCNB-KJ600-900-N2 > FeAc-TCNB-KJ600-1000-N2 > FeAc-TCNB-KJ600-1100-N2. Consequently, as it can be seen in Figure 33 (a) the amount of quaternary and pyrrolic nitrogen is increased with increasing temperature, these forms of nitrogen are stable at higher temperature. The overall nitrogen content is decreasing in the sample with increasing heat-treatment temperature. This result is unexpected. Much research is done on NPMCs and has usually found that in order to synthesize high performance catalysts for the ORR, high nitrogen contents must be achieved. In this work, the highest performing catalysts did not display high nitrogen contents or rather a high amount of any specific nitrogen bonding type. Both FeAc-TCNB-KJ600-1000-N2 which displayed the highest limiting current density and FeAc-TCNE-KJ600-900-N2 which displayed the highest onset and half-wave potential do not exemplify one type of nitrogen type. Unlike, the synthesis from previous experiments however, the nitrogen precursor was added to form iron phthalocyanine polymer sheets to form a thin planer sheet that would be decomposed and leave behind a single-atom iron centre. Previous synthesis procedures do not try to control the layer thickness of the coating and hence excess nitrogen may be present on the surface of those catalysts. The benefit to designing these polymer sheets is that the nitrogen functionalities and placement from the iron centres are fixed when the sheet is formed. Thus when the pyrolysis at high temperature begins to decompose the phthalocyanine structure, the possibilities of different nitrogen is minimal.

Figure 33 (b) illustrates the relative nitrogen contents for the FeAc-TCNE-KJ600-900-N2, FeAc-TCNB-KJ600-900-NH3. Both these catalysts show very similar compositions not only in nitrogen types but overall elemental composition as well. The TCNE precursor contains a higher ratio of nitrogen to carbon, and hence it can be seen that the nitrogen content is slightly higher for the FeAc-TCNE-KJ600-900-N2 sample compared to the FeAc-TCNB-KJ600-900-N2. The TCNB sample heat-treated in ammonia showed similar elemental composition to the FeAc-TCNE-KJ600-900-N2 and FeAc-TCNB-KJ600-900-N2 samples however had slightly less nitrogen and oxygen. This result was also counter intuitive as it was thought that ammonia would be a source of nitrogen for functionalities on the carbon black and hence increase the nitrogen content of the sample. Ammonia does however act as an etching gas and can remove functionalities from the carbon surface as seen in the last section. By this hypothesized route,

ammonia could react with the nitrogen and oxygen surface species on the carbon and produce nitrogen gas and water as products which leave the pyrolysis reactor as gases. This gives an explanation as to why there are decreased nitrogen and oxygen amounts in the FeAc-TCNB-KJ600-900-NH3 sample.

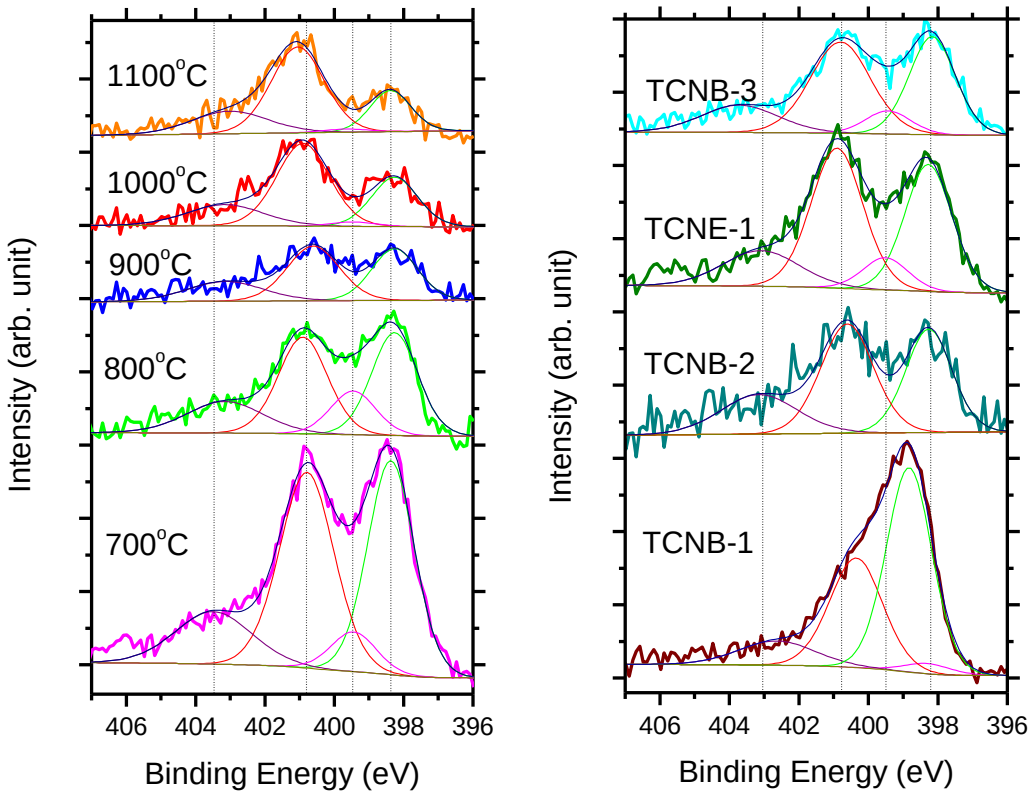

Figure 33: N1s spectra of (a) TCNB derived catalysts heat-treated at different temperatures in N_2, (b) FeAc-TCNB-KJ600-0-N2, FeAc-TCNB-KJ600-900-N2, FeAc-TCNE-KJ600-900-N2, and FeAc-TCNB-KJ600-900-NH3

Table 7: XPS summary of nitrogen content of catalyst samples

Peak Analyzed	N1	N2	N3	N4
	Atomic %	Atomic %	Atomic %	Atomic %
FeAc-TCNB-KJ600-0-N2	2.73	33.27	10.69	53.32
FeAc-TCNB-KJ600-700-N2	37.69	40.27	15.21	6.82
FeAc-TCNB-KJ600-800-N2	34.09	34.29	17.37	14.25
FeAc-TCNB-KJ600-900-N2	26.40	45.63	26.29	1.68
FeAc-TCNB-KJ600-1000-N2	26.94	51.60	19.10	2.36
FeAc-TCNB-KJ600-1100-N2	20.68	56.29	21.25	1.79
FeAc-TCNB-KJ600-900-NH3	34.46	41.66	15.90	7.97
FeAc-TCNE-KJ600-900-N2	34.37	41.62	15.65	8.37

XRD analysis was done on each sample to verify the crystalline phases present in each catalyst. Figure 34 shows the wide range diffraction pattern of FeAc-TCNB-KJ600-1000-N2 as a representative plot for all samples since there is little difference between the samples. The other synthesized catalyst diffraction patterns are not shown here. All diffraction patterns show a peak at $2\theta=26.0$ corresponding to the (002) graphitic peak of carbon. Peaks located at 38.2, 42.4, 44.4, 64.8, 78.0, and 98.8 represent various iron species (i.e. Iron carbides, α-Fe and γ-Fe). These peaks confirm the various structures of iron contained within all the samples.

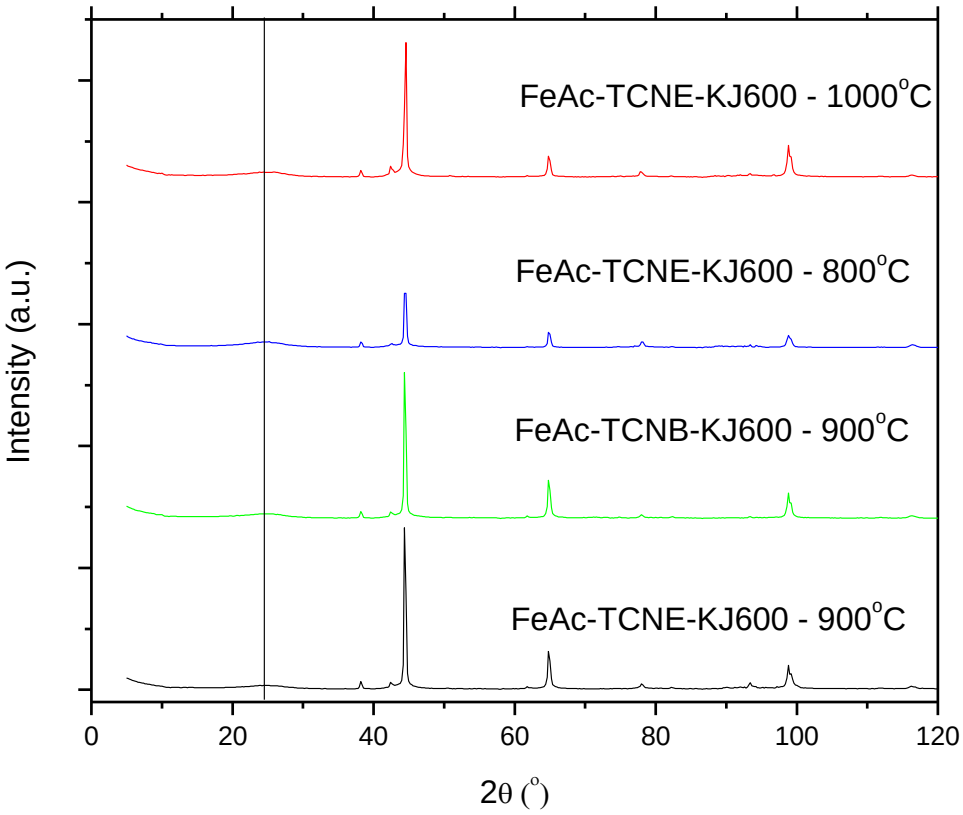

Figure 34: XRD diffraction patterns confirming various crystalline phases of iron and carbon

TGA was carried out on the TCNB derived catalyst heat-treated at different temperatures (700 – 1100°C) in oxygen. The weight loss versus temperature curves are illustrated in Figure 35a where *ca*. 3.5 mg of each catalyst sample was burned in air until all the carbonaceous species were burned off. Therefore, the percentage remaining of each catalyst starts from 100% and at sufficiently high enough temperatures (>675°C), drops to less than 3% of the original weight. The remaining content after burning in air represents the metal content and ash content of the bulk catalyst material. Due to the oxidation of the metals, the remaining iron content probably exists in different oxide phases (i.e. FeO, Fe_3O_4, Fe_2O_3), thus the final mass of the burned catalysts were not used as the bulk iron content in the original samples. From Figure 35a, an obvious trend occurs where the change in mass drops at higher temperatures for catalyst heat-treated in higher temperatures. This mass change is more apparent in Figure 35b illustrating the derivative weight change versus the temperature. Figure 35b shows the burning of the catalysts

begins as early as 350^{o}C and completely finishes burning at 675^{o}C. The peaks in Figure 35b represent the burning of carbonaceous species. For FeAc-TCNB-KJ600-700-N2 four distinct peaks are observed centered at 410^{o}C, 440^{o}C, 470^{o}C and 490^{o}C. The low rate of weight loss observed at 410^{o}C is due to the destruction of iron phthalocyanine units which have not fully decomposed after a heat-treatment at 700^{o}C. This is why this peak is not apparent for the other catalyst samples which have been heat-treated at higher temperatures. At temperatures 800oC and higher, the iron phthalocyanine units have been fully decomposed from pyrolysis and no such structures exist on the carbon surface of these resulting catalyst. Due to the peak size and the rate of mass loss, the peak seen in the FeAc-TCNB-KJ600-700-N2 TGA differential curve at 470^{o}C represents the decomposition of the functional groups present on the carbon black. These functional groups are not present in the catalysts heat-treated at higher temperatures because at higher pyrolysis temperatures, these functional groups have already been burned off during the synthesis of the catalysts. 700^{o}C was not sufficiently high enough to burn off these functional groups on the carbon black. At 440 and 470^{o}C burning of amorphous carbons is suspected - each peak representing a different purity of graphitized carbon. These two peaks are present in all the TCNB derived catalysts heat-treated at higher temperatures, however are shifted to the right illustrating a higher thermal stability. This higher stability in the catalyst heat-treated at higher temperatures indicates a higher graphitic order in the carbon. Graphitic carbon has a much higher resistance to high temperatures compared to amorphous carbon and thus a higher graphitic content in the catalyst results in higher thermal stability as seen by the TGA curves. This graphitic content was created by conducting the pyrolysis at higher temperature in N_2. The weight change peaks shift right to higher temperatures in Figure 35b because of the higher purity of graphitized carbon. It is well-known that graphitized carbon has superior electroconductive properties over amorphous carbon. Graphitized carbon has also shown to increase the chemical stability of Fe-N/C catalysts from oxidative species such as H_2O_2 and CO. It is believed that this increased graphitic content seen in catalysts with higher pyrolysis temperatures improves the overall performance and durability of these TCNB derived catalysts.

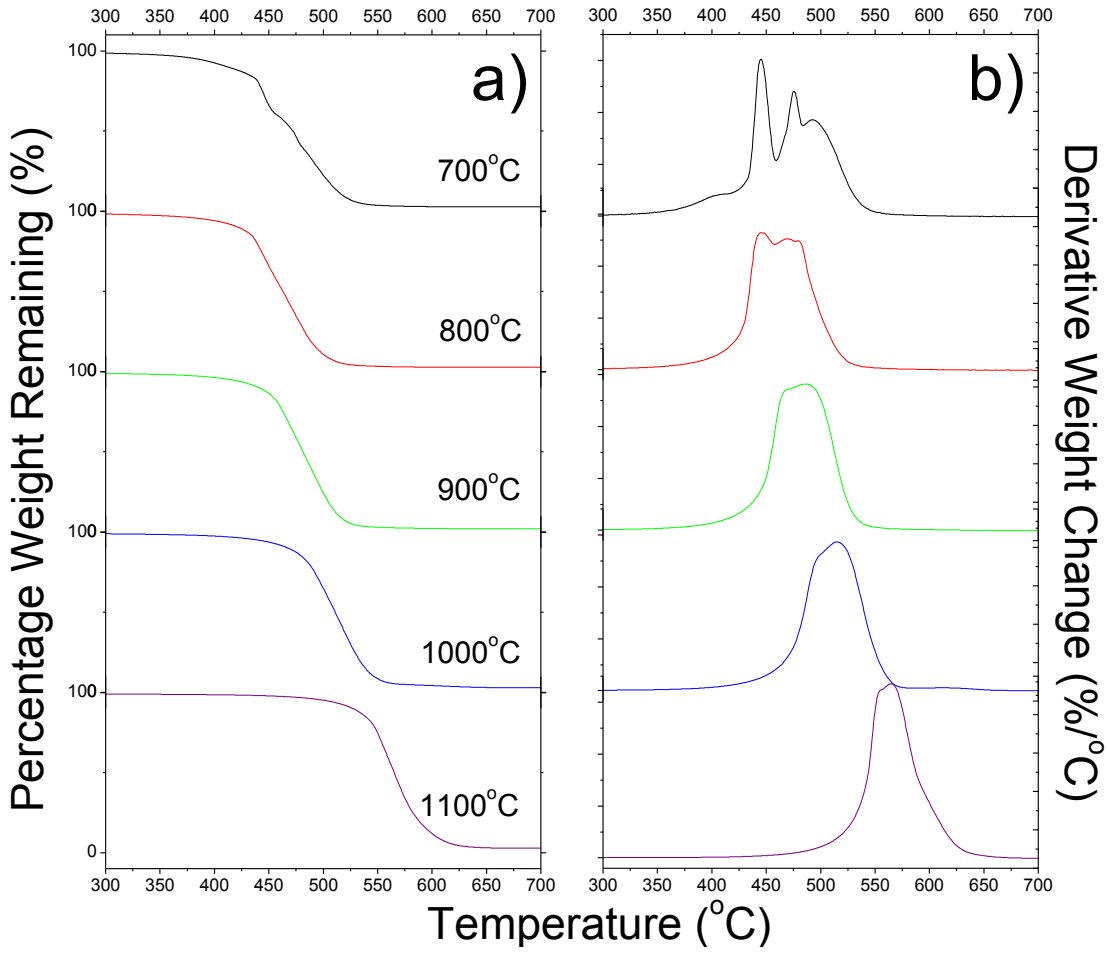

Figure 35: Thermogravimetric analysis of TCNB derived catalysts heat-treated at different temperatures: a) percentage weight remaining versus temperature and b) derivative weight change versus temperature of the corresponding catalyst TGA curve

5.5 Conclusions

In this work, seven NPMCs were successfully synthesized and tested for the ORR. These samples were electrochemically tested in a RRDE half-cell setup in 0.1 M $HClO_4$. Of the seven samples, FeAc-TCNE-KJ600-900-N2 performed the best with respect to onset and half-wave potentials which were tested to be 895 and 679 mV vs RHE respectively. Although this catalyst performed adequately against the other synthesized samples, it is still lacking compared to precious electrocatalysts such as Pt/C. FeAc-TCNB-KJ600-900-N2 also achieved a relatively high ORR performance with onset and half-wave potentials of 845 and 610 mV, however the

limiting current density for FeAc-TCNB-KJ600-900-N2 (5.97 mA/cm^2) was seen to be dramatically greater than Pt/C (5.48 mA/cm^2).

Upon optimizing the final temperature of the pyrolysis for the TCNB catalyst the limiting current density was raised to 7.00 mA/cm^2 for FeAc-TCNB-KJ600-1000-N2. Ammonia was found to be destructive as a pyrolysis gas due to the etching away of oxygen and nitrogen from the carbon surface and the non-heat-treated sample was found to be not active for the ORR. The existence of a polymer network on the carbon surface after a pyrolysis of 300-400^oC is still unconfirmed. Several analysis techniques were employed during this phase to gather more data regarding the morphology and composition of these TCNB and TCNE derived catalysts.

- **TEM:** The surface morphology was investigated. Both the FeAc-TCNB-KJ600-900-N2 and FeAc-TCNE-KJ600-900-N2 derived catalysts showed a layer <10 nm thick indicating a coating had been adsorbed onto the surface of the carbon black followed by a pyrolysis.

- **XPS:** Surface composition was determined through broad range XPS scans as well as narrow ranged scans focused on the N1s signal. It was showed that the catalyst with the highest limiting current density had high relative amounts of quaternary/pyrrolic nitrogen groups which was hypothesized to be beneficial for the structure of the active site.

- **XRD:** From the diffractograms, various crystalline materials were observed in the catalyst structures. Graphitic carbon was present in the carbon black, as well as different structures of iron which was present as mainly α-Fe and Fe_3C.

- **TGA:** The graphitic nature of carbon increased providing greater thermal stability for the overall catalysts heat-treated at higher temperatures. This higher graphitic nature, increases the chemical stability as well as the electroconductivity of the carbon support which is beneficial for a fuel cell catalyst.

Future work to identify this network structure is necessary to understand the reasoning behind this high limiting current result.

Section 6: Summary and Future Work

In summary, three different experiments were carried out to explore three different types of nitrogen precursors for non-precious heat-treated metal catalysts for the ORR. The first experiment utilized EDA, a commonly employed nitrogen precursor known for its high nitrogen to carbon ratio and its ability to effectively catalyze the ORR after pyrolysis. Four different samples were synthesized on carbon blacks of different porosities, KJ600 and KJ300. Of the two, KJ600 demonstrated higher onset and half-wave potentials for the ORR. It was concluded that the higher porosity and surface area demonstrated by the KJ600, led to the facilitation of greater number of catalytic active sites being formed. The two carbon substrates were also evaluated after a modification of the procedure to include a reflux while coating the carbon black. This reflux allowed for a thicker coating of precursor material to be adsorbed onto the carbon surface before the pyrolysis step. It was found that including a reflux stage improved the ORR performance significantly for the resulting FeCo-EDA-KJ600R and FeCo-EDA-KJ300R catalysts.

Future work to be carried out for these sorts of catalysts could involve seeking further improvement of the ORR performance. Strategies to optimize the metal and precursor loading, the heat-treatment temperature, and pyrolysis gases may be worth examining. Several researches, including the work done in Section 4, made use of a second coating and pyrolysis step to increase active site density on the high surface area carbon. Such strategies can be adopted for the FeCo-EDA-KJ600 catalyst as the synthesis procedures are very similar. Further characterization of the synthesized catalysts should be carried out to better understand the structure and mechanism experienced by the catalysts samples. Durability studies would give an idea as to the stability of the NPMCs to see if they can meet fuel cell application criteria.

The work presented in Section 4 made use of cyanamide as a high pyridinic type nitrogen provider after pyrolysis. A synthesis procedure similar to the experiment in Section 3 was employed and similar analysis was carried out to determine the resulting ORR performance for

the synthesized catalysts. Different synthesis procedures were used to prepare four different catalyst samples:

Table 8: Naming of Fe-cyan-KJ600 catalysts and procedural changes to each catalyst sample

Catalyst name	Procedural Change
Fe-cyan-KJ600-1	Similar procedure in Section 4, at a heat-treatment temperature of 1000^{o}C
Fe-cyan-KJ600-2	Same procedure to synthesize Fe-cyan-KJ600-1 however, 100 sccm of NH_3 was flowed in the reaction chamber during pyrolysis
Fe-cyan-KJ600-3	Sample Fe-cyan-KJ600-2 was ball-milled for three hours, and then the underwent a synthesis procedure again with half loading of iron(II) sulphate and cyanamide to increase active site density.
Fe-cyan-KJ600-4	Sample 3 was repeated, however no ball-milling stage between coating and pyrolysis procedures was used.

The samples were examined for the ORR through half-cell testing and it was found that the order of the catalytic activity from highest to lowest was Fe-cyan-KJ600-4 > Fe-cyan-KJ600-3 > Fe-cyan-KJ600-2 > Fe-cyan-KJ600-1. The effects of ammonia and a second re-coating and pyrolysis were seen to be beneficial for the onset and half-wave potential of the resulting catalyst. In addition the nitrogen content on the sample surface was increased due to both procedure modifications. Ball-milling the sample prior to coating was deemed to be destructive for the BET surface area since the pores would be crushed thus creating a poorer ORR plot.

Several modifications to this experiment could be explored to better understand this cyanamide-derived catalyst.

- Experimentations with increased number of heat-treatments and coatings steps could determine the extent to which the number of coatings and heat-treatments affects the ORR performance.
- Iron and cyanamide loadings should be varied to determine optimal amounts such that active sites can be easily formed on the surface of the carbon during pyrolysis.

- Further characterizations of the catalyst surface should be carried out to understand the functionalities and species present. Time-of-Flight Secondary Ion Mass Spectrometry (ToF-SIMS), FTIR, and Raman spectroscopy could be used to gather more information.
- Durability of the catalyst in acidic conditions is also an important feature to study as fuel cell catalysts must be able to endure for thousands of hours within a fuel cell to be considered for applications.

Section 5 was the final phase of work done in this thesis. The work focused on designing a polymer network of iron phthalocyanine sheet polymer from novel precursors (TCNB and TCNE). Seven catalyst samples were made which used different synthesis parameters summarized in Table 5. Of the catalyst samples, FeAc-TCNE-KJ600-900-N2 showed the greatest onset and half-wave. This catalyst sample however, showed poor limiting current density. FeAc-TCNB-KJ600-900-N2 showed much greater current density and was heat-treated at different final temperatures ranging from 700-1100. Of these, FeAc-TCNB-KJ600-1000-N2 showed the greatest current density. Ammonia treatment did not improve the results of this catalyst.

Much work still needs to be done to fully characterize these results. Most importantly, the iron phthalocyanine structure needs to be identified to ensure the polymer sheet exists prior to heat-treatment. FTIR analysis during the pyrolysis or at various stages during the pyrolysis stage needs to be carried out to investigate the types of bonds that exist in the catalyst. Optimization of the TCNE derived sample should be carried out to increase the performance of this catalyst system.

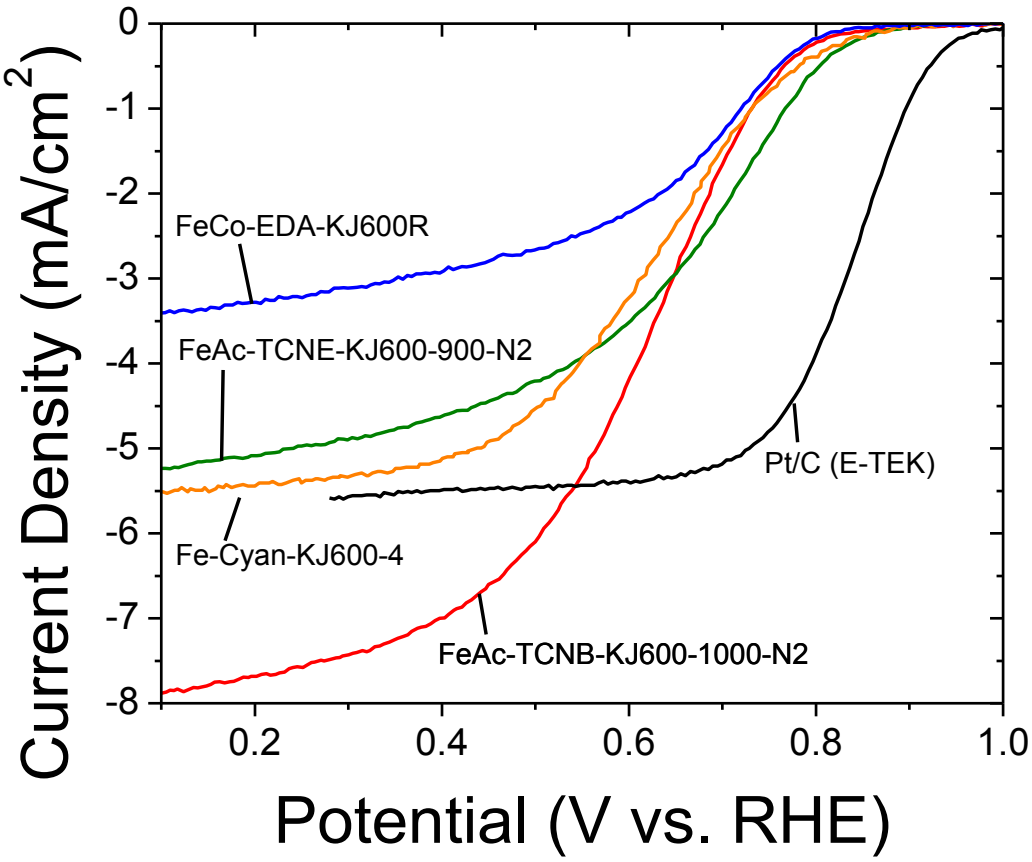

Figure 36: Summary of the ORR curves for the best catalyst shown from each phase of work

Figure 36 shows the ORR polarization curves for the best catalysts prepare in each phase of work. As reference, commercial grade Pt/C is also shown. NPMCs still have a long way to go to obtain the performance benchmark of platinum based catalysts.

References

[1] S. Lasher, J. Sinha, Y. Yang, S. Sriramulu, Direct Hydrogen PEMFC Manufacturing Cost Estimation for Automotive Applications, TIAX LLC, 2007.

[2] J. Zhang, I. NetLibrary, PEM fuel cell electrocatalysts and catalyst layers: fundamentals and applications, Springer, 2008.

[3] J. Wu, X. Yuan, J. Martin, H. Wang, J. Zhang, J. Shen, S. Wu, W. Merida, Journal of Power Sources 184 (2008) 104-119.

[4] L. Zhang, J. Zhang, D. Wilkinson, H. Wang, Journal of Power Sources 156 (2006) 171-182.

[5] C. Bezerra, L. Zhang, K. Lee, H. Liu, A. Marques, E. Marques, H. Wang, J. Zhang, Electrochimica Acta 53 (2008) 4937-4951.

[6] R. O'Hayre, S. Lee, S. Cha, F. Prinz, Journal of Power Sources 109 (2002) 483-493.

[7] M. Wilson, S. Gottesfeld, Journal of the Electrochemical Society 139 (1992) L28.

[8] D. Gruber, N. Ponath, J. Müller, F. Lindstaedt, Journal of Power Sources 150 (2005) 67-72.

[9] E. Antolini, Applied Catalysis B: Environmental 74 (2007) 337-350.

[10] H. Colón-Mercado, B. Popov, Journal of Power Sources 155 (2006) 253-263.

[11] S. Mukerjee, S. Srinivasan, Journal of Electroanalytical Chemistry 357 (1993) 201-224.

[12] H. Meng, P. Shen, J. Phys. Chem. B 109 (2005) 22705-22709.

[13] H. Meng, P. Shen, Chemical communications 2005 (2005) 4408-4410.

[14] B. Wang, Journal of Power Sources 152 (2005) 1-15.

[15] M. Lefevre, E. Proietti, F. Jaouen, J. Dodelet, Science 324 (2009) 71.

[16] Z. Chen, D. Higgins, A. Yu, L. Zhang, J. Zhang, Article in press (2010).

[17] Y. Feng, N. Alonso-Vante, physica status solidi (b) 245 (2008) 1792-1806.

[18] X. Li, B. Popov, T. Kawahara, H. Yanagi, Journal of Power Sources.

[19] D. Ohms, S. Herzog, R. Franke, V. Neumann, K. Wiesener, S. Gamburcev, A. Kaisheva, I. Iliev, Journal of Power Sources 38 (1992) 327-334.

[20] A. Widelöv, R. Larsson, Electrochimica Acta 37 (1992) 187-197.

[21] R. Jiang, D. Chu, Journal of the Electrochemical Society 147 (2000) 4605.

[22] J. Maruyama, I. Abe, Journal of the Electrochemical Society 154 (2007) B297.

[23] D. Chu, R. Jiang, Solid State Ionics 148 (2002) 591-599.

[24] M. Manzoli, F. Boccuzzi, Journal of Power Sources 145 (2005) 161-168.

[25] P. He, M. Lefevre, G. Faubert, J. Dodelet, Journal of New Materials for Electrochemical Systems 2 (1999) 243-252.

[26] S. Gupta, D. Tryk, I. Bae, W. Aldred, E. Yeager, Journal of Applied Electrochemistry 19 (1989) 19-27.

[27] K. Sawai, N. Suzuki, Journal of the Electrochemical Society 151 (2004) A682.

[28] P. Matter, L. Zhang, U. Ozkan, Journal of Catalysis 239 (2006) 83-96.

[29] G. Lalande, G. Faubert, R. Cote, D. Guay, J. Dodelet, L. Weng, P. Bertrand, Journal of Power Sources 61 (1996) 227-237.

[30] F. Charreteur, F. Jaouen, S. Ruggeri, J. Dodelet, Electrochimica Acta 53 (2008) 2925-2938.

[31] A. Freund, J. Lang, T. Lehmann, K. Starz, Catalysis Today 27 (1996) 279-283.

[32] Z. Wen, J. Liu, J. Li, Advanced materials 20 (2008) 743-747.

[33] S. Joo, C. Pak, D. You, S. Lee, H. Lee, J. Kim, H. Chang, D. Seung, Electrochimica Acta 52 (2006) 1618-1626.

[34] E. Ambrosio, C. Francia, M. Manzoli, N. Penazzi, P. Spinelli, International Journal of Hydrogen Energy 33 (2008) 3142-3145.

[35] X. Wang, J. Lee, Q. Zhu, J. Liu, Y. Wang, S. Dai, Chemistry of Materials 22 2178-2180.

[36] X. Wang, W. Li, Z. Chen, M. Waje, Y. Yan, Journal of Power Sources 158 (2006) 154-159.

[37] H. Tang, J. Chen, Z. Huang, D. Wang, Z. Ren, L. Nie, Y. Kuang, S. Yao, Carbon 42 (2004) 191-197.

[38] Z. Chen, D. Higgins, H. Tao, R. Hsu, The Journal of Physical Chemistry C 113 (2009) 21008-21013.

[39] D. Guo, H. Li, Journal of Electroanalytical Chemistry 573 (2004) 197-202.

[40] S. Maldonado, K. Stevenson, J. Phys. Chem. B 109 (2005) 4707-4716.

[41] J. Zheng, X. Zhang, P. Li, J. Zhu, X. Zhou, W. Yuan, Electrochemistry Communications 9 (2007) 895-900.

[42] K. Lee, J. Zhang, H. Wang, D. Wilkinson, Journal of Applied Electrochemistry 36 (2006) 507-522.

[43] J. Zheng, X. Zhang, P. Li, X. Zhou, W. Yuan, Catalysis Today 131 (2008) 270-277.

[44] P. Matter, U. Ozkan, Catalysis Letters 109 (2006) 115-123.

[45] Z. Zhou, X. Gao, J. Yan, D. Song, M. Morinaga, Carbon 42 (2004) 2677-2682.

[46] H. Chhina, D. Susac, S. Campbell, O. Kesler, Electrochemical and Solid-State Letters 12 (2009) B97.

[47] H. Chhina, S. Campbell, O. Kesler, Journal of Power Sources 161 (2006) 893-900.

[48] H. Chhina, S. Campbell, O. Kesler, Journal of Power Sources 164 (2007) 431-440.

[49] H. Chhina, S. Campbell, O. Kesler, Journal of the Electrochemical Society 154 (2007) B533.

[50] H. Chhina, S. Campbell, O. Kesler, Journal of Power Sources 179 (2008) 50-59.

[51] Y. Suzuki, A. Ishihara, S. Mitsushima, N. Kamiya, K. Ota, Electrochemical and Solid-State Letters 10 (2007) B105.

[52] G. Liu, X. Li, P. Ganesan, B. Popov, Electrochimica Acta 55 (2010) 2853-2858.

[53] X. Li, B. Popov, T. Kawahara, H. Yanagi, Journal of Power Sources (2010).

[54] V. Nallathambi, J. Lee, S. Kumaraguru, G. Wu, B. Popov, Journal of Power Sources 183 (2008) 34-42.

[55] J. Choi, R. Hsu, Z. Chen, The Journal of Physical Chemistry C 114 (2010) 8048-8053.

[56] N. Subramanian, S. Kumaraguru, H. Colon-Mercado, H. Kim, B. Popov, T. Black, D. Chen, Journal of Power Sources 157 (2006) 56-63.

[57] B. Popov, X. Li, G. Liu, J. Lee, International Journal of Hydrogen Energy.

[58] T. Wood, Z. Tan, A. Schmoeckel, D. O'Neill, R. Atanasoski, Journal of Power Sources 178 (2008) 510-516.

[59] M. Lefèvre, E. Proietti, F. Jaouen, J. Dodelet, Iron-based Catalysts for Oxygen Reduction in PEM Fuel Cells: Expanded Study Using the Pore-filling Method, ECS, 2009.

[60] H. Wang, R. Cote, G. Faubert, D. Guay, J. Dodelet, Journal of Physical Chemistry B-Condensed Phase 103 (1999) 2042-2049.

[61] M. Bron, S. Fiechter, M. Hilgendorff, P. Bogdanoff, Journal of Applied Electrochemistry 32 (2002) 211-216.

[62] R. Cote, G. Lalande, D. Guay, J. Dodelet, G. Denes, Journal of the Electrochemical Society 145 (1998) 2411.

[63] M. Alves, J. Dodelet, D. Guay, M. Ladouceur, G. Tourillon, The Journal of Physical Chemistry 96 (1992) 10898-10905.

[64] A. Bouwkamp-Wijnoltz, W. Visscher, J. Van Veen, S. Tang, Electrochimica Acta 45 (1999) 379-386.

[65] J. Zhang, L. Zhang, C. Bezerra, H. Li, Z. Xia, A. Marques, E. Marques, Electrochimica Acta 54 (2009) 1737-1743.

[66] L. Zhang, K. Lee, C. Bezerra, J. Zhang, Electrochimica Acta 54 (2009) 6631-6636.

[67] G. Faubert, R. Cote, D. Guay, J. Dodelet, G. Denes, P. Bertrandc, Electrochimica Acta 43 (1998) 341-353.

[68] P. Matter, E. Wang, U. Ozkan, Journal of Catalysis 243 (2006) 395-403.

[69] F. Jaouen, S. Marcotte, J. Dodelet, G. Lindbergh, J. Phys. Chem. B 107 (2003) 1376-1386.

[70] M. Lefevre, J. Dodelet, P. Bertrand, J. Phys. Chem. B 109 (2005) 16718-16724.

[71] M. Lefèvre, J. Dodelet, Electrochimica Acta 48 (2003) 2749-2760.

[72] C. Medard, M. Lefevre, J. Dodelet, F. Jaouen, G. Lindbergh, Electrochimica Acta 51 (2006) 3202-3213.

[73] F. Charreteur, F. Jaouen, J. Dodelet, Electrochimica Acta 54 (2009) 6622-6630.

[74] J. Herranz, F. Jaouen, J. Dodelet, Electrochemical Evidence of Two Types of Active Sites for Oxygen Reduction in Fe-based Catalysts, ECS, 2009.

[75] G. Faubert, R. Cote, J. Dodelet, M. Lefevre, P. Bertrand, Electrochimica Acta 44 (1999) 2589-2603.

[76] D. Villers, X. Jacques-Bédard, J. Dodelet, Journal of the Electrochemical Society 151 (2004) A1507.

[77] F. Jaouen, F. Charreteur, J. Dodelet, Journal of the Electrochemical Society 153 (2006) A689.

[78] E. Proietti, J. Dodelet, Ballmilling of carbon supports to enhance the performance of Fe-based electrocatalysts for oxygen reduction in PEM fuel cells, ECS, 2008.

[79] F. Charreteur, S. Ruggeri, F. Jaouen, J. Dodelet, Electrochimica Acta 53 (2008) 6881-6889.

[80] S. Barazzouk, M. Lefevre, J. Dodelet, Journal of the Electrochemical Society 156 (2009).

[81] J. Herranz, M. Lefèvre, J. Dodelet, Journal of the Electrochemical Society 156 (2009) B593.

[82] E. Proietti, S. Ruggeri, J. Dodelet, Journal of the Electrochemical Society 155 (2008) B340.

[83] Product Data Sheet, Akzo Nobel Polymer Chemicals B.V., Chicago, 2008.

[84] Product Data Sheet, Chicago, 2010.

[85] X. Wang, H. Zhang, J. Zhang, H. Xu, Z. Tian, J. Chen, H. Zhong, Y. Liang, B. Yi, Electrochimica Acta 51 (2006) 4909-4915.

[86] N. Krishnankutty, M. Vannice, Chemistry of Materials 7 (1995) 754-763.

[87] A. Sirk, S. Campbell, V. Birss, Electrochemical and Solid-State Letters 8 (2005) A104.

[88] N. Alexeyeva, E. Shulga, V. Kisand, I. Kink, K. Tammeveski, Journal of Electroanalytical Chemistry.

[89] D. Higgins, Z. Chen, Z. Chen, Electrochimica Acta Article in Press (2010).

[90] H. Chung, C. Johnston, P. Zelenay, Synthesis and Evaluation of Heat-treated, Cyanamide-derived Non-precious Catalysts for Oxygen Reduction, ECS, 2009.

[91] H. Chung, C. Johnston, K. Artyushkova, M. Ferrandon, D. Myers, P. Zelenay, Electrochemistry Communications (2010).

[92] M. Groenewolt, M. Antonietti, Advanced materials 17 (2005) 1789-1792.

[93] F. Moser, A. Thomas, Journal of Chemical Education 41 (1964) 245.

[94] D. Boston, J. Bailar Jr, Inorganic Chemistry 11 (1972) 1578-1583.

[95] C. Fadley, Progress in Surface Science 16 (1984) 275-388.

[96] C. Fadley, R. Baird, W. Siekhaus, T. Novakov, S. Bergström, Journal of Electron Spectroscopy and Related Phenomena 4 (1974) 93-137.

[97] D. Turner, M. Al Jobory, The Journal of Chemical Physics 37 (1962) 3007.

[98] C. Jeffree, N. Read, Hall, J, L,, Hawes, C, R ed (s). Electron microscopy of plant cells.. Academic Press: London (1991) 313-413.

[99] L. De Broglie, R. Lindsay, Physics Today 18 (1965) 67.

[100] D. Williams, C. Carter, Transmission Electron Microscopy (2009) 3-22.

[101] P. Hawkes, Academic Press: London 633 (1985) 242-243.

[102] L. Azároff, R. Kaplow, N. Kato, R. Weiss, A. Wilson, R. Young, X-ray Diffraction, McGraw-Hill New York, 1974.

[103] B. Cullity, S. Stock, Elements of X-ray Diffraction, Addison-Wesley Reading, MA, 1978.

[104] P. Griffiths, J. De Haseth, Fourier transform infrared spectrometry, Wiley-Interscience, 2007.

[105] C. Banwell, E. McCash, Fundamentals of molecular spectroscopy, McGraw-Hill London, 1983.

[106] J. Beauchaine, J. Peterman, R. Rosenthal, Microchimica Acta 94 (1988) 133-138.

[107] C. Duval, R. Oesper, E. Ralph, (1963).

[108] S. Brunauer, P. Emmett, E. Teller, Journal of the American Chemical Society 60 (1938) 309-319.

[109] F. Jaouen, M. Lefèvre, J. Dodelet, M. Cai, J. Phys. Chem. B 110 (2006) 5553-5558.

[110] R.S. Hsu, Z. Chen, ECS Transactions 28 (2010) 39-46.

Appendix A: Scientific Contributions

- Refereed Publications

R.S. Hsu, D. Higgins, Dr. Z. Chen 2010. "Tin-oxide-coated single-walled carbon nanotube bundles supporting platinum electrocatalysts for direct ethanol fuel cells". Nanotechnology. Vol. 21, 165705.

J.Y. Choi, **R.S. Hsu**, Dr. Z. Chen 2010. "Highly Active Porous Carbon-Supported Nonprecious Metal-N Electrocatalyst for Oxygen Reduction Reaction in PEM Fuel Cells". Journal of Physical Chemistry C, Vol. 114, No. 17, 8048-8053.

Z. Chen, D. Higgins, H. Tao, **R.S. Hsu**, Dr. Z. Chen 2009. "Highly Active Nitrogen-Doped Carbon Nanotubes for Oxygen Reduction Reaction in Fuel Cell Applications", Journal of Physical Chemistry C, Vol. 113, No. 49, 21008-21013.

- Non-refereed Publications

R.S. Hsu, Dr. Z. Chen 2009. "Platinum/Tin Oxide – Single Walled Carbon Nanotube Electrocatalysts for Direct Ethanol Fuel Cells", ECS Transactions, Vol. 25, No. 1, 1169-1176.

Dr. Z. Chen, **R.S. Hsu** 2009. "Nafion/Acid Functionalized Mesoporous Silica Nanocomposite Membrane for High Temperature PEMFCs", ECS Transactions, Vol. 25, No. 1, 1151-1157.

R.S. Hsu, Dr. Z. Chen 2010. "Improved Synthesis Method of a Cyanamide Derived Non-Precious ORR Catalyst for PEFCs", ECS Transactions, Vol. 28, No. 23, 39-46.

J.Y. Choi, **R.S. Hsu**, Dr. Z. Chen 2010. "Nanoporous Carbon-Supported Fe/Co-N Electrocatalyst for Oxygen Reduction Reaction in PEM Fuel Cells", ECS Transactions, Vol. 28, No. 23, 101-112.

- Selected Presentations

High Performance Nonprecious Metal Catalysts for Oxygen Reduction Reaction in PEM Fuel Cells. ECS 217th ECS Meeting. Oral Presentation. Vancouver, Canada, April, 2010.

Functionalized Titanium Dioxide Nanotube Based Composite Membranes for High Temperature PEMFCs. ECS 217th ECS Meeting. Oral Presentation. Vancouver, Canada, April, 2010.

Platinum Tin Oxide – Single Walled Carbon Nanotube Electrocatalyst for Direct Ethanol Fuel Cell. *Particle Technology Research Centre Conference*, London Ontario, Canada, July 2009.

Highly Active Carbon Nitride Electrocatalysts for the Oxygen Reduction Reaction for PEM Fuel Cell Applications. Ontario Fuel Cell Research & Innovation Network. Oral Presentation. Waterloo, Canada, December 2009.

Platinum/Tin Oxide – Single Walled Carbon Nanotube Electrocatalyst for Direct Ethanol Fuel Cell. 216th ECS Meeting. Oral Presentation. Vienna, Austria, August 2009.

Nafion/Acid Functionalized Mesoporous Silica Nanocomposite Membrane for High Temperature PEMFCs. 216th ECS Meeting. Oral Presentation. Vienna, Austria, August 2009.

H2U Waterloo Student Design Team. NHA Annual Hydrogen Conference and Expo 2008. Poster presentation. Sacramento, California, United States of America, April 2008.